A Comparison of the Response of 316 SS and the P7 Alloy to Heavy-Ion Irradiation

Robert Lee Sindelar

June 1985

UWFDM-637

Ph.D. thesis.

A Comparison of the Response of 316 SS and the P7 Alloy to Heavy-Ion Irradiation

Robert Lee Sindelar

Fusion Technology Institute
University of Wisconsin
1500 Engineering Drive
Madison, WI 53706

http://fti.neep.wisc.edu

June 1985

UWFDM-637

Ph.D. thesis.

A COMPARISON OF THE RESPONSE OF 316 SS AND THE P7 ALLOY TO HEAVY-ION IRRADIATION

BY

ROBERT LEE SINDELAR

A thesis submitted in partial fulfillment of the
requirements for the degree of

DOCTOR OF PHILOSOPHY

(Nuclear Engineering)

at the

UNIVERSITY OF WISCONSIN-MADISON

1985

A COMPARISON OF THE RESPONSE OF 316 SS AND THE P7 ALLOY TO HEAVY-ION IRRADIATION

Robert Lee Sindelar

Under the Supervision of Professor Gerald L. Kulcinski

The subject of this thesis is a comparison of a high purity austenitic stainless steel to a commercial purity type 316 stainless steel after exposure to heavy-ion irradiations.

Specimens of the P7 alloy, a high purity austenitic alloy similar to 316 SS but with a high (1000 appm) oxygen content, and the MFE heat of 316 SS were irradiated with 14 MeV nickel ions at temperatures which ranged from 400 to 650°C (0.4-0.55 T_m). These studies were conducted at displacement damage rates from 1 to 4 x 10^{-3} dpa/s within a layer ~ 3 μm from the specimen surface. A cross-sectioning technique of specimen preparation was applied to allow TEM analysis throughout this damage range. This study is the first report on heavy-ion irradiation effects on P7 and 316 SS viewed in cross-section.

Voids readily formed in P7 over all temperatures and doses investigated (400-650°C, 2-100 dpa). A suppression in the cavity number density and size was noted at depths which correspond to the range of the bombarding nickel ions for irradiations at temperatures of 400 and 500°C. This decrease in cavity nucleation agrees with current radiation damage models for these irradiation conditions.

Void formation in 316 SS occurred from the lowest temperature investigated, 450°C, up to 550°C. The absence of void formation in samples irradiated at 600 and 650°C up to 40 dpa is attributed to the inability to nucleate voids at these temperatures in the absence of gaseous nucleating agents.

Extensive phase decomposition occurred in 316 SS under irradiation over the entire irradiation temperature range. Small, 5-30 nm nickel rich precipitates formed at 450-550°C during irradiation. Cavities were seen to form only at the precipitate-matrix interface. At 600 and 650°C, the Fe_2P phase, a radiation-induced phase was the predominant microstructural feature.

A swelling rate study of the P7 alloy at 650°C yielded a swelling rate of 0.4%/dpa. These results are consistent with other heavy-ion swelling rates but are lower by a factor of 2 than the rate which occurs during fast neutron irradiation. Modeling of the swelling with respect to the depth-dependent damage has shown corrections can be applied to the dose levels to yield steady-state swelling rates approaching 0.7%/dpa.

APPROVED:

June 12, 1985

Date

Professor Gerald L. Kulcinski
Nuclear Engineering Department

ACKNOWLEDGEMENTS

The road to the completion of a research thesis is not traveled alone. Without the guidance and support of many advisors and friends, this work would not have been possible.

My thesis advisor, Professor G.L. Kulcinski, has given direction to the overall project as well as many useful suggestions on subtle details which make an effective presentation. Professor R. Arthur Dodd has developed useful experimental techniques and provided insights for this study. Discussions with Professor W.G. Wolfer were also very helpful.

I would also like to thank Professor P.A. Quin and the rest of the University of Wisconsin Nuclear Physics group for the use of the tandem accelerator irradiation facility. Technical support for the heavy-ion irradiations was ably provided by J.H. Billen and R.C. Schmidt. Also, I extend a special thanks to R.J. Casper for his assistance with the operation of the electron microscopes.

Several past members of the Radiation Damage Group, S.K. McLaurin, R.W. Knoll, R.H. Zee, H. Attaya and D.B. Bullen have given valuable suggestions and assistance. I am also grateful for the discussions with and help from the current members, S.J. Zinkle, D.L. Plumton, L.E. Seitzman, J. Kai, D.J. Pertzborn, C.D. Croessmann, D.H. Plantz, L. Wang and J. Liang.

I wish to extend special acknowledgements to Ms. E.A. Brown for her expedience and skill in processing this organized manuscript and D. Bruggink for his aid with the preparation of the graphics.

Finally, I would like to express my love and thanks in return for the love and support I have received from my family throughout the course of my collegiate career. I dedicate this thesis to the memory of my father, Raymond R. Sindelar.

Funding for this project was provided by the U.S. Department of Energy, Office of Fusion Energy.

TABLE OF CONTENTS

PAGE

ABSTRACT.. ii

ACKNOWLEDGEMENT... iv

LIST OF FIGURES... ix

LIST OF TABLES.. xii

1. INTRODUCTION... 1

    References for Chapter 1................................ 4

2. ASPECTS OF RADIATION EFFECTS IN METALS................... 6

    A. Microstructural Evolution Under Heavy-Ion Irradiation 6

        1. Calculation of dpa Under Heavy-Ion Irradiation.... 7

        2. Void and Loop Nucleation......................... 13

        3. Void Growth Kinetics............................. 23

    B. Phase Evolution Under Irradiation.................... 27

        1. Precipitate Classification....................... 30

        2. Enhanced and Induced Solute Segregation.......... 31

        3. Precipitate Growth and Dissolution Under Irradiation.................................. 34

    References for Chapter 2................................ 37

3. REVIEW OF THERMAL STUDIES AND ION IRRADIATIONS OF 316 SS.. 44

    A. Thermal Studies of 300-Series Austenitic Steels...... 44

        1. Phases Formed During Thermal Aging............... 44

        2. Time-Temperature-Precipitation in 316 SS......... 52

        3. Phase Evolution.................................. 52

PAGE

B. Ion-Irradiation Studies of 316 SS.................... 54

C. Ion-Irradiation Studies of P7........................ 59

References for Chapter 3................................ 67

4. EXPERIMENTAL APPARATUS AND PROCEDURE..................... 70

A. Specimen Composition and Characterization............ 70

B. Heavy-Ion Irradiation Facility....................... 74

C. Specimen Preparation and Analysis.................... 80

1. Pre-Irradiation Specimen Preparation............. 82

2. Post-Irradiation Specimen Preparation............ 82

3. Jet-Electropolish of Cross-Sectioned Specimens.... 84

4. Extraction Replica Procedure..................... 85

5. 316 SS Standard.................................. 86

6. Iron Plating of Ferritic Alloys.................. 87

7. Error Analysis................................... 88

References for Chapter 4................................ 89

5. RESULTS.. 90

A. Nickel-Ion-Irradiated P7 Alloy....................... 93

1. Injected Interstitial Effects..................... 93

2. 650°C Irradiations of P7......................... 102

B. Nickel-Ion-Irradiated 316 SS......................... 113

1. 450-550°C Irradiations of 316 SS................. 116

2. 600-650°C Irradiations of 316 SS................. 122

PAGE

3. Precipitation in Ion-Irradiated 316 SS............ 129

References for Chapter 5................................ 135

6. DISCUSSION.. 137

A. Effect of Impurities on Void Swelling................. 137

1. Effect of Oxygen on Void Swelling................. 139

2. Heterogeneous Void Formation...................... 141

3. Temperature Dependence of Void Formation.......... 143

B. Effects of the Injected Interstitials................. 149

C. Swelling Rates of Austenitic Stainless Steels......... 155

1. Heavy-Ion Swelling Rates of P7 and 316 SS......... 155

2. Fast Neutron and Electron Swelling Rates of Austenitic Stainless Steels.................... 162

3. Factors Which Determine the Swelling Rate of Austenitic Stainless Steels.................... 163

4. Effects of Cavitation on Damage Calculations in Ion-Irradiated P7............................. 167

References for Chapter 6................................ 176

7. CONCLUSIONS.. 181

8. SUGGESTIONS FOR FUTURE WORK................................. 184

LIST OF FIGURES

PAGE

Fig. 2.1. Displacement damage vs. depth for 14 MeV Ni on 316 SS, P7 14

Fig. 2.2. Precipitation effects on swelling 28

Fig. 3.1. EDS spectra of ppt. in thermally-aged 316 SS 48

Fig. 3.2. TTP diagram for 316 SS 53

Fig. 3.3. Phase reaction sequence of 316 SS 55

Fig. 4.1. Thermal-mechanical handling of 316 SS 72

Fig. 4.2. Grain size of 316 SS 73

Fig. 4.3. Dislocation structure in unirradiated 316 SS 73

Fig. 4.4. Auger spectrum from surface of P7 foil 75

Fig. 4.5. Auger spectrum from 0.5 μm depth of P7 foil 75

Fig. 4.6. University of Wisconsin Heavy-Ion Irradiation Facility 76

Fig. 4.7. Heavy-Ion target stand 78

Fig. 4.8. Cross section schematic 81

Fig. 4.9. Irradiated foil schematic 83

Fig. 4.10. Plating holder and bubbler apparatus 83

Fig. 5.1. Irradiation parameters for P7, 316 SS 92

Fig. 5.2. Stacking fault tetrahedra observed near the end of the damage range in the P7 alloy 94

Fig. 5.3. Voids in P7 - 400°C 95

Fig. 5.4. Void parameters, P7 - 400°C 96

Fig. 5.5. Voids in P7 - 500°C 98

PAGE

Fig. 5.6. Void parameters, P7 - 500°C........................ 100

Fig. 5.7. Void parameters, P7 - 550°C........................ 101

Fig. 5.8. Temperature dependence of swelling of P7........... 103

Fig. 5.9. Voids in P7 - 650°C................................ 104

Fig. 5.10. Void parameters, P7 - 650°C....................... 105

Fig. 5.11. Voids in P7 - 650°C............................... 107

Fig. 5.12. Void parameters, P7 - 650°C....................... 108

Fig. 5.13. Void-dislocation structure, P7- 650°C............. 109

Fig. 5.14. Void parameters, P7 - 650°C....................... 110

Fig. 5.15. Outgassed P7 - 650°C.............................. 112

Fig. 5.16. Dislocation structure, 40 dpa - 316 SS............ 114

Fig. 5.17. Void-ppt. association in 316 SS................... 117

Fig. 5.18. Void parameters, 316 SS - 450°C................... 118

Fig. 5.19. Voids in 316 SS - 500°C........................... 119

Fig. 5.20. Void parameters, 316 SS - 500°C................... 120

Fig. 5.21. Void parameters, 316 SS - 500°C................... 121

Fig. 5.22. Void parameters, 316 SS - 550°C................... 123

Fig. 5.23. Through-focus void-ppt............................ 124

Fig. 5.24. Through-range, 316 SS - 600°C..................... 125

Fig. 5.25. Through-range, 316 SS - 650°C..................... 127

Fig. 5.26. Optical-TEM, 316 SS - 650°C....................... 128

Fig. 5.27. G-phase 316 SS.................................... 130

Fig. 5.28. Fe_2P-phase 316 SS.............................. 132

PAGE

Fig. 5.29. $M_{23}C_6$-phase 316 SS.............................. 133

Fig. 5.30. MnS-phase 316 SS................................ 134

Fig. 6.1. Void-ppt., 316 SS................................ 142

Fig. 6.2. Void-ppt.-matrix schematic........................ 145

Fig. 6.3. Swelling curve, 316 SS - 40 dpa................... 147

Fig. 6.4a. Void growth rate with injected interstitials...... 151

Fig. 6.4b. Void growth rate with injected interstitials...... 151

Fig. 6.5. Steady state nucleation rate with injected interstitials.. 154

Fig. 6.6. Void swelling, P7 - 650°C......................... 157

Fig. 6.7. Dpa vs. depth, void-free P7....................... 158

Fig. 6.8. Swelling rate, P7 first-order corrected........... 159

Fig. 6.9. Swelling rate, P7 and 316 SS...................... 160

Fig. 6.10. Swelling rate, neutron irradiated alloy.......... 160

Fig. 6.11. F/P as a function of E_v^m and sink strength......... 165

Fig. 6.12. Net bias for voids............................... 165

Fig. 6.13. Swelling profile - P7............................ 169

Fig. 6.14. Dpa rate, P7 with voids.......................... 173

Fig. 6.15. Swelling rate, P7 second-order corrected......... 175

LIST OF TABLES

PAGE

Table 1.1. International equivalent classifications of austenitic stainless steels........................ 2

Table 3.1. Phases observed in austenitic stainless steels.... 45

Table 3.2. Composition of phases formed in aged 316 SS....... 46

Table 3.3. Composition of phases formed in aged 316 SS....... 46

Table 3.4. Phase orientation relationships to fcc matrix..... 50

Table 3.5. Previous ion-irradiation studies of 316 SS........ 56

Table 3.6. Previous ion-irradiation studies of P7........... 60

Table 4.1. Chemical analysis of MFE heat of 316 SS.......... 71

Table 4.2. Chemical analysis of MFE heat of 316 SS.......... 71

Table 4.3. Chemical analysis of the P7 alloy................ 71

Table 4.4. Oxygen and nitrogen content of 316 SS, P7......... 74

Table 4.5. EDS ratio constants (k values).................... 87

Table 5.1. 14 MeV nickel ion irradiation parameters.......... 91

Table 5.2. Dislocation structure - P7........................ 92

Table 5.3. Dislocation structure - 316 SS.................... 115

Table 5.4. Precipitation parameters - 316 SS................. 131

Table 6.1. Composition of 316 SS, Firth Vickers 555 316 SS, En588 321 SS, P7 alloy............................ 148

Table 6.2. Parameters for 650°C P7 irradiations............. 156

CHAPTER 1. INTRODUCTION

The structural materials of controlled thermonuclear reactors (CTR) will be exposed to intense radiation in the form of high energy neutrons and charged particles at high temperatures. Unfortunately, this environment causes displacement damage in these materials(1) which can lead to the rapid degradation of the mechanical properties and the onset of void-induced swelling.(2)

Austenitic stainless steels[a] are a leading candidate for first wall structural materials. However, extensive void swelling would limit first wall lifetimes of magnetic fusion reactors (MFR)(5,6) and there is a large economic incentive to understand the causes for such behavior.

Simple compositional modification by means of impurity atom additions (e.g., Si, C) or changes in the Fe-Cr-Ni ratio has been shown to yield significant reductions in the swelling response of these alloys.(7) This reduced swelling is temporary, as austenitic alloys show large increments of swelling per unit of damage after an initial transient period of 20-100 dpa.(8) It has been re-

---

[a] Austenitic stainless steels are highly corrosion resistant, nonmagnetic steels which are produced by many industrialized nations. Table 1.1 lists the composition limits of the American Iron and Steel Institute classification of the 300 series (austenitic) stainless steels. Because of their well-developed fabrication process, an extensive data base on their mechanical properties and their overall service characteristics, these steels are being used as a fast fission reactor cladding material and have been proposed as structural materials in fusion reactors.

Table 1.1 (3)

SPECIFIED ANALYSIS (WT PERCENT) OF THE AISI 300 SERIES AUSTENITIC STAINLESS STEELS

	C max.	*Si* max.	*Mn* max.	*Cr*	*Ni*	*Mo*	*Ti*	*Nb*
Steels								
301	0·15	1·00	2·00	16–18	6–8			
302	0·15	1·00	2·00	17–19	8–10			
304	0·08	1·00	2·00	18–20	8–12			
310	0·25	1·50	2·00	24–26	19–22			
316	0·08	1·00	2·00	16–18	10–14	2·00–3·00		
321	0·08	1·00	2·00	17–19	9–12		5 × % C min.	
347	0·08	1·00	2·00	17–19	9–13			10 × % C min.
316 (Dev. spec.)[a]	0·03–0·08	0·2–0·6	1·6–2·00	16·5–18	11–12·5	2–2·75	0·02 max.	0·02 max.
Weld metals								
316 (19–12–3)	0·08	1·0	0·5–2·5	17–20	10–14·0	2·5–3·5		
316 (17–8–2)	0·06–1·0	0·8	0·5–2·5	16·5–18·5	8–9·5	1·5–2·5		
308	0·08	1·00	2·0	18–20	10	—	—	

[a] Additional components: Zr, 0·02 max.; V, W, 0·1 max.; Co, 0·15 max.; Cu, 0·25 max.; As, Sn, 0·03 max.; Al, 0·05 max.; B, 0·0020–0·005; N, 0·040–0·07. (From Wood [4].)

ported(9,10) that the post-transient swelling rate of austenitic alloys is typically 1%/dpa. This swelling rate would severely limit the use of this alloy as a structural material for a commercial fusion reactor which requires a first wall lifetime of 120-200 MW-y/m^2 (i.e., 40 yr x 3-5 MW/m^2).[b]

Metallurgically-tailored austenitic stainless steels can, however, suppress the deleterious swelling levels by extending the low swelling transient regime.(12) Specifically, the Primary Candidate Alloy (PCA), a Ti-modified austenitic stainless steel, has shown significantly less void swelling compared to 316 SS after irradiation under similar conditions.(13,14) Thus, austenitic steels are still contenders for CTR structural materials, especially in the 100 dpa or lower regime.

As mentioned above, impurity atoms have a large influence on the duration of the transient regime. It is important to characterize the role of each impurity species to preclude the inadvertent fabrication of a high swelling structural material.

A convenient way to examine the effects of displacement damage on microstructural evolution with controlled irradiation parameters is through the use of ion irradiation studies.(2) The objective of this study is to characterize the response of a high-purity, high-

---

[b] The power level of a fusion reactor is specified in terms of the neutron wall loading -- the energy carried through the first wall by the 14 MeV neutrons, which are just one product of the D-T fusion reaction. Current annual wall loading estimates range from 3 to 5 MW/m^2. A loading of 1 MW/m^2 is equivalent to 11.5 <u>d</u>isplacements <u>p</u>er <u>a</u>tom in a cylindrical plasma chamber.(11)

swelling, austenitic stainless steel, designated as the P7 alloy, and of a commercial purity 316 stainless steel to high levels of radiation damage produced by ion irradiation. Irradiations are performed at temperatures from 400-650°C (0.4-0.55 T_m), up to dose levels of 120 dpa, and at rates of 1-6 x 10^{-3} dpa/s using 14 MeV nickel ions. Careful attention is paid to the initial gas content of the alloys. Specifically, care was taken to exclude the inadvertent introduction of the reactive gas species oxygen prior to irradiation.(15)

The irradiated samples are analyzed in cross-section.(16) This technique of TEM sample preparation provides depth-dependent damage information in heavy-ion irradiated material and allows for the study of cavity nucleation and growth by the bombarding nickel ion species.(17) It also facilitates a study of dose and dose rate variations in an ion-irradiated sample.

Previous heavy-ion irradiation results have yielded a swelling rate much lower than the typical 1%/dpa rate characteristic of fast neutron irradiations.(18) To gain insight into this discrepancy a swelling rate study is performed at 650°C in the P7 alloy.

References for Chapter 1

1. G.L. Kulcinski, "Radiation Damage: The Second Most Serious Obstacle to Commercialization of Fusion Power," in Proceeding of International Conference on Radiation and Tritium Technology for Fusion Reactors, Gatlinburg, TN, 1-3 Oct. 1975.

2. Radiation-Induced Voids in Metals, J.W. Corbett and L.C. Ianniello (Eds.), Proceeding of the 1971 International Conference, Albany (1971).

3. American Iron and Steel Institute, steel products manual. Stainless and heat resisting steels, New York, AISI, (1974).
4. D.S. Wood, Intern. Conf. Mech. Behavior and Nucl. Appl. of Stainless Steels at Elevated Temps., Varese, Met. Soc. (1982).
5. E.E. Bloom et al., Nucl. Tech. 31 (1976) 115-22.
6. R.F. Mattas et al., J. Nucl. Mater. 122 & 123 (1984) 230-35.
7. Radiation Effects in Breeder Reactor Structural Materials, M.L. Bleiberg and J.W. Bennet (Eds.), TMS-AIME (1977).
8. F.A. Garner, J. Nucl. Mater. 122 & 123 (1984) 459-471.
9. W.G. Wolfer, ibid, pp. 367-378.
10. F.A. Garner and W.G. Wolfer, ibid, pp. 201-206.
11. F.W. Wiffen et al., in The Metal Science of Stainless Steels, E.W. Collings and H.W. King (Eds.), TMS-AIME (1978) 146-159.
12. P.J. Maziasz, in Ref. 9, pp. 472-486.
13. P.J. Maziasz, in Ref. 9, pp. 236-241.
14. P.J. Maziasz and D.N. Braski, in Ref. 9, pp. 311-316.
15. R.L. Sindelar, R.A. Dodd and G.L. Kulcinski, in DAFS Quarterly Progress Report DOE/ER-0046/21, April 15, 1985.
16. S.J. Zinkle and R.L. Sindelar, DAFS Quarterly Progress Report DOE/ER-0046/20, February 15, 1985.
17. B. Badger, Jr., et al., ASTM-STP 870, J.S. Perrin and F.A. Garner (Eds.), (1984).
18. F.A. Garner, J. Nucl. Mater. 117 (1983) 177.

CHAPTER 2. ASPECTS OF RADIATION EFFECTS IN METALS

A. Microstructural Evolution Under Heavy-Ion Irradiation

Interactions of radiation with a metal target can alter the microstructure of the metal through collisions which cause displacements of atoms from their original lattice sites in the metal. Neutrons, high energy protons, high energy electrons, ions, and even energetic photons, through initial interactions with target electrons, are all capable of creating Frenkel defects, i.e. vacancy-interstitial pairs. Each of the above forms of radiation has its own cross section for an energy transfer between projectile and target atom, $d\sigma(E)/dT$, which is dependent on the energy of the incident radiation (E) and also on the energy transferred (T) to the target atom. If the target atom acquires a threshold amount of energy, E_d, it can be displaced from its lattice site, and it becomes a PKA (Primary Knock-on Atom). This PKA, depending on its energy, can itself generate many more displaced atoms.

The cumulative effect of an irradiation which causes displacements is measured in a unit of dose called a displacement per atom. A given volume of crystalline material that has suffered an irradiation to a dose of 1 dpa means that, on the average, each lattice atom had been displaced once during the irradiation.

A microscopic examination of the spatial production of displaced atoms would reveal inhomogeneities. A PKA of high energy is likely to produce a large cascade in which some vacancies and interstitials are produced so close to one another that spontaneous recombination or spontaneous defect clustering can occur with very little point defect escape. This effect, as well as displacement rate, temperature of the target material, impurity atom effects, etc. are all parameters that can affect the evolution of a target's microstructure during irradiation.

A.1. Calculation of dpa Under Heavy-Ion Irradiation

In the early 1960's Lindhard, Scharff, Schiott (hereafter referred to as LSS), and others(1-7) developed a statistical method of accounting for and describing the spatial distribution of heavy ions impinging on a target. Modern computer codes used today utilize LSS theory to calculate the depth distribution of energy deposition of a material under ion bombardment.(8,9)

In LSS theory,(5) the ion beam is considered to lose energy by two independent types of collisions. Inelastic collisions with the electrons of the target atoms cause electronic excitation which is subsequently dissipated as heat. Elastic collisions with the target atoms may produce the PKA's which may themselves create further displacement damage by forming higher order knock-on atoms.

First, the treatment by LSS of nuclear collisions will be described (i.e., the elastic collisions). The interaction potential between the projectile and target atoms is a screened Coulomb potential,

$$V(r) = \frac{Z_1 Z_2 e^2}{r} \phi \left(\frac{r}{a}\right) \tag{2.1}$$

where ϕ is the screening function of the Thomas-Fermi model of the atom, and where

$$a = 0.8853\ a_o(Z_1^{2/3} + Z_2^{2/3})^{-1/2} \qquad (2.2)$$

with $\qquad a_o = \text{Bohr radius} = \hbar^2/me^4$

is the screening radius as given by Lindhard. The rationale for using a <u>screened</u> Coulomb potential is that the straight Coulomb potential gives too much low angle scattering and at low energy, electron shielding of the nucleus must be considered.

Lindhard uses a dimensionless recoil energy, t, and a dimensionless impact parameter to arrive at the differential scattering cross section for the nuclear collisions given by:

$$d\sigma_{\text{nuclear}} = \pi a^2\ dt/(2t^{3/2})\cdot f(t^{1/2})\ . \qquad (2.3)$$

The function $f(t^{1/2})$ is a function that depends on the assumed form of the screening function. For the Thomas-Fermi screening function, Lindhard numerically evaluated $f(t^{1/2})$.(5) Winterbon et al.(7) obtained the analytical approximation for $f(t^{1/2})$:

$$f(t^{1/2}) = 1.309\ t^{1/6}(1 + (2.618\ t^{2/3})^{2/3})^{-3/2}\ . \qquad (2.4)$$

The projectile energy deposited into nuclear collisions per unit path length is simply:

$$\left(\frac{dE}{dR}\right)_n = N \int_0^{T_m} T \, d\sigma_{\text{nuclear}} \, , \tag{2.5}$$

where N = target atomic density

T = energy transferred to target atom.

Using a dimensionless ion range,

$$\rho = RNM_2 \frac{4\pi a^2 M_1}{(M_1 + M_2)^2} \tag{2.6}$$

and with the dimensionless recoil energy in Eq. (2.3), the dimensionless nuclear stopping power is obtained:

$$\left(\frac{d\varepsilon}{d\rho}\right)_n = \int_0^{\varepsilon} dx \; f(x)/\varepsilon \tag{2.7}$$

where $x = t^{1/2}$ and a range of validity $\varepsilon > 0.01$.

To obtain the electronic stopping power, Lindhard(3) developed a stopping power valid for bombarding ions with energy:

$$E \lesssim 24.8 \, A_1 Z_1^{4/3} \text{ (in keV)} \, . \tag{2.8}$$

In dimensionless range and transfer energy variables the stopping power is written:

$$\left(\frac{d\varepsilon}{d\rho}\right)_e = k\varepsilon^{1/2} \tag{2.9}$$

where $$k = Z_1^{1/6} \frac{0.0793\, Z_1^{1/2} Z_2^{1/2} (M_1 + M_2)^{3/2}}{A_2^{1/2} M_1^{3/2} (Z_1^{2/3} + Z_2^{2/3})^{3/4}} \; . \tag{2.10}$$

This electronic stopping power has deficiencies however shown by discrepancies with experimental data. It fails to show the experimental oscillations with Z_1 for the stopping power. Also Narayan,(10-12) Whitley,(13) Bullen,(14) and Zinkle(15) have shown results which suggest that Eq. (2.9) may overestimate the electronic energy loss.

Brice has developed a semi-empirical three parameter formula for the electronic stopping power.(16) However, even this modeling is insufficient to match the experimental data with the calculated damage range.(12-15)

When the nuclear and electronic stopping powers have been determined it is possible to calculate the range of the bombarding ions into the target material as a function of the energy. With this calculation, the nuclear energy loss per unit projected path length can be ascertained as a function of the projected path length x, $S_D(x)$:(8)

$$S_d(x) = \int_x^{\infty} f(x')\, S_L[E_1(x' - x)]\, \frac{dR(x' - x)}{dx'}\, dx' \tag{2.11}$$

where $E_1(y)$ = the average energy of the ions whose projected range is y,

$f(y)$ = the fraction of beam ions with projected range in the neighborhood dy of y, assumed to be a Gaussian distribution(17)

$$f(y) = \frac{1}{\sqrt{2\pi}} \alpha_y \exp\left(- \frac{(y - y_m)^2}{(2\alpha_y^2)}\right) \tag{2.12}$$

with α_y = RMS standard deviation in the projected range. This is a measure of the intrinsic straggling (Bragg straggling) due to statistical fluctuations in the number of collisions the particles undergo.

Also, $R(y)$ = total range (measured along the path of a beam ion), considered as a function of projected range y, and dR(y)/dy relates the total range to the projected range with

$$S_L(E) = N \int_{T_d}^{T_m} Tn(T)\, d\sigma(T) \tag{2.13}$$

where $S_L(E)dR$ = total amount of energy going only into *elastic*, displacement causing collisions for a projectile and the subsequent projectiles it creates for an initial projectile energy E, and

$n(T)$ = fraction of PKA energy dissipated into displacements. It is given by:

$$n(T) = [1 + kg(\varepsilon)]^{-1} \qquad (2.14)$$

where Robinson(18) has numerically fit the function $g(\varepsilon)$ to:

$$g(\varepsilon) = \varepsilon + 0.40244\ \varepsilon^{3/4} + 3.4008\ \varepsilon^{1/6}\ . \qquad (2.15)$$

Using a modified Kinchen and Pease model of Torrens and Robinson,(19) the displacements per unit time at a depth x is:

$$K(x) = \phi\,\frac{KS_D(x)}{N\cdot 2E_d} \qquad (2.16)$$

where ϕ is the incident ion flux, K is the displacement efficiency which accounts for events that do not lead to displacements. Torrens and Robinson(19) arrived at K = 0.8 from computer modeling of the cascade structure. However, Kinney(20) has recently compiled data which shows that K = 0.3 is probably a more appropriate measure of the residual displacement damage for neutrons or ions if the PKA energy is $\gtrsim$ 30 keV. Nevertheless, the damage values in this paper will be derived from a K = 0.8 value to be consistent with the previous decade of ion bombardment studies. The average energy which must be imparted to a lattice atom to displace it, E_d, is highly dependent on crystallographic direction. Thus, the minimum value, $E_{d,min}$, obtained for 316 SS by Makin(21) (19 eV) is multiplied by 5/3 to account for directional dependence. In this study, a standard value of

E_d = 40 eV(22) for ferrous alloys is chosen to facilitate comparison of dose effects with other iron-based alloy systems.

Figure 2.1 shows the final result of the damage level as a function of depth for a flux of 14 MeV Ni ions on 316 SS calculated using the Brice Code(23) with the LSS electronic stopping power.

A.1.1. Spatial Distribution of the Damage

The distribution of displacements produced in the irradiation was mentioned before to reveal inhomogeneities. Depending on the energy of the PKA's, a collection of defects can be produced characterized by a vacancy-rich depleted zone surrounded by Frenkel interstitials.

Computer modeling has been used to understand this phenomenon.(24) A single cascade process requires ~ 10^{-13} seconds after which a ~ 10^{-11} second annealing period takes place due to the instability of the configuration.(25,26) In addition to annihilations of vacancies with interstitials, clustering of like defects or entrapment at some microstructural feature is possible.

A.2. Void and Loop Nucleation

The production of point defects gives rise to vacancy and interstitial concentrations which are in excess of thermal equilibrium values and this makes defect cluster formation possible. Collapsed vacancy-rich regions as well as agglomeration of point defects may form faulted/unfaulted loops, stacking fault tetrahedra, or even cavities (includes voids and inert-gas-containing three-dimensional vacancy clusters). The process of vacancy or interstitial agglomer-

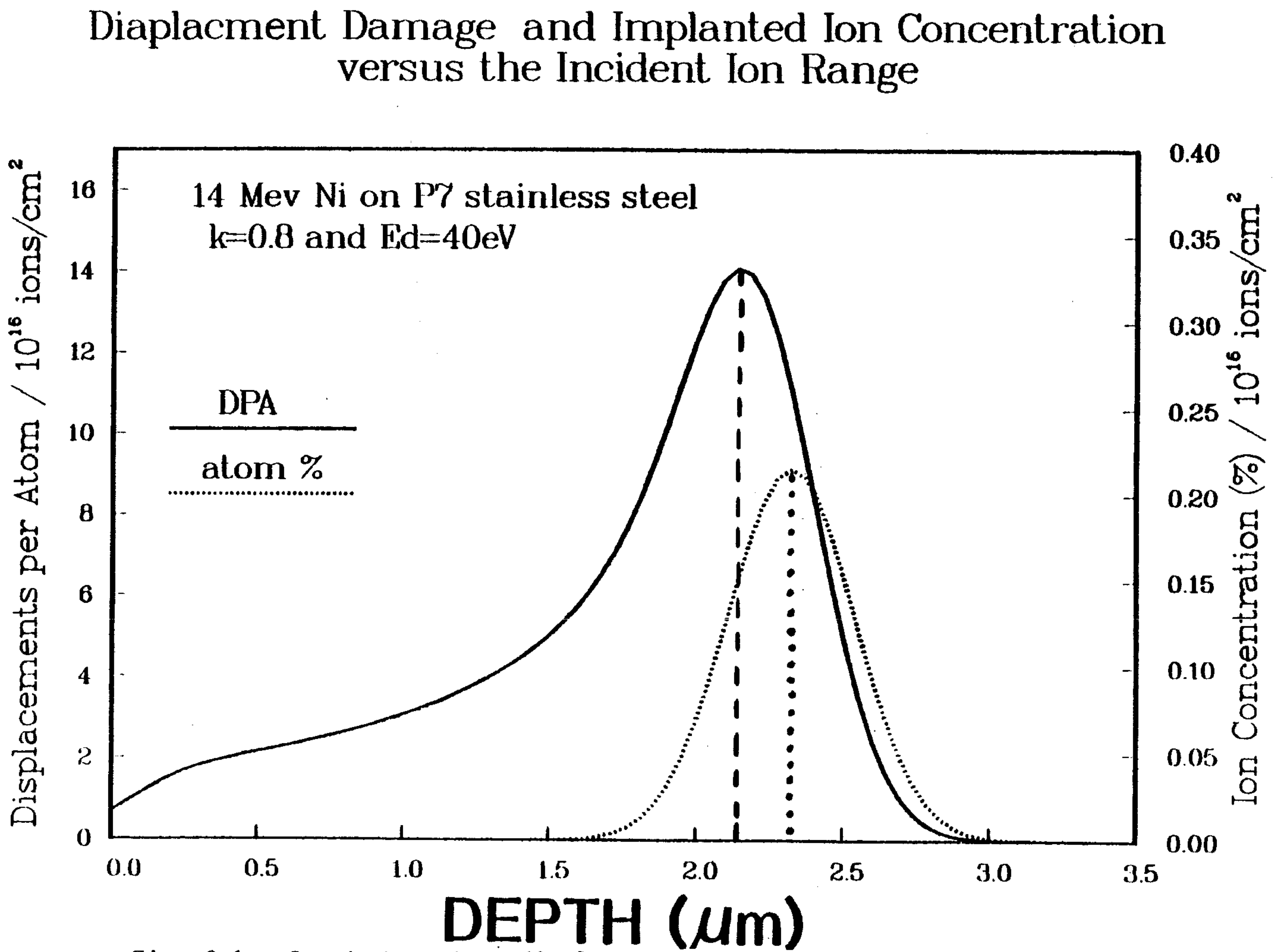

Fig. 2.1. Depth-dependent displacement damage in 316 stainless steel calculated using the Brice code$^{(23)}$ and Eq. (2.16) with $K = 0.8$ and $E_d = 40$ eV.

ation requires the mobility of these defects in the crystalline material.

Interstitials, having a relatively low (few hundredths to few tenths eV) migration energies, are mobile and readily form defect clusters at all temperatures of irradiation. Vacancy mobility in the lattice however requires a material temperature $\gtrsim 0.3\ T_{m.p.}$ because vacancy migration energies are on the order of eV. Therefore the vacancy flux produced during the irradiation would be nearly equal to the interstitial flux. This condition would then preclude the growth of any vacancy clusters possibly existing from the displacement cascade. However, interstitials are preferentially absorbed (compared to vacancies) at dislocations due to the very large elastic strains associated with self-interstitial atoms.(27,28) This occurrence allows a net vacancy flow to vacancy clusters when a suitable dislocation density has developed.

The evolutionary track of vacancy agglomeration is separated into two regimes -- nucleation and growth. A void embryo in the nucleation regime becomes a void nucleus upon attainment of a critical size. Below this size the cluster is unstable and will tend to dissolve and above this value the cluster will grow with further irradiation.

Void nucleation may be homogeneous, if there are no sites where the free energy of a cluster is lower than any other site. The nucleation may be termed heterogeneous, when nuclei form at places such as dislocations, precipitates, etc., at which the free energy for cluster formation is lower than a matrix site.

The various homogeneous/heterogeneous mechanisms of nucleation are detailed in a review by Russell.(29) His treatment of helium as an ideal gas should be modified however, due to the large pressures involved in cavity embryos.(30)

The theory of homogeneous nucleation of voids was first developed in 1971 independently by Katz and Wiedersich(31) and Russell.(32) With modifications to account for differences resulting from the possible co-precipitation of vacancies and interstitials, they adapted ideas of classical nucleation theory. Their void nucleation theory is a treatment describing the dynamics of small vacancy clusters (embryos). The clusters may shrink out of existence or they may grow to a stable size. Processes that cause cluster shrinkage are vacancy emission or interstitial absorption. The process that enables the clusters to grow is vacancy absorption. Using these ideas, the time rate change of clusters containing n vacancies can be expressed as a flux balance:

$$\begin{aligned} J_n = {} & [\beta_i(n + 1) + \alpha_v(n + 1)]\ \rho(n + 1) - [\beta_v(n + 1) \\ & + \beta_i(n) + \alpha_v(n)]\ \rho(n) + \beta_v(n - 1)\ \rho(n - 1) \end{aligned} \qquad (2.17)$$

where $\rho(n)$ and $\rho(n + 1)$ are the numbers of clusters containing n and (n + 1) vacancies, respectively, and where $\beta_v(n)$ is the rate of vacancy capture by a cluster of size n, $\beta_i(n)$ is the rate of interstitial capture by a cluster of size n and $\alpha_v(n)$ is the rate of vacancy emission by a cluster of size n.

Now using a condition of detailed balance, an expression can be obtained for $\alpha_v(n)$ in terms of $\beta_v(n)$ and $\rho(n)$.(32) Next, the deviation from classical nucleation is accounted for by taking into account the impingement of interstitials onto the void embryo for the activation energy of formation of the cluster. With this regard for co-precipitation of interstitials with vacancies, the steady state nucleation rate is written:

$$J_k = Z'\beta_k\rho'_k \qquad (2.18)$$

where ρ'_k is analogous to the equilibrium concentration of critical nuclei in classical nucleation theory.

$$\rho'_k = N_o \exp(-\frac{\Delta G'_k}{kT}) \qquad (2.19)$$

where N_O is the number of lattice sites/unit volume and $\Delta G'_k$ is the activation barrier for nucleation. It depends on the defect arrival ratio β_i/β_v and on the free energy of formation, ΔG^o_n, of a void of size n. The free energy term ΔG^o_n depends on the void size, the void-matrix surface energy, and on the vacancy supersaturation.

The factor Z' is the Zeldovich factor whose reciprocal is equal to the width at a distance kT below the maximum value of the activation barrier versus cluster size curve.

Also associated with this theory is the definition of an incubation time τ, which is the relaxation time for the approach to steady state after a step increase in supersaturation. This relaxation time is given by(29,33)

$$\tau = (2\ \beta_v^o n_k'^{1/3} Z'^2)^{-1} \qquad (2.20)$$

where n_k' is the number of vacancies in the critical nuclei, i.e. those which neither shrink nor grow at the prevailing supersaturation.

Extension of these concepts to dislocation loop nucleation with a concurrent supersaturation of interstitials and vacancies is straightforward.(34) The free energy term ΔG_n^o is modified to account for the strain energy of a loop as well as the stacking fault energy of a loop.

However, the above approach to void/loop nucleation is inadequate as the inert gas content and the effect of alloy composition including impurity levels in the metal must be considered.

Gases are thought to play a major role in the stability of three-dimensional vacancy clusters against collapse into planar loop aggregates. Gas may accomplish this by pressuring a cavity nucleus and/or reducing the surface energy of the cavity. Helium, a relatively insoluble inert gas, is continuously produced in-reactor as a result of (n,α) reactions and is therefore unavoidable. A review of the effects of helium on cavity formation is also given by Farrell.(35) Also, residual reactive gases such as hydrogen, nitrogen, and oxygen present in all commercial stainless steels by virtue of their processing, may facilitate cavity nucleation.(36,37) In fact, an early simulation study using heavy ions on 316 SS produced voids in the absence of any injected inert gas.(17)

The effects that solutes or impurities have on cavity nucleation and growth are complex. For immobile or slowly diffusing impurities, the trapping of vacancies at these species is suggested to reduce void nucleation via enhanced recombination.(38) Some observations indeed show lower void densities at a given fluence with the addition of these impurities(39) to stainless steels. Other studies(40) suggest even fast diffusing species may form fast diffusing solute-vacancy complexes and remove the vacancy supersaturation necessary for the driving force for void nucleation.

Solutes or impurities may also enhance void nucleation by the formation of "void coatings." These coatings are postulated(41,42) to reduce the interstitial capture efficiency of a void by means of a point defect-void image interaction. Impurities may also act to lower the void-matrix surface energy thereby promoting void nucleation.

Lastly, local composition changes through solute segregation to the void may alter the diffusion coefficients of point defects in the area around the void.(43) An enhancement of nickel and a reduction of chromium compared to matrix concentrations was in fact observed around voids that formed in fast-reactor-irradiated 316 SS.(44-46)

Precipitates are also important in the evolution of voids. Bullough et al., have recently incorporated the effects of precipitate-cavity entities into a computer code modeling the void evolution of 316 SS.(47) By a "capacitance" embedding procedure, they derived the sink strength for the precipitate-cavity entity. They found that the effect of such an entity is to reduce the incubation period for those cavities attached to precipitates.

Although previous ion-irradiation studies of 316 SS without helium do not show a marked association of voids with precipitates, ion-irradiation experiments of 316 SS with helium have shown precipitates form in a preferential association to cavities.(48-50) Voids are also commonly observed with precipitates in fast reactor-irradiated 316 SS.(51-54)

To incorporate the above complicated effects into a theory of nucleation and growth is not the object of this thesis. Nevertheless, models are continually being developed to account for these effects and these are briefly reviewed below.

Early attempts to more realistically model void nucleation included the effect of the gas atoms. Katz and Wiedersich(55) developed a nucleation model treating helium as an immobile gas. The activation energy for nucleation is then imagined as a surface which depends on the number of gas atoms and vacancies in the embryo. However, helium cannot realistically be treated as immobile. Russell(56) points out that the ultimate model used must take account of the mobility of the gas atoms.

To account for mobile gas atoms or impurity atoms, Russell(29) developed a general theory of void nucleation in metals via a nodal line/critical point formalism. Predictions made by this theory include possibilities of spontaneous void nucleation driven by inert gas as well as enhanced nucleation onto heterogeneous gas cluster or impurity cluster sites. Helium was incorrectly treated as an ideal gas and has been subsequently modeled more realistically.(57)

Most recently, Parker and Russell(58) have included in the nodal line formalism: (1) non-ideality of the inert gas; (2) linearly increasing helium concentration with dose; and (3) nucleation of cavities on approximately equilibrium bubbles of any size. In this treatment, the effects of solute segregation and precipitation were ignored.

Solute segregation effects were treated theoretically by Pillar and Marwick,(59) and more recently by Si-Ahmed and Wolfer.(41) Si-Ahmed and Wolfer consider the free energy terms of the point defects to determine the void bias factors for interstitials and vacancies.

These bias factors are used in the following equations for the capture rate of interstitials, of vacancies, and reemission rate of vacancies for voids:

$$\beta_i(x) = 4\pi r(x) D_i C_i Z_i^o(x) \qquad (2.21)$$

$$\beta_v(x) = 4\pi r(x) D_v C_v Z_v^o(x) \qquad (2.22)$$

$$\alpha_v(x) = 4\pi r(x) D_v C_v^o Z_v^o(x) \qquad (2.23)$$

where $Z_i^o(x)$ and $Z_v^o(x)$ are the interstitial and vacancy void bias factors, C_v and C_i are the concentrations of vacancies and interstitials and $r(x)$ is the void radius as a function of vacancy content x.

Another approach to nucleation was developed by Wolfer et al.(60) Their work resulted in a Fokker-Planck type equation describing the evolution of a void or loop size distribution over the nucleation and growth regimes. The equation found is:

$$\frac{\partial P(x,t)}{\partial t} = -\frac{\partial}{\partial x}\left[K(x)P(x,t)\right] + \frac{1}{2}\frac{\partial^2}{\partial x^2}\left[Q(x,t)P(x,t)\right] \qquad (2.24)$$

where $P(x,t)$ is the size distribution function with x denoting the number of vacancies in a cluster at time t, $K(x)$ is the drift force, and $Q(x,t)$ is a space-dependent diffusion coefficient. The critical embryo size occurs at x such that $P(x) = 0$.

Wehner and Wolfer(61) have recently applied a nonlinear transformation between x and the cluster radius r given by:

$$r = \left(\frac{3\Omega x}{4\pi}\right)^{1/3} + \frac{b}{2}\ . \qquad (2.25)$$

Here, Ω is the atomic volume, and the cluster or void surface is defined by the centers of the surface atoms. Their radii is assumed to be equal to half the Burger's vector b.

This transformation results in a new Fokker-Planck equation for the cluster distribution function $\tilde{P}(r,t)$. The solution of this equation relies on a technique based on the path integral.(62,63) This model(61) has proved very successful in treating the dynamic nucleation process and the subsequent growth stage in a unified formalism.

A.3. Void Growth Kinetics

The analytical framework for void growth utilizes concepts of chemical rate theory. Brailsford and Bullough(64) and Wiedersich(65) have extended the initial theory of Harkness and Li(66) to describe void growth with rate theory. The following outline of the ideas of rate theory are taken from an assessment of the theory by Mansur.(67)

To determine the swelling, the concentrations of vacancies and interstitials in the matrix must first be determined. These quantities are found as the solution to the following two coupled equations describing conservation of free vacancies and interstitials:

$$\nabla \cdot [D_v \nabla C_v + \frac{D_v C_v}{kT} \nabla U_v] + G_v - RC_v C_i - \sum_j K_v^j C_v = \frac{\partial C_v}{\partial t} \qquad (2.26)$$

$$\nabla \cdot [D_i \nabla C_i + \frac{D_i C_i}{kT} \nabla U_i] + G_i - RC_v C_i - \sum_j K_i^j C_i = \frac{\partial C_i}{\partial t} \qquad (2.27)$$

where v,i subscripts = vacancies and interstitials, respectively

K^j = rate constants for losses at sinks

C = point defect concentrations

U = interaction energy at sinks

G = generation rate of point defects

R = recombination coeff. = $4\pi r_0(D_i + D_v)$ where r_0 is the radius of the point defect recombination value

k = Boltzmann's constant

T = absolute temperature

t = time

D = diffusion coefficient.

A close inspection of these equations reveals the fact that the model homogenizes the reactions that point defects undergo. That is, the rate constants, being independent of position in the medium model sinks that are in effect homogeneously distributed. This approach will smooth out any details of a sink.

Equations (2.26) and (2.27) are usually solved with the time derivative vanishing, i.e. the point defect concentrations respond very quickly compared to any sink change.

Recently Mansur$^{(67)}$ gives the growth rate of a void of radius r_v:

$$\frac{dr_v}{dt} = \frac{\Omega}{r_v} [Z_v^v(r_v)D_v[C_v - C_v^e(r_v)] - Z_i^v(r_v D_i C_i)] \qquad (2.28)$$

where r_v = void radius

$C_v^e(r_v)$ = thermal equilibrium vacancy concentration at a void radius $r_v = C_v^e \exp(-(P_g - \frac{2\gamma}{r_v}) \frac{\Omega}{kT})$ where C_v^e is the bulk thermal vacancy density, P_g is the gas pressure in the void, and γ is the void-matrix surface tension

Ω = atomic volume

$Z_{v,i}^v(r_v)$ = capture efficiency for vacancies or interstitials at a void radius r_v.

Also

$$K = S(Z) \cdot D \tag{2.29}$$

where S = sink strength. Growth equations for dislocation loops are similar.(67)

If one considers that the effect of impurities is to bind or "trap" the point defects, a new approach must be taken for the growth kinetics framework. Johnson and Lam,(68) Schmidt and Sprague,(69) and Mansur(67) have all modeled the growth of voids while considering possible trapping of vacancies and interstitials at solutes or impurities that are immobile. Again, outlining the treatment by Mansur for immobile traps, new point defect balances are obtained for free interstitials:

$$G_i + C_i^T \tau_i^{-1} - R^F C_i^F C_v^F - R^{FT} C_i^F C_v^T - C_i^F \nu_i - \sum_j K_i^j C_i^F = 0 \tag{2.30}$$

for trapped interstitials:

$$C_i^F \nu_i - C_i^T \tau_i^{-1} - R^{TF} C_i^T C_v^F = 0 \tag{2.31}$$

for free vacancies:

$$G_v + C_v^T \tau_v^{-1} - R^F C_i^F C_v^F - R^{TF} C_i^T C_v^F - C_v^F \nu_v - \sum_j K_v^j C_v^F = 0 \tag{2.32}$$

for trapped vacancies:

$$C_v^F \nu_v - C_v^T \tau_v^{-1} - R^{FT} C_i^F C_v^T = 0 \tag{2.33}$$

where G = point defect generation rate

C^T = concentration of trapped defects

C^F = concentration of free defects

R^F = $4\pi r_1(D_i + D_v)$ = recombination coefficient between free vacancies and free interstitials

R^{FT} = $4\pi r_2 D_i$ = recombination coefficient between trapped vacancies and free interstitials

R^{TF} = $4\pi r_3 D_v$ = recombination coefficient between free vacancies and trapped interstitials

$\sum_j K^j C^F$ = losses of free defects to sinks (voids, dislocations, and grain boundaries)

τ = $\tau_o \exp(E_d/kT)$ = lifetime of the defect in the trapped state, and $E_d = E_m + E_b$ where E_m = defect migration energy and E_b = defect binding energy

ν = $4\pi D r_3 C_t$ = defect trapping rate

C_t = trap concentration

D = diffusion coefficient of the free defect

Qualitatively, the effect of traps is to reduce the steady state concentration of the defect being trapped and thereby reduce the void/loop growth rate.

Another effect of solute atoms is to change the bias or capture efficiency of the defect sinks in Eqs. (2.27) and (2.28). This would then alter the concentration of free defects.

Further analyses of solutes and impurities(68-70) allow for mobile traps. Temperature effects in the trapping show that traps are more effective at high temperatures where the traps slow down the mobile point defects while never becoming saturated.(69)

B. Phase Evolution Under Irradiation

The microstructural and microcompositional response of an alloy system to irradiation is largely controlled by the highly interrelated phenomena of solute-defect trapping, solute segregation, phase stability and void swelling. The result of altering the initial alloy microstructure through irradiation may allow the onset of a high rate of void swelling.(73,74) The physical processes which connect irradiation phase or microcompositional instabilities with void swelling have been outlined by Mansur et al.(75) and are shown in Fig. 2.2. There are three modes by which solute segregation and precipitation can influence the swelling response of a material. Direct effects on swelling by precipitates include increased point defect collection area for cavities attached to precipitates.(75,76)

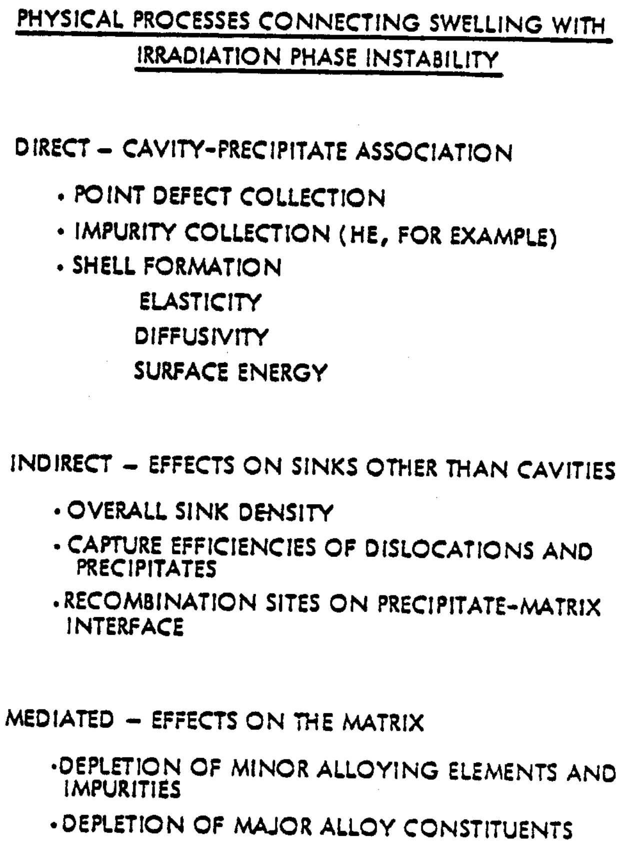

PHYSICAL PROCESSES CONNECTING SWELLING WITH IRRADIATION PHASE INSTABILITY

DIRECT – CAVITY-PRECIPITATE ASSOCIATION

- POINT DEFECT COLLECTION
- IMPURITY COLLECTION (HE, FOR EXAMPLE)
- SHELL FORMATION
  - ELASTICITY
  - DIFFUSIVITY
  - SURFACE ENERGY

INDIRECT – EFFECTS ON SINKS OTHER THAN CAVITIES

- OVERALL SINK DENSITY
- CAPTURE EFFICIENCIES OF DISLOCATIONS AND PRECIPITATES
- RECOMBINATION SITES ON PRECIPITATE-MATRIX INTERFACE

MEDIATED – EFFECTS ON THE MATRIX

- DEPLETION OF MINOR ALLOYING ELEMENTS AND IMPURITIES
- DEPLETION OF MAJOR ALLOY CONSTITUENTS

Fig. 2.2 Three classes or modes by which precipitation may affect swelling under irradiation.

Large, incoherent precipitates can efficiently collect vacancies to allow rapid growth of attached cavities. In addition, solute segregation to a subcritical void embryo can reverse the void bias for interstitials(77) by the formation of a "void coating."(41,78) This enhanced solute coating can cause an increase in the local lattice parameter near the void and thereby create a compressive coherency strain field to help repel interstitials. Also, a further interstitial barrier is formed with an increase in the shear modulus which increases the interstitial formation energy, which would reduce the flux of interstitials to that sink.

The existence of recombination sites at solute atoms or on precipitate-matrix interfaces will have an indirect effect on the cavity swelling. The increase in recombination of vacancies and interstitials will reduce the amount of void swelling.(79) Also, local composition differences at sinks may affect the sink efficiencies (e.g., provide a reaction barrier) and thus modify the sink bias.(80)

The matrix chemistry of an alloy system can also control void swelling. Garner has shown that matrix depletion of some impurity elements such as Si and C(81) as well as the major alloying element Ni(82,83) leads to the onset of a high level of cavity swelling in 316 SS. Silicon is efficient at suppressing nucleation at all void-relevant temperatures(84) while in the 316 SS matrix. The model(85) developed to explain silicon's role in pure metals is based on its higher diffusivity compared to that of the host metal increases D^v_{eff}. This is also shown in Fe-Ni-Cr alloys where small additions of silicon(86-88) substantially increase the diffusivities of all components and thereby decrease the void nucleation rate, particularly at higher temperatures.(85) Similarly, additions of nickel, a slow diffuser, to Fe-Ni,(89) Fe-Ni-Cr,(86) and Fe-Ni-Cr-Mo(90) alloys increases the diffusivity of all alloy components.

B.1. Precipitate Classification

The precipitates that form under irradiation may be classified as "radiation-enhanced," "radiation-induced," or "radiation-modified."(91) Following the terminology put forth by Wilkes,(92) "radiation-enhanced" refers to a phase that forms after shorter times than a thermally-aged specimen would show. These phases remain under post-irradiation annealing. "Radiation-induced" refers to a phase that is found only on remote regions of the phase diagram or is not a thermally stable phase at all. Post-irradiation annealing at the irradiation temperature will dissolve this phase. "Radiation-modified" refers to a phase that has a composition different than that produced during thermal-aging studies.

These phases may occur through one or more of the following processes:

1. Radiation-enhanced diffusion as a result of an increased vacancy concentration during irradiation.
2. Radiation-induced solute segregation processes which redistribute alloying elements to create local supersaturations.

3. Point defect supersaturations may alter the thermodynamic free energy of a phase and thus effectively shift thermal equilibrium phase boundaries of an alloy during irradiation.
4. "Mixing" processes occurring in the collision cascade can directly dissolve small precipitates as well as cause disorder dissolution.

A full theoretical treatment of phase stability phenomena can be found in various review articles.(92-96)

B.2. Enhanced and Induced Solute Segregation

Solute transport during irradiation is effected through radiation-enhanced diffusion or through solute-defect coupling transport mechanisms.

Radiation-enhanced diffusion is basically the result of the increased point defects present in the matrix during the irradiation.(97-100) The total diffusion coefficient of a solute atom during irradiation may be simply written:

$$D' = D_r + D_v^o \tag{2.34}$$

where D_r is that contribution to the diffusion coefficient due to the irradiation.

If diffusion occurs through a vacancy mechanism, the diffusion coefficient may be written:

$$D_v' = C_v f d^2 \tag{2.35}$$

where C_v is the prevailing matrix vacancy concentration, f is the effective jump frequency, and d is the jump distance.(97) It is easily seen that irradiation of a material alters D_v' through the increase in C_v. The dependence of D' on temperature and sink strength divides D' into three regimes: (1) at high temperatures (> 0.5 T_m), the contribution of thermal vacancies overrides the effect of vacancies produced by the irradiation and thermal diffusion dominates; (2) at intermediate temperatures where defects are primarily lost to fixed sinks, C_v is given by G/K_v where G is the defect production rate and K_v is the total sink strength. Thus the diffusion coefficient is temperature independent and varies linearly with the displacement rate; and (3) at low temperatures the diffusion coefficient is proportional to $\sqrt{G}$ with an activation energy of $E_v^m/2$. This follows as a result of the dominance of mutual recombination of point defects.

If there exists an interaction between point defects and solute atoms and if a complex is formed that is mobile, a mechanism exists for solute transport. This solute-defect binding concept along with the increased point defect concentrations and currents are the basis for the two basic mechanisms of solute segregation. The first mechanism describes the mobile defect-solute complex concept,(68,101,102) whereas the second mechanism is the so-called inverse Kirkendall effect.(103,104)

Anthony(105) predicted specific cases of the two mechanisms for solute segregation in 1972. He stated that a preferential exchange of one type of solute with a vacancy would tend to cause a depletion at a vacancy sink for this type of solute atom while causing an effective enhancement for the other types of solutes. Also if a solute and a vacancy could bind together and yet be mobile, this would also cause an enrichment of that solute at the sink for the complex.

Johnson and Lam(68,102) considered interstitial-solute and vacancy-solute complexes. The binding energy of these complexes depends on the solute-solvent size difference. Johnson-Lam theory predicts the extent of solute segregation to a void surface is dependent on the curvature of the void surface and on the interstitial-solute migration energy.

Wiedersich et al.(106) modified (vacancy-solute binding was abandoned) the Johnson-Lam theory to explain segregation in concentrated alloys. The concept of vacancy binding to solute atoms is only meaningful if the solute is dilute, otherwise the vacancy would be surrounded by more than one solute atom.(104) A vacancy binding mechanism would only be valid for the minor alloying elements or impurities in 316 SS.

For the major alloying elements, the inverse Kirkendall effect would be a viable mechanism for solute segregation.(104,106) The effect is that the slower diffusing species is "left behind" as the faster diffusing species moves away. This behavior is characteristic of a vacancy mechanism for diffusion whereas the faster diffuser would be enriched at the sink for a interstitial mechanism. Undersize solutes also tend to migrate towards sinks as they preferentially take the interstitial site in an exchange with an oversize interstitial.(46)

B.3. Precipitate Growth and Dissolution Under Irradiation

A model for change of size of precipitates under irradiation was proposed in 1972 by Nelson, Hudson and Mazey (NHM).(107) Their model considers growth from radiation enhanced diffusion, and shrinkage from two mechanisms. The first mechanism is recoil resolution of precipitate atoms. The equation describing the shrinkage of a precipitate from this sputtering off of precipitate atoms can be written:

$$\frac{dV}{dt} = -\left(\frac{1}{N}\right) 4\pi r^2 \phi \qquad (2.36)$$

where $\phi \sim 10^{14}$ G atoms/cm^{2}s, where G is the displacement rate, N is the atomic concentration and r is the radius of the precipitate.

The second mechanism of shrinkage of a precipitate is that of disorder dissolution. This mechanism is effective for coherent precipitates and acts through the "mixing" effect of the collision cascade. The high energy of the cascade area allows some reordering of the precipitate. However, the surface atoms of the precipitate tend to diffuse into the matrix thereby decreasing the size of the precipitate. Nelson et al. assumed a shell of thickness L in the precipitate is affected by the cascade ($L \approx 10$ nm) and only a fraction f of the atoms escape to the matrix. The equation describing such behavior is:

$$\frac{dV}{dt} = -4\pi r^2 fG \quad . \tag{2.37}$$

The radiation enhanced diffusion leads to a component of growth given by:

$$\frac{dV}{dt} = 3D'C_s \frac{r}{p} \tag{2.38}$$

where D' is the diffusivity of the precipitate component under irradiation, C_s is the solute concentration in solution and p is the atomic fraction of solute atoms in the precipitate.

Wilkes(92) stated that the Nelson et al. model cannot predict a final particle size distribution but rather gives a uniform (unrealistic) precipitate size. Wilkes shows that the assumptions made by NHM predict that precipitates shrink under irradiation until a steady-state matrix solute concentration is reached.

Baron et al.(108) has formulated a theory to predict the precipitate size distribution under irradiation which is based on precipitate coarsening theories as well as the physical ideas of the NHM model. The precipitate distribution is characterized by a maximum particle size with a related average particle size. The theory predicts a solute concentration in excess of the allowable thermal value. In addition, this theory predicts normal thermal coarsening behavior in the absence of irradiation.

Maydet and Russell(109) used in a nodal line critical point analysis in analyzing the change in precipitate size during irradiation.

The driving force for precipitate growth or dissolution in this theory is the strain energy of an incoherent precipitate in the matrix.(110) The rate of growth/dissolution depends on the rate of solute arrival, the rate of vacancy arrival to the precipitate, the rate of vacancy emission, and the rate of solute emission from the precipitate as well as the volumetric misfit of the precipitate. Maydet and Russell's theory does not apply to coherent precipitates and does not consider solute segregation. A recent modification to this model included the recoil resolution effects suggested by the NHM model.(111)

Another concept for a model to describe phase evolution under irradiation was that of a thermodynamic approach.(112,113) The effects of a supersaturation of point defects is to increase the free energy of the alloy system and thereby allow the existence of phases not normally found at the prevailing temperature. However, this model has been criticized(93) since the energy needed for the phase transformations (10-100 J/mole) is not met by the increased energy (~ 1 J/mole) due to the defect supersaturations.

A further consideration on the effects of excess point defects on radiation-induced phase restructuring has been undertaken by Yamauchi and de Fontaine.(114,115) They consider the equilibrium of an alloy and point defect system subject to linear constraints. Holloway and Stubbins(116) have reformulated the theory in a more rigorous manner and have studied the stability of selected phases in the presence of excess point defects for the Ni-Si, Fe-Cr, Fe-Ni and

Ni-Cr systems. These calculations shows that large changes in the relative stability of phases can indeed occur if different point defect concentrations are ascribed to the phases. This model provides an explanation for homogeneous precipitation of radiation-induced phases without the need for solute segregation processes which cause precipitation at sites where the solubility limit is exceeded.

References for Chapter 2

1. J. Lindhard and M. Scharff, Dan. Mat. Fys. Medd. 27, No. 15 (1953).
2. N. Bohr and J. Lindhard, Dan. Mat. Fys. Medd. 28, No. 7 (1954).
3. J. Lindhard and M. Scharff, Phys. Rev. 124, No. 1, 128-130 (1961).
4. J. Lindhard et al., Mat. Fys. Medd. Dan. Vid. Selsk. 33, No. 10 (1963).
5. J. Lindhard et al., Mat. Fys. Medd. Dan. Vid. Selsk. 33, No. 14 (1963).
6. J. Lindhard, Phys. Letters 12, No. 2, 126-128 (1964).
7. K.B. Winterbon et al., Mat. Fys. Medd. Dan. Vid. Selsk. 37, No. 14 (1970).
8. I. Manning and G.P. Mueller, Computer Physics Comm. 7, 85-94 (1974).
9. D.K. Brice, SAND75-0622, July 1977.
10. O.S. Oen et al., in Applications of Ion Beams to Metals, (1974), p. 639-650.
11. J.B. Roberto and J. Narayan, in CONF-751006-P1, (1975), pp. 120-126.
12. J. Narayan et al., J. Nucl. Mat. 71, 160-170 (1977).

13. J.B. Whitley, Ph.D. Thesis, University of Wisconsin, Madison, Wisconsin (1978).

14. D.B. Bullen, Ph.D. Thesis, University of Wisconsin, Madison, Wisconsin (1984).

15. S.J. Zinkle, Ph.D. Thesis, University of Wisconsin, Madison, Wisconsin (1985).

16. D.K. Brice, Phys. Rev. A6, 1791 (1972).

17. G.L. Kulcinski et al., Rad. Effects 7, 195-202 (1971).

18. M.T. Robinson, Nuclear Fusion Reactors, British Nuclear Energy Society, London, (1970), p. 364.

19. I.M. Torrens and M.T. Robinson, Irradiation Induced Voids in Metals, AEC Conf. (1971), p. 739.

20. J.H. Kinney et al., J. Nucl. Mat. 122 & 123, (1984).

21. M.J. Makin et al., J. Nucl. Mat. 68, 161-167 (1977).

22. ASTM Standard E521, Annual Book of ASTM Standards, Part 45.

23. D.K. Brice, "Ion Implantation Range and Energy Deposition Codes COREL, RASE4, and DAMG2," SAND77-0622 (1977).

24. J.R. Beeler and M.F. Beeler, Fundamental Aspects of Radiation Damage in Metals, CONF-751006 (1975).

25. M.W. Guinan and J.H. Kinney, J. Nucl. Mat. 103 & 104, 1319-1324 (1981).

26. H.L. Heinisch, J. Nucl. Mat. 117, 46-54 (1983).

27. S.D. Harkness and C.Y. Li, Radiation Damage in Reactor Materials, Vol. 2, IAEA, (1969), p. 189.

28. R. Bullough and R.C. Perrin, Ibid., p. 233.

29. K.C. Russell, Acta Met. 26, 1615-1629 (1978).

30. W.G. Wolfer, ASTM STP 725 (1980).

31. J.L. Katz and H. Wiedersich, J. Chem. Phys. 55, 1414 (1971).

32. K.C. Russell, Acta Met. 19, 753 (1971).

33. S.I. Maydet and K.C. Russell, Scripta Met. 14, 383 (1980).

34. K.C. Russell and R.W. Powell, Acta Met. 21 (March 1973).

35. K. Farrell, Rad. Effects 53, 175-194 (1980).

36. A.J.E. Foreman, "Role of Inert and Reactive Gases in Void Nucleation," in Proceedings BNES Symposium on Dimensional Stability and Mechanical Behavior of Irradiated Metals and Alloys, Brighton, England (1983).

37. N.H. Packan and K. Farrell, J. Nucl. Mat. 78, 143 (1978).

38. L.K. Mansur, M.H. Yoo and W.A. Coghlan, ANS paper at Winter Meeting, San Francisco (1977).

39. V. Levy et al., in Proceedings of the Intern. Conf. on Rad. Effects in Breeder Reactor Struct. Mat., (1977).

40. R.A. Johnson and N.Q. Lam, Phys. Rev. B13, No. 10, 4364-4375 (1976).

41. A. Si-Ahmed and W.G. Wolfer, ASTM STP 782, (1982).

42. W.G. Wolfer and L.K. Mansur, UWFDM-329 (1979).

43. A.D. Brailsford, J. Nucl. Mat. 56, 7 (1975).

44. L. Laour et al., ASTM STP 782, 310 (1982).

45. L. Boulanger et al., in Ref. 36, paper 2.

46. P.R. Okamoto and H. Wiedersich, J. Nucl. Mat. 53, 336 (1974).

47. R. Bullough et al., in Ref. 36, paper 16.

48. G. Ayrault et al., J. Nucl. Mat. 103 & 104, 1035 (1981).

49. S. Wood et al., ASTM STP 725, 455-469 (1981).

50. N.H. Packan and K. Farrell, ASTM STP 782 (1982).

51. P.J. Maziasz, J. Nucl. Mat. 85 & 86, 713 (1979).

52. W.J.S. Yang, in Phase Stability During Irradiation, J.R. Holland, L.K. Mansur and D.I. Potter (Eds.), TMS-AIME, (1980), p. 257.

53. P.J. Maziasz et al., Ibid., p. 271.

54. E.A. Kenik and E.H. Lee, Ibid., p. 493.

55. J.L. Katz and H. Wiedersich, J. Nucl. Mat. 46, 41-45 (1973).

56. K.C. Russell, Scripta Met. 7, 755-760 (1973).

57. W.G. Wolfer, ASTM STP 725, 201 (1981).

58. C.A. Parker and K.C. Russell, ASTM STP 782, 1042 (1982).

59. R.C. Pillar and A.D. Marwick, J. Nucl. Mat. 83, 42 (1979).

60. W.G. Wolfer et al., in Intern. Conf. of Rad. Effects in Breeder Reactor Struct. Mat., (1977), pp. 841-864.

61. M.F. Wehner and W.G. Wolfer, "Vacancy Cluster Evolution in Metals Under Irradiation," UWFDM-590, to be published in Phil. Mag. A.

62. M.F. Wehner and W.G. Wolfer, Phys. Rev. A 27, 2663 (1983).

63. M.F. Wehner and W.G. Wolfer, Phys. Rev. A 27, 3003 (1983).

64. A.D. Brailsford and R. Bullough, J. Nucl. Mat. 44, 121 (1972).

65. H. Wiedersich, Rad. Effects 12, 111 (1972).

66. S.D. Harkness and C.Y. Li, Met. Trans. 2, 1457 (1971).

67. L.K. Mansur, Nucl. Tech. 40, 5 (1978).

68. R.A. Johnson and N.Q. Lam, Phys. Rev. B13, 4364 (1976).

69. F.A. Schmidt and J.A. Sprague, Scripta Met. 7, 495 (1973).

70. P.R. Okamoto et al., J. Nucl. Mat. 69 & 70, 821 (1978).

71. N. Lam et al., J. Nucl. Mat. 74, 101 (1978).

72. L.K. Mansur, J. Nucl. Mat. 83, 109 (1979).

73. W.G. Wolfer, F.A. Garner and L.E. Thomas, ASTM STP 782, 1023 (1982).

74. F.A. Garner and W.G. Wolfer, J. Nucl. Mat. 122 & 123, 201 (1984).

75. L.K. Mansur, M.R. Hayns and E.H. Lee, in "Phase Stability During Irradiation," J.R. Holland, L.K. Mansur and D.I. Potter, Eds., TMS-AIME, Oct. 1980, p. 359.

76. L.K. Mansur, Phil. Mag. A 44, 867 (1981).

77. W.G. Wolfer, L.K. Mansur and J.A. Sprague, in "Radiation Effects in Breeder Reactor Structural Materials," M.L. Bleiberg and J.W. Bennett, Eds., TMS-AIME, (1977), p. 841.

78. W.G. Wolfer and L.K. Mansur, J. Nucl. Mat. 91, 265 (1980).

79. P.R. Okamoto, N.Q. Lam and H. Wiedersich, Proc. of the Workshop on Correlation of Neutron and Charged Particle Damage, J.O. Stiegler, Ed., CONF-760673, p. 111, ORNL (June 1976).

80. L.K. Mansur and W.G. Wolfer, Proc. Intern. Conf. on Properties of Atomic Defects in Metals, Argonne National Laboratory (October 1976).

81. H.R. Brager and F.A. Garner, Proc. AIME Symp. on Phase Stability During Irradiation, (1980), p. 219.

82. W.G. Wolfer, F.A. Garner and L.E. Thomas, in Effects of Radiation on Materials: Eleventh Conference, H.R. Brager and J.S. Perrin, Eds., ASTM STP 782, 1023-1041 (1982).

83. F.A. Garner and W.G. Wolfer, J. Nucl. Mat. 122 & 123, (1984).

84. H.R. Brager and F.A. Garner, in "Phase Stability During Irradiation," J.R. Holland, L.K. Mansur and D.I. Potter, Eds., TMS-AIME, (October 1980), p. 219.

85. F.A. Garner and W.G. Wolfer, J. Nucl. Mat. 102, 143 (1981).

86. S.J. Rothman, L.J. Nowicki and G.E. Murch, J. Phys. F 10, 383 (1980).

87. W. Assassa and P. Guiraldenq, Metal Science, 123 (1978).

88. G.B. Fedorov, A.N. Semenikhin, Metallurgy and Metallography of Pure Metals Moscow, Vol. II, 252 (1960).

89. B. Million et al., Mater. Science and Engr. 50, 43 (1981).

90. L.V. Pavlinov, Fiz. Metal. Metalloved. 41, No. 2, 344 (1976).

91. E.H. Lee et al., in "Phase Stability During Irradiation," J.R. Holland, L.K. Mansur and D.I. Potter, Eds., TMS-AIME, p. 191 (Ocotber 1980).

92. P. Wilkes, J. Nucl. Mater. 83, 166 (1979).

93. K.C. Russell, J. Nucl. Mater. 83, 176 (1979).

94. K.C. Russell, in "Radiation Effects in Breeder Reactor Structural Materials," M.L. Bleiberg and J.W. Bennett, Eds., TMS-AIME, p. 821 (1977).

95. J.A. Hudson, in "Precipitation Processes in Solids," TMS-AIME, p. 284 (1978).

96. H.J. Frost and K.C. Russell, in "Phase Transformations and Solute Redistribution in Alloys During Irradiation," Res. Mechanica, (1982).

97. G.J. Dienes and A.C. Damask, J. Appl Phys. 29, No. 12, 1713-1721 (1958).

98. A.C. Damask, in "Radiation Damage in Solids," D.S. Billington, Ed., pp. 763-776 (1962).

99. Y. Adda, M. Beyeler and G. Brebec, Thin Solid Films 25, 107-156 (1975).

100. R. Sizman, J. Nucl. Mater. 69 & 70, 366-412 (1968).

101. R.A. Johnson and N.Q. Lam, J. Nucl. Mater. 69 & 70, 424 (1978).

102. R.A. Johnson and N.Q. Lam, Phys. Rev. B 15, No. 4, 1794 (1977).

103. P.R. Okamoto and L.E. Rehn, J. Nucl. Mater. 83, 2 (1979).

104. A.D. Marwick, J. Phys. F: Metal. Phys. 8, No. 9, 1849 (1978).

105. T.R. Anthony, in "Radiation Induced Voids in Metals," J.W. Corbett and L.C. Ianniello, Eds., p. 730 (1972).

106. H. Wiedersich, P.R. Okamoto and N.Q. Lam, J. Nucl. Mater. 83, 98 (1979).

107. R.S. Nelson, J.A. Hudson and D.J. Mazey, J. Nucl. Mater. 44, 318 (1972).

108. M. Baron, A. Chang and M.L. Bleiberg, in "Radiation Effects in Breeder Reactor Structural Materials," M.L. Bleiberg and J.W. Bennet, Eds., (1977), p. 395.

109. S.I. Maydet and K.C. Russell, J. Nucl. Mater. 64, 101 (1977).

110. M.R. Mruzik and K.C. Russell, J. Nucl. Mater. 78, 343 (1978).

111. H.J. Frost and K.C. Russell, Acta Met. 30, 953 (1982).

112. P. Wilkes et al., Radiation Effects 29, 249 (1976).

113. L. Kaufman et al., Calphad, 281 (1977).

114. H. Yamauchi and D. de Fontaine, Research Report UCB-ENG-DDF7902, University of California, Berkeley (1979).

115. H. Yamauchi and D. de Fontaine, in "Phase Stability During Irradiation," J.R. Holland, L.K. Mansur and D.I. Potter, Eds., TMS-AIME (1981).

116. J.P. Holloway and J.F. Stubbins, J. Nucl. Mater. 122 & 123, 591 (1984).

CHAPTER 3. REVIEW OF THERMAL STUDIES AND ION IRRADIATIONS OF 316 SS

A. Thermal Studies of 300-Series Austenitic Steels

The initial solution-treated state of the 300 series austenitic stainless steels is thermodynamically unstable and therefore thermomechanical treatments can change the initial microstructure to promote precipitation of various carbide and intermetallic phases. As discussed in Chapter 2, radiation can also strongly influence the normal track of phase evolution of an alloy.

In order to determine the effects of irradiation and to classify phase evolution under irradiation as radiation-enhanced, radiation-induced or radiation-modified, extensive thermal aging studies must be reviewed over a wide range of temperatures that include the irradiation temperatures. These studies must also carefully specify the initial state of the material to include the grain size, degree of cold work, precipitate characteristics, solute and impurity content.

A.1. Phases Formed During Thermal Aging

The major precipitates found in 300-series steels are carbides ($M_{23}C_6$, M_6C and MC) and intermetallics (σ, χ and Laves). The crystal structure and lattice parameter for these phases along with the minor phases are summarized in Table 3.1.(1-11) Table 3.2 gives the relative intensity of the elemental composition determined using electron microprobe analysis of phases formed in thermally aged 316 SS.(6) Weiss and Stickler(4) employed a bulk extraction process along with

Table 3.1 (1-11)

Crystal Structures and Compositions of Phases in Austenitic Stainless Steels

Phase	*Crystal structure*	*Lattice parameters* (Å)	*Composition*
Austenite	fcc	$a_0 = 3\cdot598$	
Ferrite	bcc	$a_0 = 2\cdot85–2\cdot88$	FeCrMo
Carbides			
MC	fcc	$a_0 = 4\cdot45$ $a_0 = 4\cdot24$ (TiN) $a_0 = 4\cdot33$ (TiC)	NbC TiCTiN
M_2C		$a_0 = 4\cdot40$	(VTi)C
M_7C_3	pseudo hexagonal	$a_0 = 6\cdot928–6\cdot963$ $c_0 = 4\cdot541 - 4\cdot511$	Cr_7C_3; $(FeCr)_7C_3$; $(Fe\ 0\cdot6\ Cr\ 0\cdot4)_7C_3$
$M_{23}C_6$	fcc	$a_0 = 10\cdot57–10\cdot68$	$(Cr_{16}Fe_5Mo_2)C_6$; $(FeCr)_{23}C_6$; $Cr_{17}Fe_{4\cdot5}Mo_{1\cdot5})C_6$
M_6C	fcc (diamond type)	$a_0 \sim 10\cdot95–11\cdot28$	$(CrCoMoNi)_6C$; $(TiNi)_6C$; $(NbNi)_6C$; $(Fe_3Mo_3)C$
Nitrides			
M(CN)	fcc	$a_0 = 3\cdot1–5\cdot0$ (AlN) $a_0 = 4\cdot24$ (TiN)	Nb(C, N)Ti(CN)AlN
M_2N	hcp	$a_0 = 4\cdot78$, $c = 4\cdot44$	βCr_2N
MN		$a_0 = 4\cdot06 \pm 0\cdot03$	VN
M_2N		$a_0 = 4\cdot19$ (V Nb)	N
M_2NC		$a_0 = 4\cdot35$	
Boro carbides			
$M_{23}(CB)_6$	fcc	Similar to $M_{23}C_6$	$(FeCrMo)_{23}(CB)_6$
Borides			
M_3B_2		$a_0 \approx 5\cdot7$, $C \approx 3\cdot1$	
M_2B	orthorhombic	$a_0 \sim 14\cdot57$, $b = 7\cdot32$ $c = 4\cdot22$	
Topologically close-packed phases			
Sigma, σ	bcc tetragonal	$a_0 = 8\cdot7–9\cdot2$ $c = 4\cdot544–4\cdot8$	$(FeNi)_x(CrMo)_y FeCr$; $(FeNi)_x(CrMo)_y$
Laves, η	hexagonal	$a_0 = 4\cdot73–4\cdot74$ $c = 7\cdot72–7\cdot85$	Fe_2Mo; Fe_2Ti; Fe_2Nb
Chi, χ	bcc	$a_0 = 8\cdot807–8\cdot92$	$(FeNi)_{36}Cr_{18}Mo_4$; $Cr_6Fe_{18}Mo_5$; $Fe_{36}Cr_{12}Mo_{10}$
U	rhombohedral		$(CoTi)(CrW)_6$
G	fcc		$(TiZrVNbTaMn)(NiCo)_{16}Si_{17}$
R	hexagonal	$a_0 = 0\cdot93$ $c_0 = 19\cdot34$	Fe–Cr–Mo
Minor phases and impurities			
Sulphides			
$M_4S_2C_2$	hcp		$Ti_4S_2C_2$
MS	fcc	$a_0 = 5\cdot224$	MnS
Ti_2S	hcp	$a_0 = 3\cdot22$ $c = 7\cdot64$	Ti_2S
Spinel	diamond	$a_0 = 8\cdot51$	
Silicon carbide	hexagonal	$a_0 = 3\cdot076$ $c = 5\cdot048$	SiC
Titanium dioxide		$a_0 \sim 4\cdot6$ $c \sim 2\cdot96$	
Calcium silicate alumina	trigonal	$a_0 = 4\cdot759$ $c = 12\cdot99$	
Dimolybdenum carbide	hcp	$a_0 = 4\cdot72$, $b = 6$ $c = 5\cdot19$	
Y	hcp	$a_0 = 3\cdot206$ $c = 11\cdot19$	
τ	hcp	$a_0 = 3\cdot206$ $c = 11\cdot19$	

Table 3.2. EPMA Relative Intensities of the Element Lines Present in Extracted Phases (Cr = 100) of Type 316 Stainless Steel Following Thermal Aging(6)

	Fe/Cr	Ni/Cr	Mo(L)/Cr	V/Cr
$M_{23}C_6$	12-30	1-4	10-17	---
$M_{23}C_6$	48-56	---	---	---
$M_{23}C_6$	47	2	13	---
M_6C	11-22	55-79	37-55	1-7
M_6C	50	120	200	3
σ	121-137	8-11	16-29	---
χ	173-185	10-12	45-56	---
Laves	226-291	16-26	197-289	---
M_3B_2	41-42	1-2	170-172	2
M_2B	27	---	5	---

Table 3.3. Composition (wt.%) of Phases Formed in 316 SS Following Thermal Aging.(4) Composition Determined From Relative X-Ray Intensities Using Standard X-Ray Powder Diffraction Techniques

	Mo	Cr	Fe	Ni
$M_{23}C_6$	14	63	18	5
σ	11	29	55	5
χ	22	21	52	5
Laves	45	11	38	6

x-ray powder diffraction techniques to arrive at the elemental composition of 316 SS phases in Table 3.3. Stoter(8) has recently investigated phases of 316 SS present after 30,000 hours of aging at 650°C. Results of the EDS analysis of the extracted phases is shown in Fig. 3.1.

A.1.1. Carbide Precipitation

Silcock(12) has determined the carbon solubility for several stabilized and unstabilized austenitic stainless steels. Equation (3.1) below indicates that for solution-annealing temperatures of 1000°C or greater substantial amounts of carbon are dissolved in austenite. When these steels are rapidly cooled, the dissolved carbon remains in solution. However, when these supersaturated steels are thermally aged, carbide precipitation occurs.

Carbon Solubility in Type 316 SS

$$\log\text{ (C ppm)} = 7.771 - \frac{6272}{T(K)} \qquad (3.1)$$

A.1.1.1. $M_{23}C_6$ Carbide

$M_{23}C_6$ is the predominant carbide formed in the 300 series austenitic stainless steels in the absence of stabilizing elements (Ti, Nb, Ta). Stoter(8) has suggested that embrittlement of 316 SS after 30,000 hours at 650°C was due to the intergranular $M_{23}C_6$ precipitation.

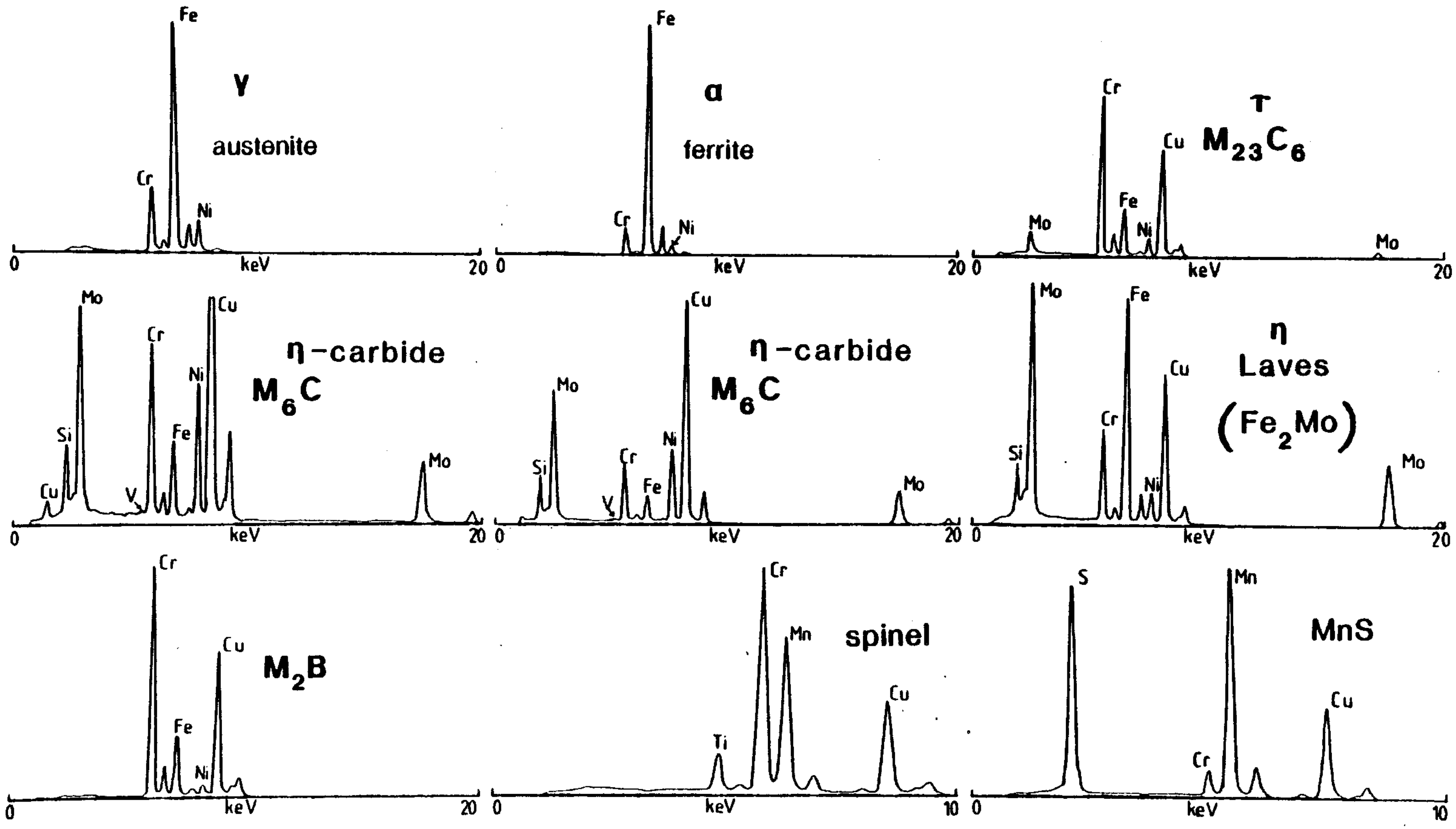

Fig. 3.1. EDS spectra from extracted precipitates in thermally-aged 316 SS.(8)

Weiss and Stickler(4) found solution-treated 316 SS caused $M_{23}C_6$ to precipitate successively at grain boundaries, incoherent twin boundaries and nonmetallic inclusions, coherent twin boundaries, and finally intragranularly. The appearance sequence for $M_{23}C_6$ in cold-worked material was first at grain boundaries and intersections of faults, incoherent twin boundaries, coherent twin boundaries, and finally along dislocation lines and in the fault planes. Marshall(13) gives a detailed review on the formation of $M_{23}C_6$. Table 3.4 lists the precipitate morphology and orientation relationship for $M_{23}C_6$ along with the other phases observed in aged 316 SS.

A.1.1.2. M_6C Carbide

This phase is called the η-carbide and is found in steels containing molybdenum or niobium. Lee et al.(14) state that the thermal formation of this phase in 316 SS is confined to the temperature range 560-650°C. Two possible types of structure are reported for this phase.(14) The filled type is given by M_6X with X = C, N, O whereas the unfilled type is M_5SiX with the X site vacant.

The M_6C phase appears in 316 SS after long aging times(4) with the proposed reaction sequence given by:(4,15)

$$M_{23}C_6 \xrightarrow[\sim 650^{\circ}C]{+Mo} (FeCr)_{21}Mo_2C_6 \xrightarrow{+Mo} M_6C \ . \qquad (3.2)$$

Maziasz(16) has found various orientation relationships with the austenite matrix for the M_6C phase and suggests that the differing

Table 3.4 Precipitate Morphology and Orientation of Thermal Phases in AISI Type 316 Stainless Steel

PHASE	TYPICAL MORPHOLOGY	PARALLEL PLANES	RATIO OF PPT. TO MATRIX INTERPLANAR SPACINGS (d'_{ppt}/d_{γ})
$M_{23}C_6$	Rhombohedral Platelet	$[100]_{M_{23}C_6} \parallel [100]_{\gamma}$ $[110]_{M_{23}C_6} \parallel [110]_{\gamma}$	$d'_{100}/d_{100} = 2.95$ $d'_{110}/d_{110} = 2.95$
M_6C	Rhombohedral	$(101)_{M_6C} \parallel (111)_{\gamma}$*	$d'_{101}/d_{111} = 3.08$
Laves	Faulted Lath	$(00.1)_{Laves} \parallel (231)_{\gamma}$* $(00.1)_{Laves} \parallel (\bar{3}12)_{\gamma}$* $(21.0)_{Laves} \parallel (1\bar{1}1)_{\gamma}$	$d'_{00.1}/d_{231} = 8.04$ $d'_{00.1}/d_{\overline{312}} = 8.04$ $d'_{21.0}/d_{1\bar{1}1} = 1.14$
χ	Various	$(011)_{\chi} \parallel (111)_{\gamma}$** $(111)_{\chi} \parallel (011)_{\gamma}$** $(0\bar{1}1)_{\chi} \parallel (0\bar{1}1)_{\gamma}$**	$d'_{011}/d_{111} = 3.02$ $d'_{\bar{1}11}/d_{011} = 2.01$ $d'_{0\bar{2}2}/d_{0\bar{1}1} = 5.0$
σ	Various	$(110)_{\sigma} \parallel (1\bar{1}1)_{\gamma}$ $(100)_{\sigma} \parallel (\bar{1}\bar{1}0)_{\gamma}$	$d'_{110}/d_{1\bar{1}1} = 3.0$ $d'_{100}/d_{1\bar{1}0} = 3.46$

* = not exactly parallel, a slight angular displacement
** = several degrees from parallel

orientations correspond to different chemical compositions of the phase.

A.1.2. Intermetallic Precipitation

A.1.2.1. σ Phase

The σ phase is an intermetallic phase with a tetragonal crystal structure. The nominal composition usually found is FeCr although Lai(17) has determined the composition (wet chemical analysis) of σ extracted from 316 SS to be 54 Fe-29 Cr-8 Mo. A similar composition was seen by Bolton et al.(5,6) Hall and Algie have reviewed the subject of σ phase formation.(18)

Weiss and Stickler(4) saw σ appear in 316 SS beginning sequentially at triple points, grain boundaries, and after longer times and higher temperatures at incoherent twin boundaries, and finally intragranularly, nucleating on oxide inclusions. Therefore σ phase appears to require a high-energy interface for nucleation. Goldschmidt(15) suggested that σ phase formed from the decarbonization of $M_{23}C_6$ and Weiss and Stickler(4) observed σ phase on $M_{23}C_6$. However, Duhaj et al.(19) and Blenkinsop and Nutting(20) observed nucleation of σ phase independent of $M_{23}C_6$.

A.1.2.2. Chi Phase (χ)

The χ phase behaves either as an intermetallic compound or as a carbide of the type $M_{18}C$. It has a bcc α-Mn type crystal structure(14) and is usually associated with σ phase. The nucleation sequence begins at grain boundaries followed by incoherent twin boundaries, and after long aging time, intragranularly. The morphology of the χ phase ranges from rod-shaped to globular massive particles.

A.1.2.3. Laves Phase (η)

Laves is an intermetallic phase with a hexagonal crystal structure. It has the composition AB_2 with Fe_2Mo the composition usually found in 316 SS. Weiss and Stickler(4) found Laves phase to precipitate intragranularly as equiaxed particles or as clusters of particles. Occasionally it was found on grain boundaries.

A.2. Time-Temperature-Precipitation in 316 SS

Weiss and Stickler(4) carried out an extensive investigation over a 400-900°C temperature range to determine the time-temperature-precipitation (TTP) diagrams as a function of carbon content, solution treatment temperature, and effect of cold work for 316 SS. Figure 3.2 shows the TTP diagram obtained from the thermal aging of 316 SS whose pretreatment was a solution annealed at 1260°C for 1.5 hours followed by a water quench. Spruiell et al.(21) has found that a pretreatment of a solution anneal at 1050°C gives a similar initial microstructure and TTP diagram. The effect of cold work is to shift the "C-curves" of the $M_{23}C_6$ carbide and the intermetallic phases (Laves, χ and σ) towards shorter times.(21) Grot and Spruiell(22) found type 316 modified with titanium suppressed $M_{23}C_6$ formation but accelerated σ and χ formation compared to 316 SS.

A.3. Phase Evolution

The partial overlapping of the regions in the TTP diagram indicates that the evolutionary sequence of the phases is complex in

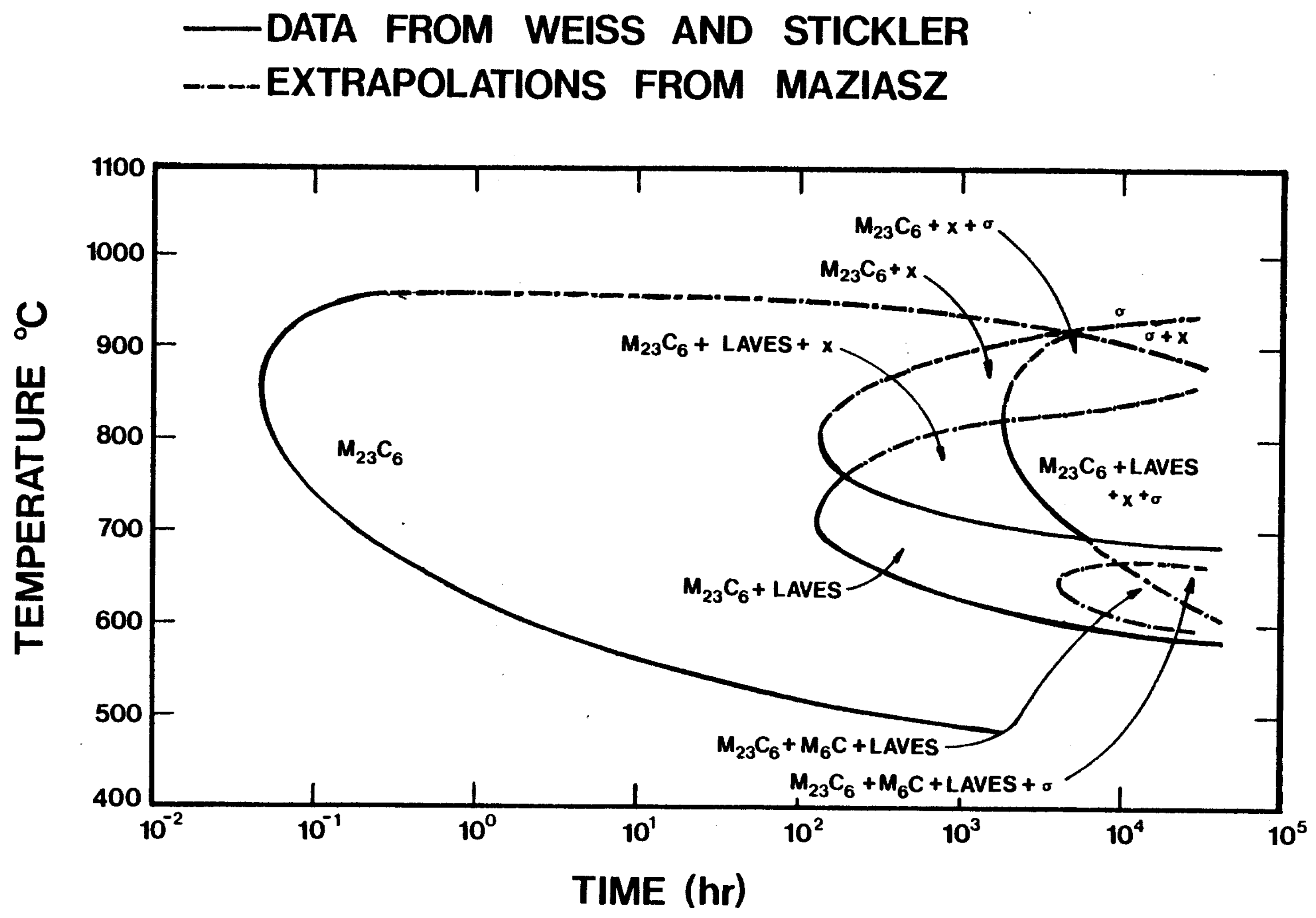

Fig. 3.2. TTP diagram as determined by Weiss and Stickler(4) with extensions from Maziasz.(16) The pretreatment involved a 1260°C solution quench of the 316 SS.

thermally-aged 316 SS. Figure 3.3 shows the phase reaction sequence proposed by Weiss and Stickler for the thermal aging of solution-quenched 316 SS. Lai(17) gives a detailed model of the precipitation kinetics of 316 SS.

B. Ion-Irradiation Studies of 316 SS

There have been numerous heavy-ion irradiations of austenitic stainless steels and ternary alloys during the past fifteen years. Most of these studies have used nickel ions to create the displacement damage. Measurements of the resultant swelling have been performed using either step height techniques(23) which measure the integrated swelling along the damage range or conventional transmission electron microscopy of samples which were backthinned to observe the damage peak. However, interpretation of the results of step-height data can be misleading.(24)

Table 3.5 lists the results of the various heavy-ion irradiation studies(25-31) of nominal purity 316 SS. Hudson(26) performed an irradiation temperature scan at doses of 16 and 40 dpa and found a peak swelling temperature of ~ 650°C for 316 SS which had been preimplanted to 10 appm helium. Similar results were obtained by Lee et al.(31) (625°C) and Makin et al.(32) (650°C). In addition, Lee reported(31) that helium-free specimens also had a peak swelling temperature of ~ 625°C. This observation that samples of 316 SS with and without helium exhibit a similar peak swelling temperature was also reported by Johnston(31) and Nelson et al.(33) Nelson also noted that void formation did not occur in a titanium-modified steel

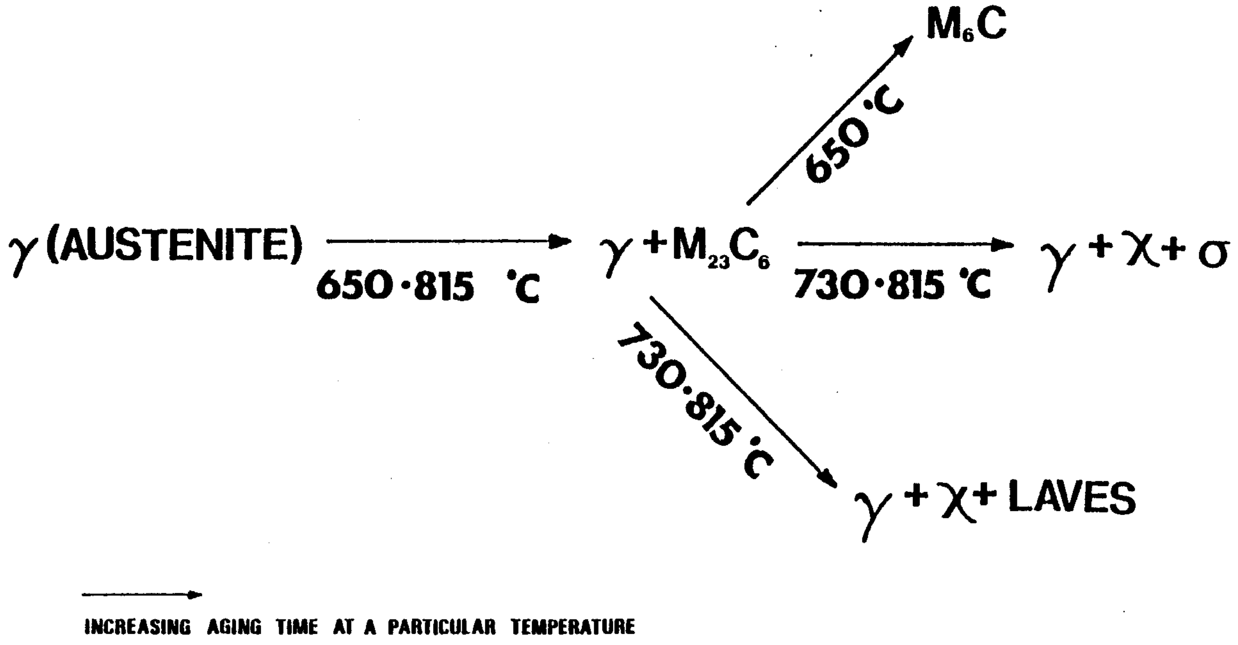

Fig. 3.3. Phase reaction sequence proposed by Weiss and Stickler(4) for the thermal aging of 316 SS.

Table 3.5. Heavy Ion Irradiations of 316 SS

316 SS Pretreatment	Ion Used	dpa	He appm	Temp. °C	N_v (10^{14} cm^{-3})	$\overline{d}$ (nm)	ΔV/V %	Ppt.	Ref.
4% CW	5 MeV Cu	30	0	500	60	18	1.8		25
S.A.	46.5 MeV Ni	16	10	525	---	---	0.1		26
		16	10	560	---	---	0.3		
		16	10	600	---	---	0.6		
		16	10	650	---	---	0.9	Some $M_{23}C_6$ at high doses	
		16	10	700	---	---	0		
		40	10	450	0	0	0		
		40	10	525	20	21	1.0		
		40	10	560	15	27	1.5		
		40	10	600	12	40	3.9		
		40	10	625	7.0	50	4.7		
		40	10	650	2.5	77	5.9		
		40	10	700	0.3	89	1.1		
S.A.	5 MeV Ni	50	0	625	0.2	45	0.15		27
		100	0	625	0.3	65	0.50		
		200	0	625	0.4	170	10		
		20	20	625	1.5	25	0.2		
		100	20	625	6.9	70	10		
		200	20	625	1.8	170	50		
			DUAL-BEAM						
S.A.	4 MeV Ni	1	10	625	---	---	0	$M_{23}C_6$ on grain boundaries. Unidentified thin lathe precipitate at low dose.	28
		10	100	625	15	18	1		
		100	1000	625	60	30	9		
		200	2000	625	40	40	20		

Table 3.5. Heavy Ion Irradiations of 316 SS (Continued)

316 SS Pretreatment	Ion Used	dpa	He appm	Temp. °C	N_v (10^{14} cm^{-3})	$\overline{d}$ (nm)	ΔV/V %	Ppt.	Ref.
			DUAL-BEAM						
S.A.	28 MeV Si	5	50	550	2.6	12.7	0.04	$M_{23}C_6$. Unidentified acicular ppt. with cavities attached to them.	29
		5	50	650	1.4	19.1	0.2		
20% CW		5	50	750	1.1	27.1	0.3		
			DUAL-BEAM						
S.A. and aged for 10 hrs. at 800°C	3 MeV Ni	2	10	625	1.5	12	0.05	$M_{23}C_6$. Unidentified acicular ppt.	30
		7	35	625	3.9	17	0.1		
		15	75	625	10	16	0.3		
		28	140	625	12	23	1.3		
		2	30	625	1.3	11	0.05		
		8	120	625	5.0	12	0.1		
		14	210	625	5.1	16	0.2		
		27	400	625	16	21	1.1		
		7	350	625	25	8	0.15		
		12	600	625	35	12	0.7		
		20	1000	625	42	13	1.5		
			DUAL-BEAM						
S.A.	4 MeV Ni	100	0	625	0.7	100	4.0	Carbides, not associated with voids.	31
		100	40	600	3	20	2.5		
		100	40	650	1	40	3.8		
		100	40	700	0.5	100	4.8		
		100	40	750	0.1	100	1.8		
		100	40	800	0	0	0		

free of helium. He postulated that the reactive gases present in 316 SS were sufficient for void nucleation whereas the titanium in the modified steel would act as a gettering agent for these gases. An additional specimen preimplanted with oxygen did indeed exhibit void swelling.

The precipitation response of 316 SS to ion-irradiation is difficult to identify. Packan and Farrell,(28) Wood et al.(29) and Ayrault et al.(30) have reported small (~ 100 nm) thin lathe or "acicular" precipitates to form during irradiation. Small cavities were often observed to form at the precipitate interface. Recent identification of this phase was reported by Lee et al.(34) Their ion-irradiation study of an austenitic stainless steel similar to 316 SS and with 0.2 wt.% titanium and 0.04-0.08 wt.% phosphorus has shown this thin-lathe precipitate (needle-like appearance) to be the Fe_2P phase with composition (wt.%) 16 Si-5 P-4 S-19 Cr-29 Fe-27 Ni. A post-irradiation anneal for 16 hours at the irradiation temperature of 675°C caused a partial dissolution of this phase.

There have also been reports(26,28-31) of the $M_{23}C_6$ carbide, a thermally induced phase, to form during irradiation. This phase is isostructural to the G-phase, a radiation-induced nickel silicide, and thus it is difficult to distinguish between the two phases.(35) Maziasz(36) has reported that the G-phase couples positively to radiation-induced segregation whereas the $M_{23}C_6$ carbide does not. That is, the large degree of radiation-induced nickel and silicon segregation suggests that the G-phase might form during irradiation rather than the $M_{23}C_6$.(36) Thus, the past reports of $M_{23}C_6$ are suspect without the chemical analysis of the phase.

C. Ion-Irradiation Studies of P7

The P7 alloy, a high purity austenitic stainless steel with major alloying composition similar to 316 SS (see Tables 4.1-4.3), has been studied following irradiation with single heavy ions (Ni), dual (Ni plus He) and triple beam (Ni, He and D) ions.(37-42) This alloy has also been neutron-irradiated(43) and studied following neutron and heavy-ion irradiation to a common dose.(44)

The P7 alloy swells readily(37) but does not undergo radiation-induced phase instability which would complicate the analysis of the irradiation studies on void formation. Table 3.6 lists the void parameters from the ion-irradiation studies of the P7 alloy. Bloom et al.(37) used step height techniques to determine the high levels of swelling following the high-dose irradiation of P7. The void parameters in the remainder of these studies were extracted from specimens backthinned to the damage peak. This places a large uncertainty on the dose level(42) due to the uncertainty of the depth of the swelling peak in the ion-irradiated foils.

Observations made from the dual-beam studies(38,39) include the enhancement of cavity nucleation with a concurrent reduction in average cavity size and swelling compared to the single-beam irradiation of P7. Co-implantation of hydrogen (deuterium) at a rate of 50 appm D/dpa simultaneously with the helium caused no apparent additional

Table 3.6. Void Parameters in Ion-Irradiated P7 Alloy

Ion Species	Ion Energy (MeV)	Peak Dose Rate (x 10^{-3} dpa/s)	Dose (dpa)	Irr. Temp. (°C)	Mean Diameter (nm)	Density (x 10^{15} cm^{-3})	Swelling (%)	Comments	Ref.
Ni^+	4.0	4 x 10^{-3}	100	635	---	---	38	single ion	37
"	"	"	210	"	---	---	82		
"	"	"	310	"	---	---	125	swelling determined by step height	
Ni	4.0	6.1	1	625	11	2.0	0.16	single ion	38
"	"	"	12	"	38	1.0	2.8	" "	
"	"	"	71	"	88	0.4	18	" "	
"	"	"	1	"	10	2.5	0.1	dual ion 200 appm He/dpa	
"	"	"	12	"	23	2.8	1.9	" "	
"	"	"	74	"	49	1.6	11	" "	
"	"	"	1	"	16	0.3	0.06	triple ion 20 appm He/dpa 50 appm D/dpa	
"	"	"	10	"	30	1.3	2.0	" "	
"	"	"	73	"	42	3.2	12.8	" "	
"	"	"	1	"	6.0	2.3	0.25	preinject 625 c 1400 appm He	
"	"	"	10	"	14	10	1.5	" "	
	"	"	70	"	5 & 20 bimodal	10	3.8	" "	

Table 3.6. Void Parameters in Ion-Irradiated P7 Alloy (Continued)

Ion Species	Ion Energy (MeV)	Peak Dose Rate (x 10^{-3} dpa/s)	Dose (dpa)	Irr. Temp. (°C)	Mean Diameter (nm)	Density (x 10^{15} cm^{-3})	Swelling (%)	Comments	Ref.
Ni	4.0	6.1	1	625	3	60	0.05	preinject rt-20 appm He 200 appm D	38
"	"	"	10	"	4	100	0.2	" "	
"	"	"	66	"	4 & 6	4 & 60	1.0	" "	
Ni	4.0	6	1	567	9	0.7	---	single ion	39
"	"	"	70	"	50	1	10	" "	
"	"	"	1	627	12	2	---	" "	
"	"	"	70	"	95	0.4	18	" "	
"	"	"	1	677	24	0.01	---	" "	
"	"	"	70	"	200	0.05	22	" "	
"	"	"	1	752	None	---	---	" "	
"	"	"	70	"	260	0.003	2.5	" "	
"	"	"	1	827	None	---	---	" "	
"	"	"	70	"	100	Few	---	" "	
"	"	"	1	567	4	1.4	---	dual ion, 28 appm He/dpa	
"	"	"	70	"	30	3.0	5	" "	
"	"	"	1	627	9	2.3	---	" "	
"	"	"	70	"	40	1.8	11	" "	
"	"	"	1	677	20	0.8	---	" "	
"	"	"	85	"	80	0.4	19	" "	
"	"	"	1	752	11	0.16	---	" "	
"	"	"	70	"	150	0.08	14	" "	
"	"	"	1	827	5	---	---	" "	
"	"	"	70	"	90-170	0.004-0.04	2-10	" "	

Table 3.6. Void Parameters in Ion-Irradiated P7 Alloy (Continued)

Ion Species	Ion Energy (MeV)	Peak Dose Rate (x 10^{-3} dpa/s)	Dose (dpa)	Irr. Temp. (°C)	Mean Diameter (nm)	Density (x 10^{15} cm^{-3})	Swelling (%)	Comments	Ref.
Ni	4.0	6	1	567	10	1.5	---	triple ion 28 appm He/dpa 50 appm D/dpa	39
"	"	"	70	"	30	10	---	" "	
"	"	"	1	627	10	0.3	---	" "	
"	"	"	70	"	30	3	13	" "	
"	"	"	1	677	---	None	---	" "	
"	"	"	70	"	100-220	0.01-0.4	15-20	" "	
"	"	"	1	752	25	0.08	---	" "	
"	"	"	70	"	250	0.01	12	" "	
"	"	"	1	827	15	0.02	---	" "	
"	"	"	70	"	150	0.08	---	" "	
Ni	4.0	2	10	667	55	0.25	1.8	single ion no pulse	40
"	"	"	"	"	50	4	2.8	single ion 0.05 s on/off	
"	"	"	"	"	65	1.4	2.4	single ion 60 s on/off	
"	"	"	"	"	35	15	3.7	dual ion 20 appm He/dpa no pulse	
"	"	"	"	"	55	4	3.3	dual ion 0.5 s on/off	
"	"	"	"	"	44	6	2.6	dual ion 60 s on/off	

Table 3.6. Void Parameters in Ion-Irradiated P7 Alloy (Continued)

Ion Species	Ion Energy (MeV)	Peak Dose Rate (x 10^{-3} dpa/s)	Dose (dpa)	Irr. Temp. (°C)	Mean Diameter (nm)	Density (x 10^{15} cm^{-3})	Swelling (%)	Comments	Ref.
Ni	4.0	2	10	667	19	8-19	0.3-1	preimplant 200 appm He no pulse	40
"	"	"	"	"	21	2	0.14	preimplant 0.5 s on/off	
"	"	"	"	"	13-16	0.7-2	0.06-0.09	preimplant 60 s on/off	
"	"	"	"	660	55	0.25	1.8	single ion no pulse	41
"	"	"	"	"	50	0.4	2.8	single ion 60 s on/off	
"	"	"	"	"	65	0.14	2.4	single ion 0.5 s on/off	
"	"	"	"	750	84	0.02	0.45	single ion no pulse	
"	"	"	"	"	None	---	---	no voids w/pulse	
"	"	"	"	660	19	0.8	0.3	preinject 200 appm He	
"	"	"	"	"	21	0.2	0.14	preinject 60 s on/off	
"	"	"	"	"	16	0.07	0.06	preinject 0.05 s on/off	
"	"	"	"	750	18	0.15	0.05	preinject no pulse	
"	"	"	"	"	5.6	3.9	0.04	preinject 60 s on/off	

Table 3.6. Void Parameters in Ion-Irradiated P7 Alloy (Continued)

Ion Species	Ion Energy (MeV)	Peak Dose Rate (x 10^{-3} dpa/s)	Dose (dpa)	Irr. Temp. (°C)	Mean Diameter (nm)	Density (x 10^{15} cm^{-3})	Swelling (%)	Comments	Ref.
Ni	4.0	2	10	750	6.3	5.0	0.06	preinject 0.5 s on/off	41
"	"	"	"	570	17	2.5	0.59	dual ion 20appm He/dpa no pulse	
"	"	"	"	"	19	3.3	1.2	dual ion slow pulse	
"	"	"	"	"	19	3.0	1.3	dual ion fast pulse	
"	"	"	"	660	35	1.5	3.7	dual ion 20 appm He no pulse	
"	"	"	"	"	55	0.4	3.3	dual ion slow pulse	
"	"	"	"	"	44	0.6	2.6	dual ion fast pulse	
"	"	"	"	750	39	0.12	0.48	dual ion 20 appm He/dpa no pulse	
"	"	"	"	"	15	0.61	0.10	dual ion slow pulse	
"	"	"	"	"	20	0.2	0.07	dual ion fast pulse	
Ni	4.0	2	1	567	10	0.7	0.3	single ion	42
"	"	"	"	627	11	2	0.15	" "	
"	"	"	"	677	25	0.003	---	" "	

Table 3.6. Void Parameters in Ion-Irradiated P7 Alloy (Continued)

Ion Species	Ion Energy (MeV)	Peak Dose Rate (x 10^{-3} dpa/s)	Dose (dpa)	Irr. Temp. (°C)	Mean Diameter (nm)	Density (x 10^{15} cm^{-3})	Swelling (%)	Comments	Ref.
Ni	4.0	2	10	567	26	0.7	1	single ion	42
"	"	"	"	627	35	1.0	2.5	" "	
	"	"	"	677	90	0.02	8	" "	
"	"	"	"	750	110	Few	---	" "	
"	"	"	"	827	None	---	---	" "	
"	"	"	70	567	52	1.2	10	" "	
"	"	"	"	627	90	0.4	18	" "	
"	"	"	"	677	200	0.04	22	" "	
"	"	"	"	750	250	Few	3	" "	
"	"	"	"	827	None	---	---	" "	
Ni	4.0	7	11	572	30.9	0.66	1.1	single ion	44
"	"	"	11.3	627	38.2	0.90	2.7	" "	
"	"	"	10.5	677	99.2	0.018	0.93	" "	
"	"	"	12	752	118	0.0016	0.14	" "	
"	"	"	13	827	0	0	0	" "	
"	"	"	10	572	20.3	0.72	0.31	dual ion 20 appm He/dpa	
"	"	"	10.1	627	25.6	2.55	2.3	" "	
"	"	"	12.3	682	71.6	0.17	3.5	" "	
"	"	"	9.5	752	94.4	0.045	2.0	" "	
"	"	"	11.5	827	0	0	0	" "	

systematic effects. The highest levels of swelling were exhibited by the unimplanted reference P7.(39)

P7 has also been studied after pulse (0.5 s on/off and 60 s on/off) irradiation. The effect of pulse irradiation on the swelling of P7 are complex.(40,41) One clear effect of pulsing is to suppress nearly all large void type cavities while not greatly influencing the small bubble type cavities at high temperatures.

In a direct comparison of neutron and ion-irradiated P7 to a nominal dose of 10 dpa, Farrell and Packan(44) found that the level of peak swelling of the ion-irradiated P7 (2.4%, T = 627°C) was 1/3 that of neutron-irradiated P7 (7.7%, T = 552°C). The addition of helium (dual-beam 20 appm/dpa) slightly increased the swelling to 2.8% (T = 682°C). Results of their study show that application of an empirical temperature shift to the ion-irradiation study do not adequately reproduce the quantitative microstructural aspects of the fast neutron study. However, it will be shown (Chapter 6) that the post-transient rate of swelling (%/dpa) of ion-irradiated P7 may approach that observed during fast neutron irradiations.

References for Chapter 3

1. D.R. Harries, Physical Metallurgy of Iron-Chrome-Nickel Austenitic Stainless Steels, Intern. Conf. Mech. Behavior and Nucl. Appl. of Stainless Steels at Elevated Temps., Varese, May 1981, London, Metals Society.

2. F.B. Pickering, Intern. Met. Reviews 1 (1976) 227-68.

3. C.J. Novak, in Handbook of Stainless Steels, D. Peckner and I.M. Bernstein (Eds.), (1978), pp. 4.1-4.77.

4. B. Weiss and R. Stickler, Met. Trans. 3 (1972) 851.

5. A.J. Bolton et al., CEGB Report No. RD/B/N3991 (1977).

6. A.J. Bolton et al., Properties and Microstructure of 316 Stainless Steel, Vol. 2, (1979), pp. 183-190, Cambridge, ICM3.

7. J.M. Leitnaker and J. Bently, Met. Trans. 84A (1977) 1605.

8. L.P. Stoter, J. Mater. Sci. 16 (1981) 1039-51.

9. C. Da Cassa and V.B. Nilishwar, J. Iron Steel Inst. 207, (1969) 1003.

10. J. Gwyther, M. Hobdell and A.J. Hooper, Metals Tech., (1974) 406-411.

11. T. Thorvaldson and G.L. Dunlop, Met. Sci. 16 (1982) 184-190.

12. J.M. Silcock, Corrosion, NACE 38, No. 2, (1982) 122.

13. P. Marshall, "Austenitic Stainless Steels - Microstructure and Mechanical Properties," Elsevier Applied Science Publishers, 1984.

14. E.H. Lee, P.J. Maziasz and A.F. Rowcliffe, in "Phase Stability During Irradiation," TMS-AIME, (1980), pp. 191-218.

15. H. Goldschmidt, "The Phase Constituents of Some Niobium Bearing and Associated Transition Metal Systems," Interstitial Alloys, New York, Plenum Press (1967).

16. P.J. Maziasz, in "The Metal Science of Stainless Steels," E.W. Collings and H.W. King (Eds.), TMS-AIME, (1979), p. 160.

17. J.K.L. Lai et al., Mater. Sci. and Engr. 49 (1981) 19; also J.K.L. Lai, Mater. Sci. and Engr. 58 (1983) 195.

18. E.O. Hall and S.H. Algie, Met. Rev. 11 (1966) 61-88.

19. P. Duhaj, J. Ivan and E. Makovicky, J. Iron Steel Inst. 206 (1968) 1245.

20. P.A. Blenkinsop and J. Nutting, J. Iron Steel Inst. 205 (1967) 953.

21. J.E. Spruiell et al., Met. Trans. 4 (1973) 1533.

22. A.S. Grot and J.E. Spruiell, Met. Trans. 6A (1975) 2023.

23. W.G. Johnston, J.H. Rosolowski and A.M. Turkalo, J. Nucl. Mater. 46 (1973) 273-280.

24. F.A. Garner, J. Nucl. Mater. 117 (1982) 177.

25. G.L. Kulcinski, J.J. Laidler and D.G. Doran, Rad. Effects 7 (1971) 195.

26. J.A. Hudson, J. Nucl. Mater. 60 (1976) 89.

27. W.G. Johnston et al., ASTM STP 529 (1973) 213.

28. N.H. Packan and K. Farrell, ASTM STP 782 (1982) 885.

29. S. Wood et al., ASTM STP 725 (1981) 455.

30. G. Ayrault et al., J. Nucl. Mater. 103 & 104 (1981) 1035.

31. E.H. Lee, A.F. Rowcliffe and E.A. Kenik, J. Nucl. Mater. 83 (1979) 79-89.

32. M.J. Makin et al., in Radiation Effects in Breeder Reactor Structural Materials, M.L. Bleiberg and J.W. Bennet (Eds.), TMS-AIME (1977) 645.

33. R.S. Nelson et al., in Radiation-Induced Voids in Metals, J.W. Corbett and L.C. Ianniello (Eds.) (1972) 430.

34. E.H. Lee, L.K. Mansur and A.F. Rowcliffe, J. Nucl. Mater. 122 & 123 (1984) 299.

35. W.J.S. Yang et al., in Phase Stability During Irradiation, J.R. Holland, L.K. Mansur and D.I. Potter (Eds.), TMS-AIME (1980) 257.

36. P.J. Maziasz, J. Nucl. Mater. 122 & 123 (1984) 472.

37. E.E. Bloom, J.O. Stiegler, A.F. Rowcliffe and J.M. Leitnaker, Scripta Met. 10 (1976) 303.

38. K. Farrell and N.H. Packan, J. Nucl. Mater. 85 & 86 (1979) 683-687.

39. N.H. Packan and K. Farrell, J. Nucl. Mater. 85 & 86 (1979) 677-681.

40. N.H. Packan, J. Nucl. Mater. 114 (1981).

41. K. Miyahara, N.H. Packan and N. Igata, Effect of Radiation on Materials: Eleventh Conf., ASTM STP 782, H.R. Brager and J.S. Perrin (Eds.), (1982) 941-952.

42. N.H. Packan and K. Farrell, Nucl. Tech. Fusion 3 (May 1983) 392-404.

43. H.R. Brager and F.A. Garner, in Ref. 41, 152-165.

44. K. Farrell and N.H. Packan, in Ref. 41, 953-962.

CHAPTER 4. EXPERIMENTAL APPARATUS AND PROCEDURE

A. Specimen Composition and Characterization

The 316 stainless steel used in this study was manufactured by MSI Nuclear of Salt Lake City, Utah. The material heat number is X15893 which is the Magnetic Fusion Engineering reference heat. The chemical composition (mill and check) as determined by MSI Nuclear is given in Table 4.1. The material was further analyzed by National Spectrographic Laboratories, Inc. of Cleveland, Ohio. Their chemical analysis gave the composition in Table 4.2.

The material was thermal-mechanically treated from a 5/16" hot-rolled plate to a final 0.020" thickness by T.K. Roche of the Metals Processing Group, Metals & Ceramics Division, Oak Ridge National Laboratory. A detailed account of this treatment by Roche is given in Fig. 4.1. Figures 4.2 and 4.3 are optical and TEM micrographs which illustrate the 60 μm average grain size and low (10^9 cm^{-2}) initial dislocation density representative of the pre-irradiation material.

The P7 alloy used in this study was developed and manufactured at ORNL as a high purity austenitic stainless steel. The composition of P7 (see Table 4.3) contains major alloying elements in quantities similar to the AISI specification for 316 SS.

Initial attempts to determine the oxygen content of both alloys by use of Auger Electron Spectroscopy was unsuccessful. No oxygen signal could be detected in either alloy after the initial oxide

Table 4.1. MSI Nuclear Analysis of 316 SS (wt.%)

	Cr	Ni	Mo	Mn	Si	C	P	S	Fe
Mill	17.33	12.38	2.14	1.79	0.65	0.05	0.031	0.020	Bal.
Check	17.53	12.81	2.21	1.83	0.64	0.05	0.028	0.021	Bal.

Table 4.2. NATIONAL SPECTROGRAPHIC Analysis of 316 SS (wt.%)

Cr	Ni	Mo	Mn	Si	C	P	S	Fe
16.56	11.84	2.44	1.67	0.66	0.057	0.033	0.015	Bal.

Table 4.3. ORNL Analysis of P7 Alloy (wt.%)

Cr	Ni	Mo	Mn	Si	C	P	S	Ti	W	Fe
17	16.7	2.5	0.03	0.1	0.005	---	---	0.01	0.068	Bal.

Log No.: 9874 Date: 8/21/81

Materials Processing Laboratories

REQUEST FOR SERVICE

Material and Prior History: 316 SS Ht X-15893, 5/16" thick hot-rolled plate. Process to 0.020" thick sheet annealed condition.

Work Description Schedule:
- Anneal 1 hr @ 1050°C in Argon
- Cold roll to 0.150 (Bliss Mill)
- Anneal 1 hr @ 1050°C in Argon (Sargeant and Wilbur Fu.)
- Cold roll to 0.075 (Bliss Mill)
- Anneal 1 hr @ 1050°C in Argon (Sargeant and Wilbur Fu.)
- Cold roll to 0.040 (Bliss Mill)

Remarks (For Lab. Use)
- Anneal 1 hr @ 1050°C in Argon (Sargeant and Wilbur Fu.)
- Cold roll to 0.020 (Bliss Mill)
- Anneal 1 hr @ 1050°C in Argon (Ceramic Devel. Lab. Fu., Run #215)

Material pickled lightly in HF-HNO_3-H_2O after each annealing step, and degreased after each cold rolling step.

Signature: T.K. Roche

Extension: 4-4357

Fig. 4.1. Thermal-mechanical treatment of hot-rolled 316 SS plate to yield a 0.51 mm (0.020") thick solution-annealed foil.

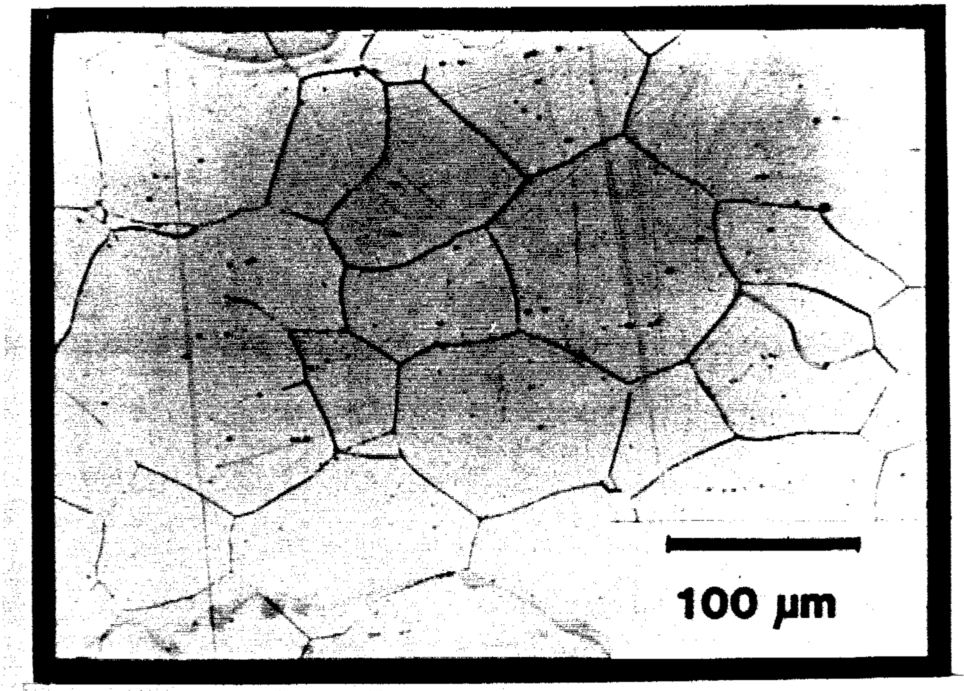

Fig. 4.2. Optical micrograph showing the grain size and grain structure of as-received solution-annealed 316 SS.

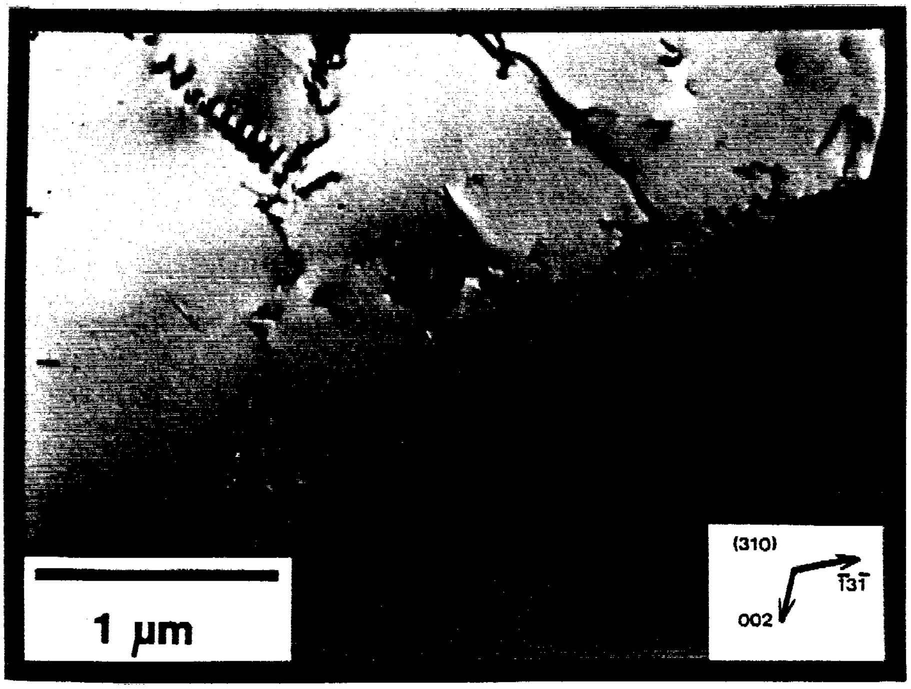

Fig. 4.3. TEM micrograph of annealed 316 SS illustrating the dislocation structure.

Table 4.4. Oxygen and Nitrogen Content by Inert Gas Fusion Analysis

	Oxygen (wt.%)	Nitrogen (wt.%)
316 SS	0.005	0.046
P7	0.028	0.0041

layer was sputtered away (see Figs. 4.4, 4.5). Inert gas fusion analysis of samples of these alloys performed at Teledyne Wah Chang Laboratories yielded oxygen and nitrogen contents given in Table 4.4.

B. Heavy-Ion Irradiation Facility

Irradiations of the 316 stainless steel and P7 alloy were conducted at the U.W. Heavy-Ion Irradiation Facility. The facility has been used by numerous student researchers in the U.W. Radiation Damage Research Group and has been upgraded and modified during its period of use. The basic system is described in detail elsewhere.(1,2) The present constituents of the facility include a heavy-ion source with the acronym of SNICS, a 7 MV tandem electrostatic accelerator, various beam handling/monitoring equipment, and a target stand (see Fig. 4.6).

The ion species to be used in this study are Ni^{3+}. These ions originate as Ni^- from the SNICS source which was conceived and developed by Caskey et al.(3) To create this ion species, a cathode of nickel is sputtered away by energetic cesium ions. The ions created are Ni^- which are electrostatically extracted from the source at

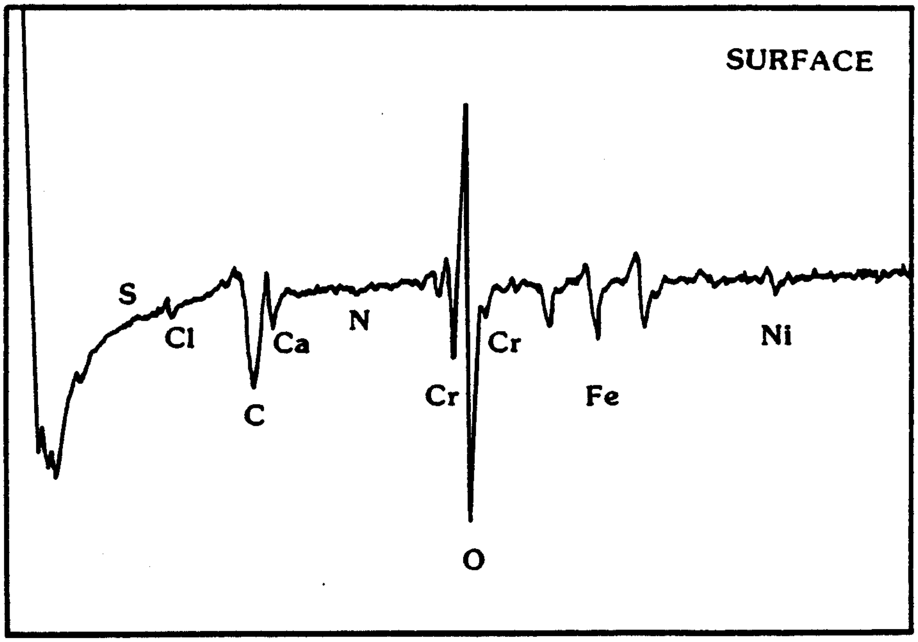

Fig. 4.4. Auger electron signal at surface of a P7 foil. Note strong oxygen signal as a result of the surface oxide.

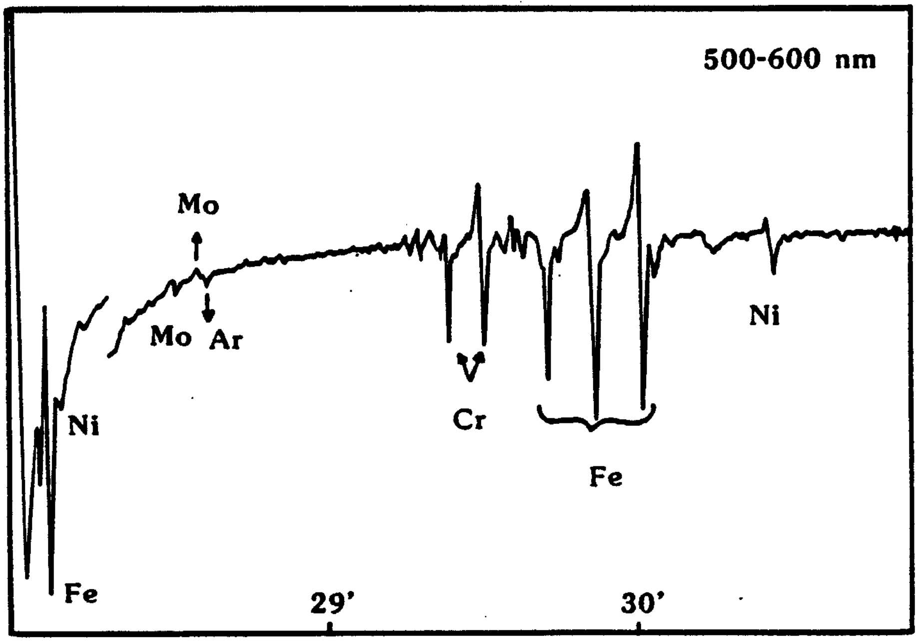

Fig. 4.5. Auger electron signal after 500-600 nm of material was sputtered away (30 minutes of sputtering).

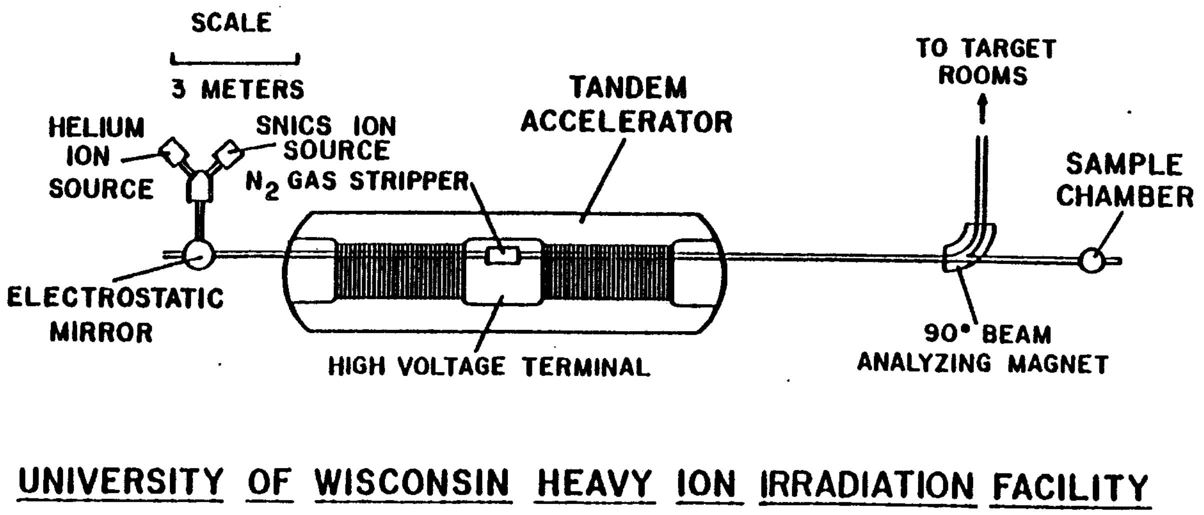

Fig. 4.6. Basic components of the UW Heavy Ion Irradiation Facility include the SNICS ion source, the tandem accelerator, and the sample chamber (target section).

a potential of 2-4 kV. The ions are then magnetically analyzed and then deflected by an electrostatic mirror into the low energy end of the accelerator (built by High Voltage Engineering Corporation, Model EN). From here, the negative ions are accelerated towards the high voltage terminal with positive voltage V. A N_2 gas stripper is used to strip electrons from the negative ions via a collision process, leaving them as positive ions. With varying degrees of stripping, a distribution of charge states of the ions are created with charge nq, n being an integer. These positive ions are further accelerated through the potential V and exit of the high energy end of the machine. Therefore, given a charge state n, and with the terminal potential V, the emergent ion would have acquired the energy

$$E = qV(1 + n) \ . \tag{4.1}$$

A given charge state is selected by use of an electromagnetic quadrupole lens mounted on the high energy beam tube. For .this study, a charge state of $n = 3$ was selected in conjunction with a terminal potential of 3.5 MV to give 14 MeV heavy ions to irradiate the specimen.

The 14 MeV Ni^{3+} ions are then directed towards the target stand of the Heavy-Ion Irradiation Facility. This target stand and its vacuum system were originally designed and built by H.V. Smith and R.G. Lott.(1,2) The present configuration is shown in Fig. 4.7. This section lies ~ 1/2° off the tandem axis to prevent any contami-

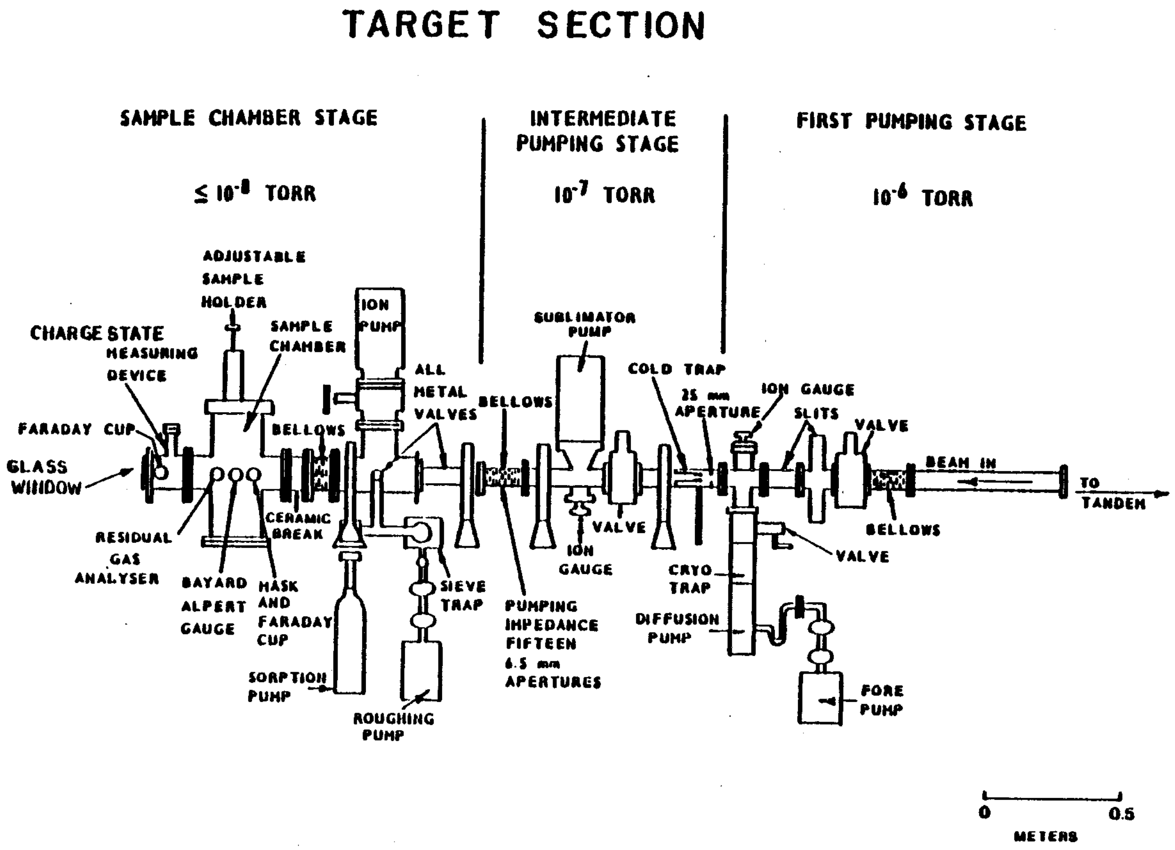

Fig. 4.7. U.W. Radiation Damage Group target stand for heavy-ion irradiation.

nant particles such as high energy neutrals or low Z ions from impinging upon the target. A large analyzing magnet is used to correctly steer the beam of heavy ions toward this target section.

The vacuum system for this section consists of three pumps in series. The first stage employs a 2" water-cooled diffusion pump with a speed of 200 ℓ/s. Pressures at this point in the system are about 10^{-4} Pa (~ 10^{-6} torr). The second stage consists of a 400 ℓ/s titanium sublimator pump built by National Electrostatics Inc. of Middleton, Wisconsin. Pressures obtained are 10^{-5} Pa (~ 10^{-7} torr) at this point as measured by an ion gauge. Finally, pressures in the third stage are kept around 10^{-6} Pa (~ 10^{-8} torr) by use of a large orbitron pump. These pressures are maintained even at elevated (500-700°C) temperatures.

A Varian Model VGA-100 residual gas analyzer is used to monitor the gases present in this final vacuum system stage which houses a carrousel specimen holder/heater.(4) Up to eight specimens can be mounted in the holder with the irradiated sample individually radiatively heated. Individual chromel-alumel thermocouple leads allow the temperature of the eight hold specimens to be monitored during an irradiation.

To characterize and measure the intensity of the beam in the target section, several diagnostic devices are used. The charge state distribution of the ion species striking the specimen are analyzed by allowing the beam to strike an inserted gold foil where Rutherford scattering events occur. Particles scattered 90° from the foil are detected by a solid state detector. An energy spectrum can be ascertained from the scattering information. With proper beam focusing and steering, it is possible to obtain a beam which contains over 95% 14 MeV Ni^{3+} ions. To measure total beam current, three different Faraday cups, one at the entrance to the target section, one directly before the specimen, and one directly behind the specimen are used. The cups are labeled the entrance cup, the mask cup, and the exit cup, respectively. When the mask cup is not used to check the beam current, a Ta mask containing a 3 mm aperture is inserted to define the irradiation spot on the specimen. Spurious specimen currents were noted using the carrousel holder/heater and recent modifications to correct this were made. These changes included the use of a ceramic break to allow the specimen stage to float electrically and suppress the emission of secondary electrons.

C. Specimen Preparation and Analysis

The samples of this study were analyzed using the cross-section technique(4,5) as outlined in Fig. 4.8. The cross-section procedure allows the entire ion damage region to be viewed at once, thereby allowing analysis in regions that have been subjected to varying dose and dose rate levels as well as control regions which did not undergo displacement damage.

Spurling and Rhodes(6) were the first researchers to apply the cross-section method to an ion-irradiated material. Unfortunately, their technique required a high temperature (500°C) anneal in order to ensure an adequate bond at the foil-plate interface. The cross-

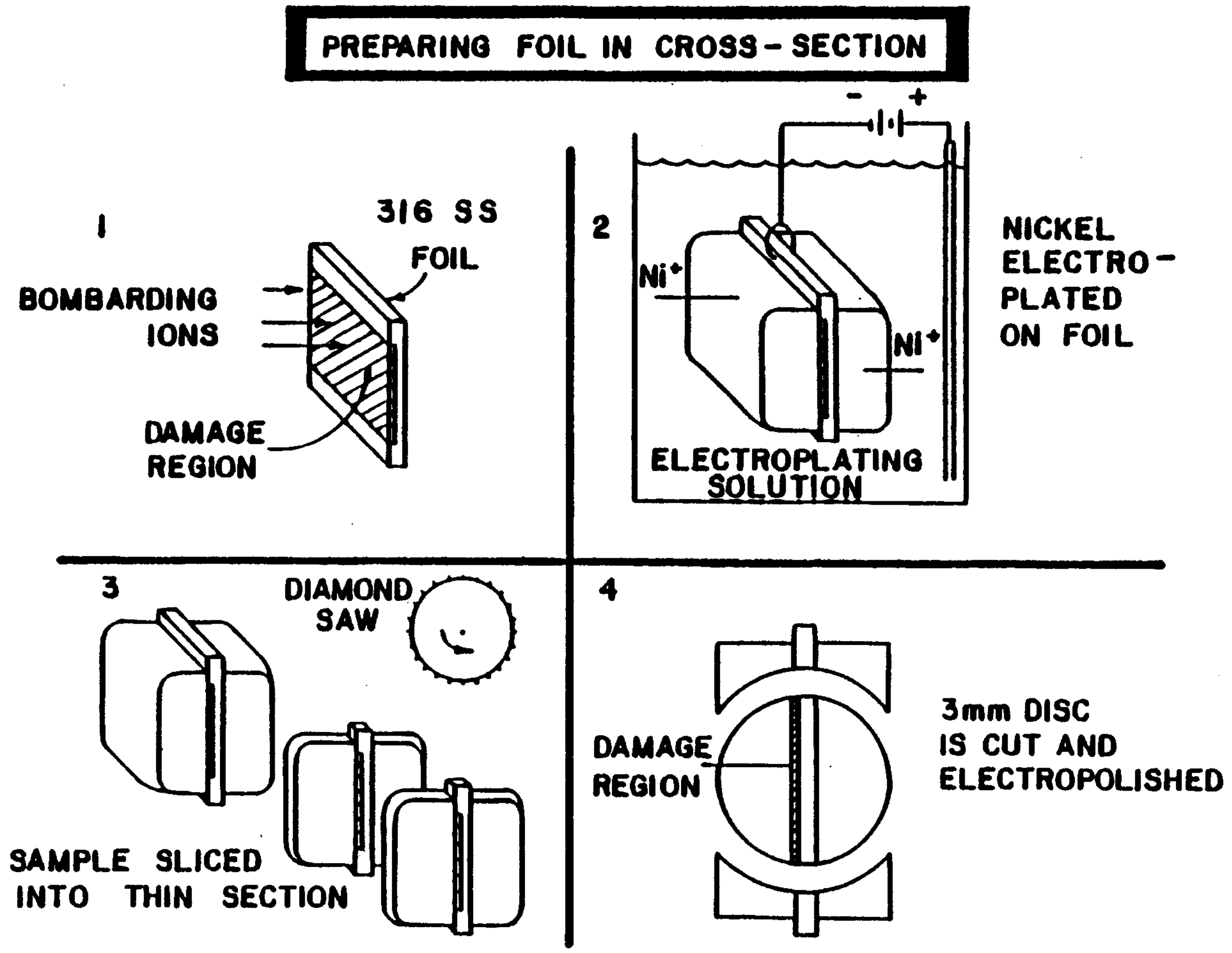

Fig. 4.8. Steps in the preparation of a TEM specimen to show entire damage region in an irradiated foil.

section procedure developed in this study is free from any post-irradiation treatment that could alter the microchemistry to any observable degree. Details of the pre- and post-irradiation specimen preparation to produce a cross-sectioned specimen are given below.

C.1. Pre-Irradiation Specimen Preparation

Foils approximately 1 cm × 0.5 cm were cut from the 0.020" (0.51 mm) stock and mechanically polished using a fine 0.3 μm alumina powder abrasive. The samples were not electropolished prior to irradiation in order to preclude the introduction of reactive gases into the specimen, which have been shown to enhance cavity formation in previous heavy-ion-irradiation cross-section studies of nickel.(5,7)

C.2. Post-Irradiation Specimen Preparation

Following irradiation, the 1 cm × 0.5 cm foil is thoroughly degreased using acetone. Next, both sides of the foil are lightly swabbed with 0.3 μm alumina followed by a thorough rinse with methanol. The edges around the foils are subsequently coated with microstop(8) lacquer (see Fig. 4.9). Next, the foil is mounted in a plexiglas holder containing a 1/2 cm × 1/2 cm "window" (see Fig. 4.10). The above two steps promote a uniform potential across the foil surface and thereby allow a uniform deposition of plating to occur.

Before the electrodeposition of a nickel plate layer on the foil, the irradiated foils are given an activation treatment in a solution of 60 g $NiCl_2 \cdot 4\ H_2O$, 40 ml HCL, and 250 ml H_2O at room

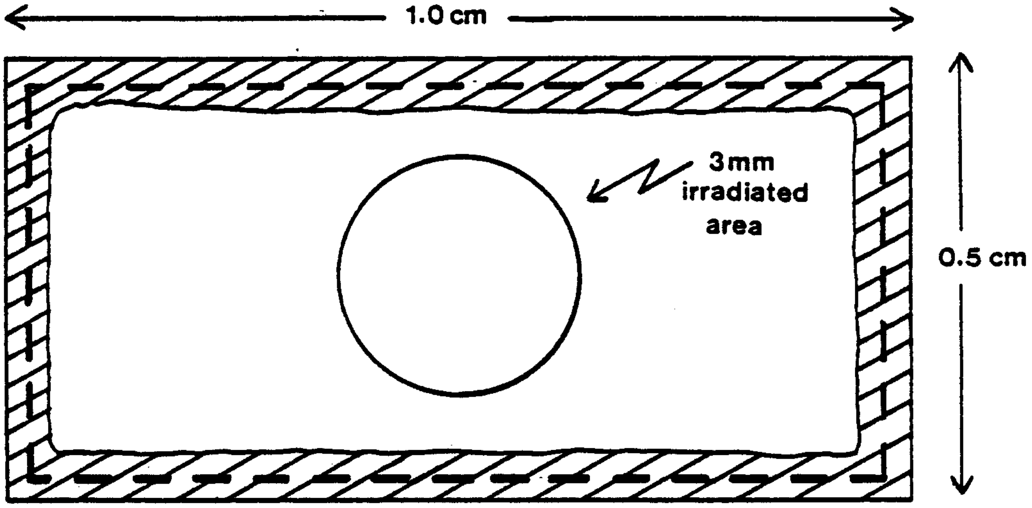

Fig. 4.9. Schematic of an irradiated 316 SS foil lacquered around its edges to decrease the convergence of electric field lines during the plating step.

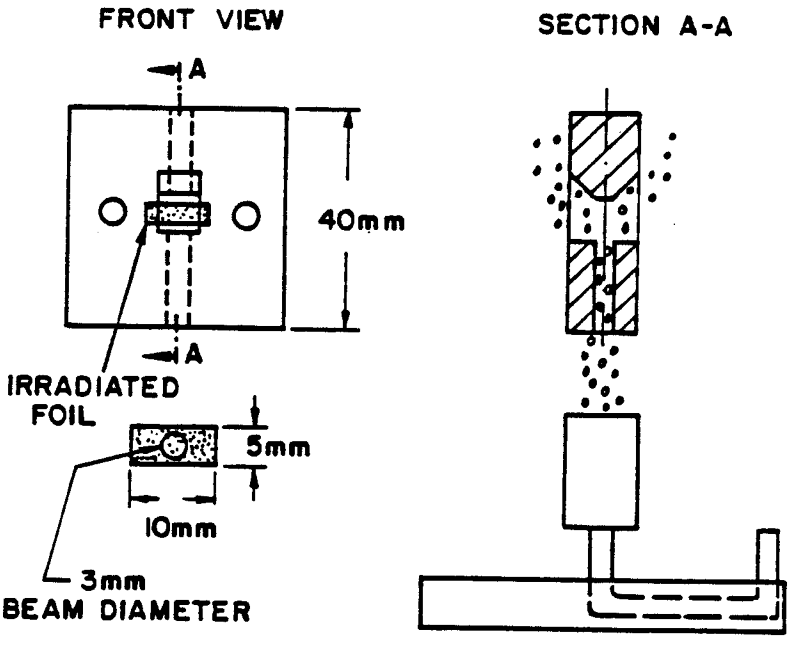

Fig. 4.10. Schematic of the sample holder and gas bubbler used for the electrodeposition of nickel.

temperature (which is similar to Wood's nickel(9)). The samples are made anodic for 2-3 seconds at a current density of 250 mA/cm^2. The purpose of this step is to remove the metal oxide layer, which is necessary in order to obtain a strong plate-foil bond. Less than 0.15 μm of material is removed from the irradiated surface as determined by interference microscopy. After activation, the polarity of the cell is reversed and the sample is plated in the above solution for 5 minutes at a current density of 100 mA/cm^2. The sample is then transferred into the nickel plate bath which is a high chlorine solution containing 150 g $NiSO_4 \cdot 4\ H_2O$, 150 g $NiCl_2 \cdot 4\ H_2O$, and 70 g boric acid in 1000 ml H_2O at 70°C. The partially plated foil is made anodic in this plate bath at 200 mA/cm^2 for 10 seconds, then with the polarity reversed, it is plated for ~ 15 hours. During the plating period, a fine stream of Ar bubbles provided by a common aquarium air stone (see Fig. 4.10) is used to create a turbulent layer near the foil surface to remove gas bubbles and help promote a more uniform electrodeposit.

A diamond saw is used to slice specimens from the plated sample. With the use of a 150 μm-thick blade, approximately five irradiated cross-section slices 0.25 mm (0.008-0.010") thick are obtained from a single irradiated sample. The 3 mm TEM discs are cut from these slices using a rotary saw.(10)

C.3. Jet-Electropolish of Cross-Sectioned Specimens

A two-step polishing technique employing two different electropolishing solutions is used to prepare a TEM specimen with an electron transparent area at the irradiated interface. In the first step, microstop lacquer(8) is applied over one side of the 3 mm disc exposing a ~ 50 μm wide strip along the irradiated interface only. The specimen is then jet-electropolished for 2 minutes in a solution consisting of 30% HNO_3 in 70% methanol at 0°C at 10 V (80-90 mA). The lacquer is removed with acetone and the specimen is jet-electropolished until perforation in a solution of 10% perchloric acid, 90% acetic acid, 20 g/ℓ Cr_2O_3 and 10 g/ℓ $NiCl_2 \cdot 4\ H_2O$ at 20°C at 45 V (80-90 mA).

C.4. Extraction Replica Procedure

For accurate chemical analysis of precipitates formed in the 316 SS, it is essential that their x-ray signal be distinguished from the background matrix signal.(11) An efficient means to obtain the true precipitate composition is the extraction of the precipitates on a replica of the specimen surface. R.A. Dodd has developed a dry-stripping technique(12) which has been successfully applied to the irradiated, nickel-plated 316 SS to obtain an extraction replica of the ion-damage region. Details of the process are given below:

1. The plated specimen is lightly etched in Villela's reagent (5 ml HCl, 1 g picric acid in 100 ml methanol) following a fine mechanical polish.
2. Apply 0.5% Formvar solution to the surface to form a primary replica.
3. Etch with Villela's reagent through the Formvar (let etchent remain on Formvar layer ~ 1 minute).

4. Rinse thoroughly with methanol, allow to dry and back the Formvar with several layers of 1% Collodion in amyl acetate.
5. Apply a thin strip of cellophane to the Collodion surface by use of replicating solution. Dry strip the combined plastic replica, and dissolve the Collodion in acetone.
6. Evaporate a thin carbon layer onto the replica to provide enhanced contrast and stability in the electron beam.

C.5. 316 SS EDS Standard

Standard Transmission Electron Microscopy and Energy Dispersive X-Ray Spectroscopy were performed in this study with a JEOL TEMSCAN 200CX TEM, STEM, EDX-capable electron microscope. When operated in the STEM mode, a 20 nm electron probe may be used to generate x-ray emission from the specimen.

Current Analytical Electron Microscopy techniques have been reviewed by Zaluzec.(11) In this study, the Cliff-Lorimer method(13) was employed to obtain the chemical analysis of the matrix as well as extracted precipitates from the 316 SS. Equation (4.2) is the ratio technique equation and can be applied to an x-ray spectrum to obtain the chemical composition of the specimen if x-ray absorption can be neglected:

$$\frac{C_i}{C_j} = k_{i-j} \frac{I_i}{I_j} \tag{4.2}$$

with $C_i + C_j + C_k + \ldots = 1$

Table 4.5

k_{Fe-Ni}	k_{Fe-Cr}	k_{Fe-Si}	k_{Fe-Mo}	k_{Fe-S}	K_{Fe-P}
0.820	1.15	2.98	0.340	1.2	1.2

Proportionality constant values obtained in this study on a 316 SS specimen using the TEMSCAN 200CX in STEM, spot mode, with condenser aperture 3 and condenser setting = 2.

where: C_i = concentration of component i in wt.%

I_i = integrated x-ray peak of component i

k_{i-j} = constant which varies with operating voltage only (assuming a "thin" foil)

The values of k (Table 4.5) used in this study were obtained by using the x-ray spectra of the 316 SS as a standard of known chemical composition (Tables 4.1, 4.2) as recommended by Goldstein.(14)

C.6. Iron Plating of Ferritic Alloys

In a manner similar to the nickel plating of 300-series austenitic steels described in Section C.2, an iron plating procedure of ferritic steel alloys was also developed in this study.

After the irradiated foil is degreased and lacquered, it is pickled for 2 minutes at 50°C in 15 ml H_2SO_4 in 85 ml H_2O to which 2 g thiourea is added. Next, the foil is carefully rinsed in water and then immersed in a plate bath consisting of 200 g of $FeCl_2 \cdot 4\ H_2O$, 50 g NaCl, 50 g $CaCl_2$ in 700 ml H_2O at 90°C. The foil is made anodic for 4 seconds at 100 mA/cm^2 after which time it is plated at the same current density.

C.7. Error Analysis

Void and precipitate sizes were determined using a Zeiss particle counter and the data is reduced in a manner similar to Whitley(5) and Knoll.(4) The swelling $\Delta V/(V - \Delta V)$ and number densities were calculated from

$$\Delta V = \frac{\pi}{6} \sum_i n_i d_i^3 \qquad (4.3)$$

$$n = \frac{\sum_i n_i}{A \cdot t} \qquad (4.4)$$

where A = area of micrograph, t = sample thickness and V = original volume = A•t.

The source of largest error was in the determination of t, the sample thickness. Methods used to calculate the thickness included stereo microscopy using a known tilt angle and a parallax measured on a Hilgar Watts stereo viewer(15) and depth fringe techniques.(16) The resultant error associated with the number densities was estimated to be ~ 30%.

References for Chapter 4

1. R.G. Lott, Ph.D. Thesis, University of Wisconsin, Madison, Wisconsin, 1979.

2. W.J. Weber, Ph.D. Thesis, University of Wisconsin, Madison, Wisconsin, 1977.

3. G.T. Caskey, R.A. Douglas, H.T. Richards and H. Vernon Smith, Jr., "A Simple Negative-Ion Sputter Source," Nucl. Inst. and Meth. 157 (1978) 1-7.

4. R.W. Knoll, Ph.D. Thesis, University of Wisconsin, Madison, Wisconsin, 1981.

5. J.B Whitley, Ph.D. Thesis, University of Wisconsin, Madison, Wisconsin, 1978.

6. R.A. Spurling and C.G. Rhodes, J. Nucl. Mat. 44 (1972) 341.

7. D.B. Bullen, Ph.D. Thesis, University of Wisconsin, Madison, Wisconsin, 1984.

8. Michigan Chrome & Chemical Co., Microstop and Microshield STOP-OFF LACQUER, 8615 Grinnell Avenue, Detroit, MI, 48213.

9. T.M. Rodgers, Handbook of Practical Electroplating, MacMilland, New York (1959) 225.

10. South Bay Technology, Inc., Model 350 Abrasive Slurry Drill, 5209 Tyler Ave., Temple City, CA, 91780.

11. N.J. Zaluzec in "Introduction to Analytical Electron Microscopy," J.H. Hren, J.I. Goldstein and D.C. Joy (Eds.), Plenum Press, New York (1977) 121-167.

12. R.A. Dodd, Professor, Metallurgy and Mineralogy Engineering, University of Wisconsin, private communication.

13. G. Cliff and G.W. Lorimer, J. Microscopy 103 (1975) 203.

14. J.I. Goldstein, in Ref. 11.

15. Rank Precision Industries, Ltd., Folding Mirror Stereoscope SB/80, P.O. Box 36, Leicester House, Lee Circle, Leicester, England LE1 9JB.

16. J.W. Edington, Practical Electron Microscopy in Materials Science, (1974) Phillips, Vol. 3, p. 3.

CHAPTER 5. RESULTS

The irradiation conditions of the P7 alloy and 316 stainless steel are shown in Fig. 5.1 with the irradiation parameters given in Table 5.1. The irradiation response of both the P7 alloy and the 316 SS produced interesting temperature-dependent microstructural features. Irradiations of P7 with 14 MeV Ni-ions induced void formation over the entire temperature range (400-650°C) investigated in this study. The low temperature P7 results showed a suppression in both cavity number density and average diameter over depths which correspond to the range of the 14 MeV Ni-ion species. No such suppression effects were noted in the samples irradiated to similar fluences at 550°C and 650°C. The P7 samples irradiated at 650°C showed the evolution of a bimodal void size distribution at the damage peak. This void-size distribution has not been previously observed in helium-free irradiations of austenitic steel alloys.

Voids were detected after the ion-irradiation of 316 SS at the lowest temperature surveyed, 450°C up to 550°C. The void formation was heterogeneous with the voids forming at precipitate interfaces only. No voids were detected after 40 dpa in samples irradiated at 600 and 650°C. An Fe_2P phase was detected in these 316 SS samples. Annealing experiments in this study have shown this phase to be radiation-induced. The range of visible damage (dislocation structure) ended at depths of 2.9-3.2 μm for the entire temperature range, consistent with the calculated damage profile.

Table 5.1. 14 MeV Ni-Ion Irradiation Parameters

Material	Irradiation Temp. (°C)	Ion Fluence $\times 10^{16}$ ions/cm^2	Dose 1 μm* (dpa)	Dose Rate at 1 μm (10^{-3} dpa/s)	Dose 2.2 μm (dpa)	Dose Rate at 2.2 μm (10^{-3} dpa/s)
P7 Alloy	400	3.3	10	1.0-1.3	40	4-5
P7 Alloy	500	0.8	2.4	0.8-1.0	10	3-4
P7 Alloy	500	3.3	10	0.8-1.0	40	3-4
P7 Alloy**	550	1.0	3.0	0.9-1.2	12	3-5
P7 Alloy	650	0.8	2.4	0.8-1.0	10	3-4
P7 Alloy	650	3.3	10	1.0-1.3	40	4-5
P7 Alloy	650	5.6	17	1.6-2.0	68	6-8
P7 Alloy	650	8.3	25	0.8-1.0	100	3-4
Outgassed P7	650	1.7	5	0.8-1.0	20	3-4
Outgassed P7	650	3.3	10	0.8-1.0	40	3-4
316 SS	450	3.3	10	0.6-0.8	40	2-3
316 SS	500	3.3	10	0.8-1.0	40	3-4
316 SS	500	10	30	1.5-1.8	120	6-8
316 SS	550	3.3	10	0.7-0.9	40	3-4
316 SS	600	3.3	10	0.8-1.0	40	3-4
316 SS	650	3.3	10	1.0-1.5	40	4-6

*E_d = 40 eV, K = 0.8

**Irradiated with 14 MeV copper ions

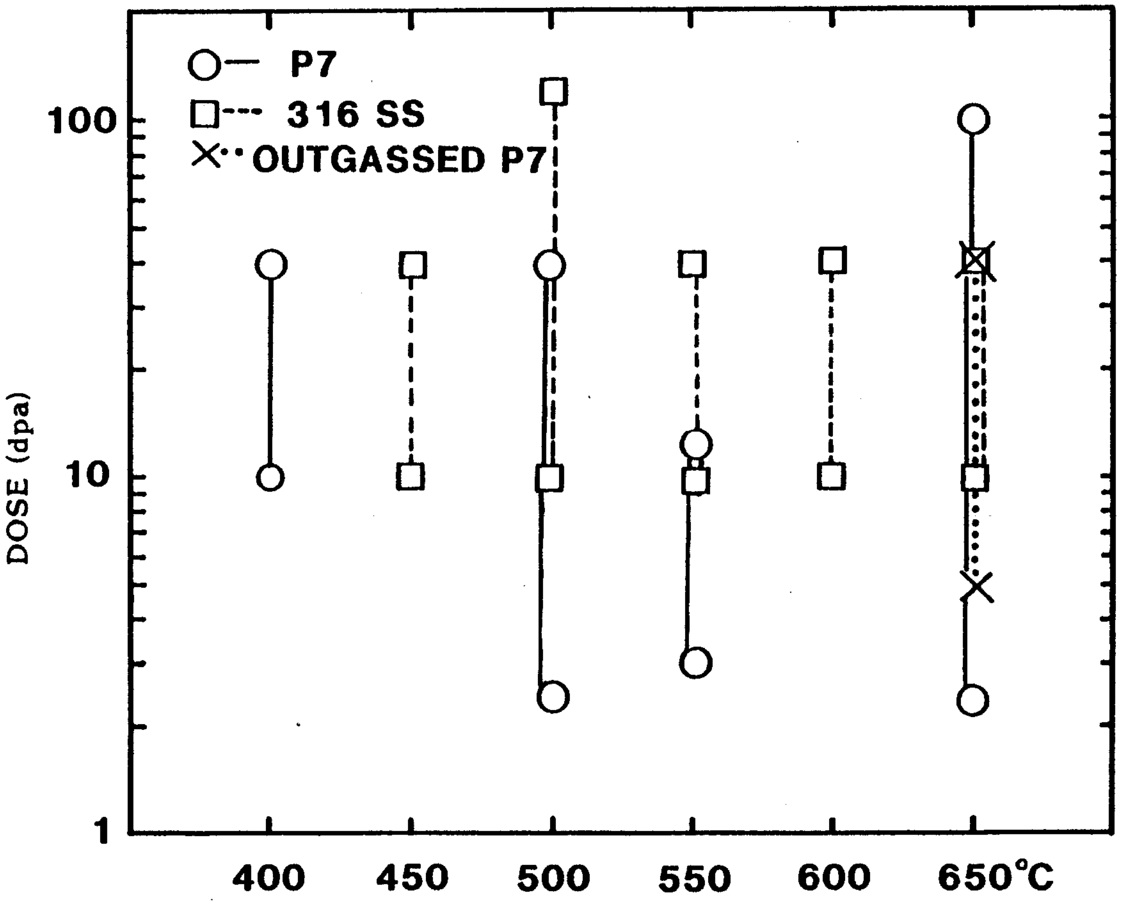

Fig. 5.1. Dose and temperature regimes investigated in this study for 14 MeV Ni-ion-irradiated P7 alloy, MFE heat of 316 SS, and outgassed P7 alloy. (Dose levels from entire ion damage range.)

A. Nickel-Ion-Irradiated P7 Alloy

TEM analysis of the 14 MeV Ni-ion irradiations of P7 over the 400-650°C temperature range with doses up to 100 dpa did not show major phase decomposition of the austenite matrix in the damage region or in the control region. Voids were observed to form during irradiation at all temperatures investigated while the average cavity diameter increased and the cavity density decreased with temperature at a give dose level. The dislocation structure contained predominantly Frank loops with b = a/3<111> at low temperatures (< 500°C) whereas a network dislocation structure was observed at 650°C with a saturated density of 1-3 x 10^{10} cm^{-2} over the dose levels surveyed in this study. The results of the observed dislocation structure are summarized in Table 5.2. Stacking fault tetrahedra were observed at the end of damage range (3 μm depth) at 400°C. Figure 5.2 shows the size (25 nm) and distribution (10^{15} cm^{-3}) of the stacking fault tetrahedra after a dose of 10 dpa.

A.1. Injected Interstitial Effects

Previous studies using the cross-section technique on nickel had reported observing varying widths of a suppression in void formation in the injected interstitial range of the irradiated samples.(1,2) In an attempt to observe this phenomenon in a different alloy system, samples of the P7 alloy were irradiated at 400°C and 500°C to peak doses of 40 dpa. Figures 5.3 and 5.4 show the TEM micrographs and void parameters obtained from the 400°C sample. Voids at the 1 μm depth (10 dpa) are larger in diameter (4.5 nm) than those near the

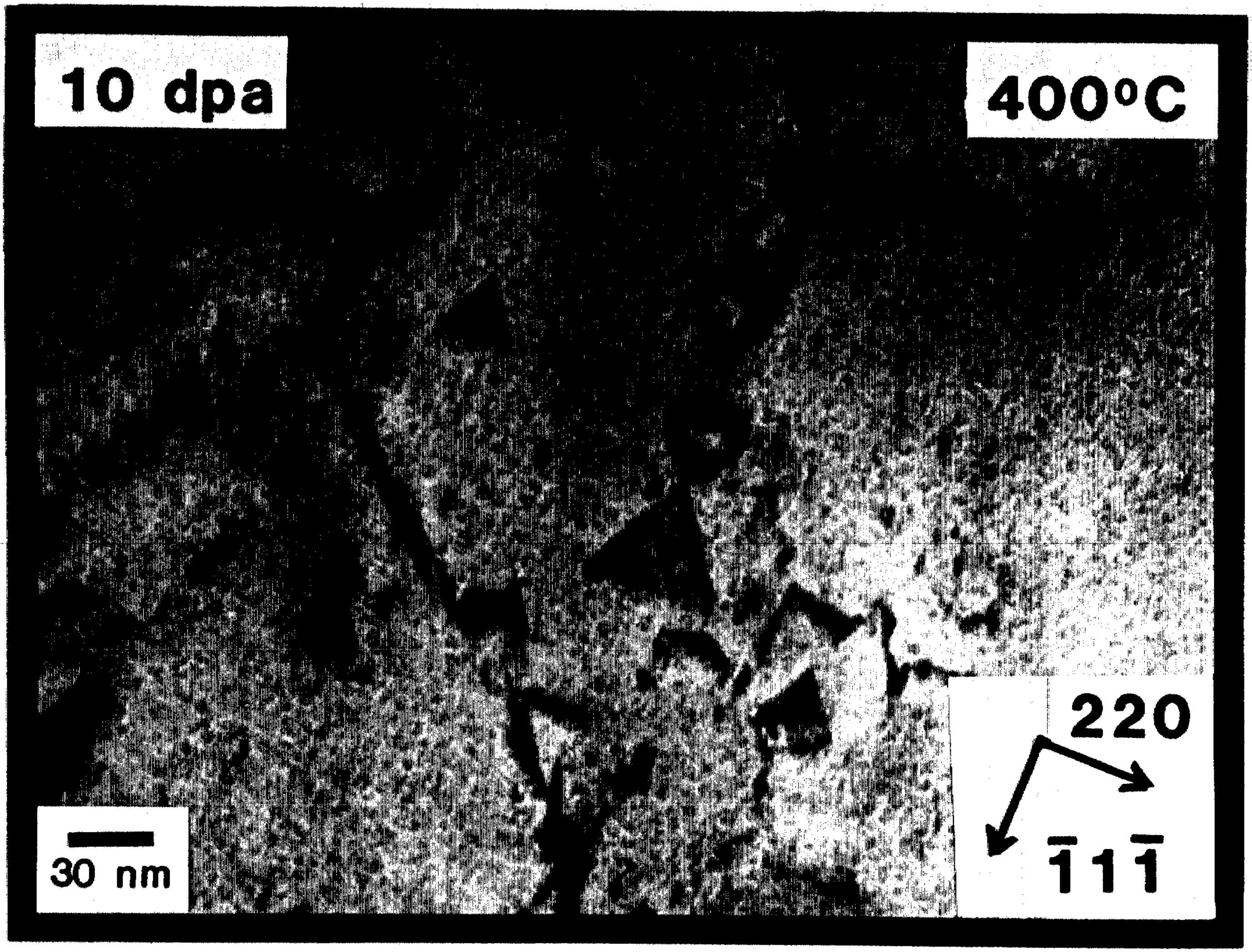

Fig. 5.2 Stacking fault tetrahedra observed near the end of the damage range in the P7 alloy.

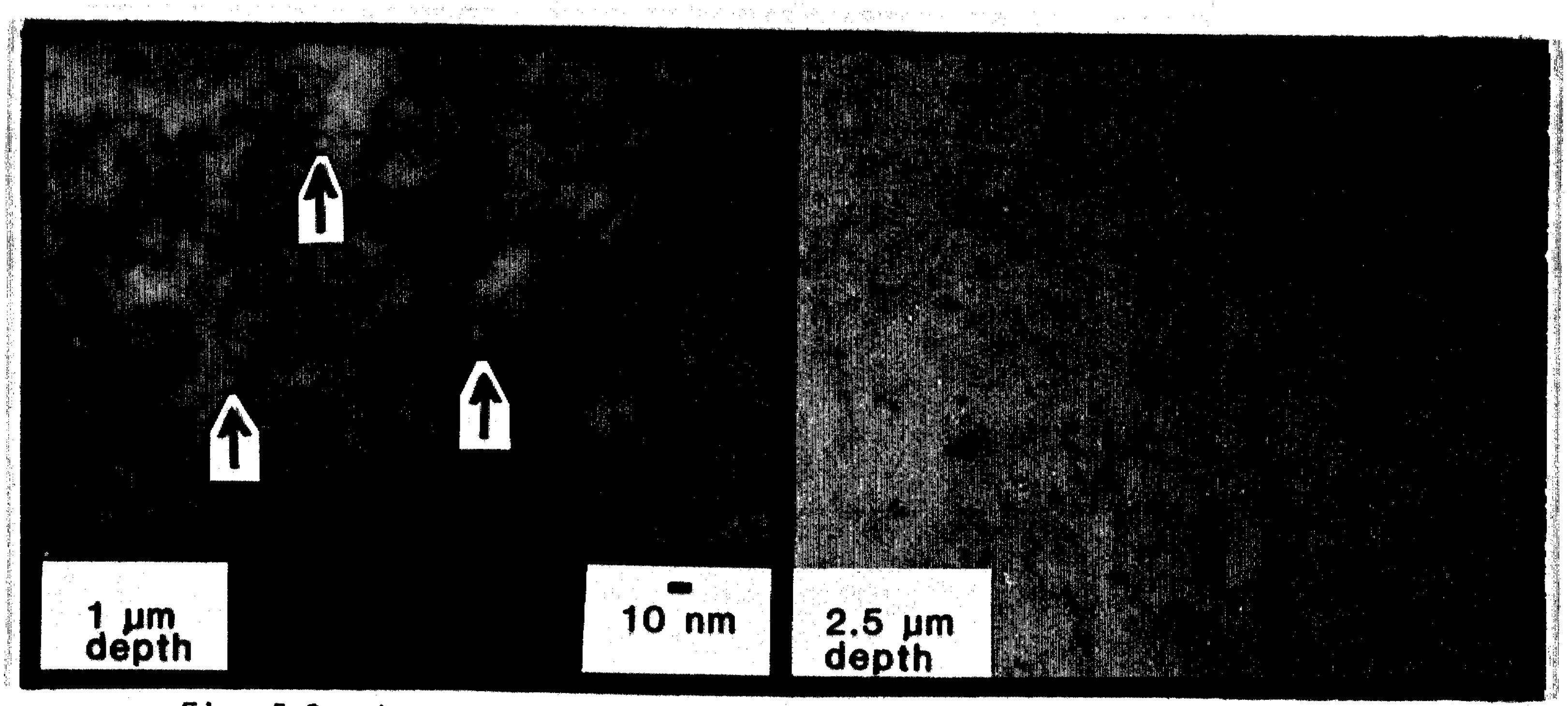

Fig. 5.3. Low contrast TEM micrographs at a depth of 1 µm and 2.5 µm in the 400°C P7 sample irradiated to 10 dpa at 1 µm. Note the dramatic suppression of void growth (size) at the 2.5 µm depth which is near the peak of the injected nickel ions.

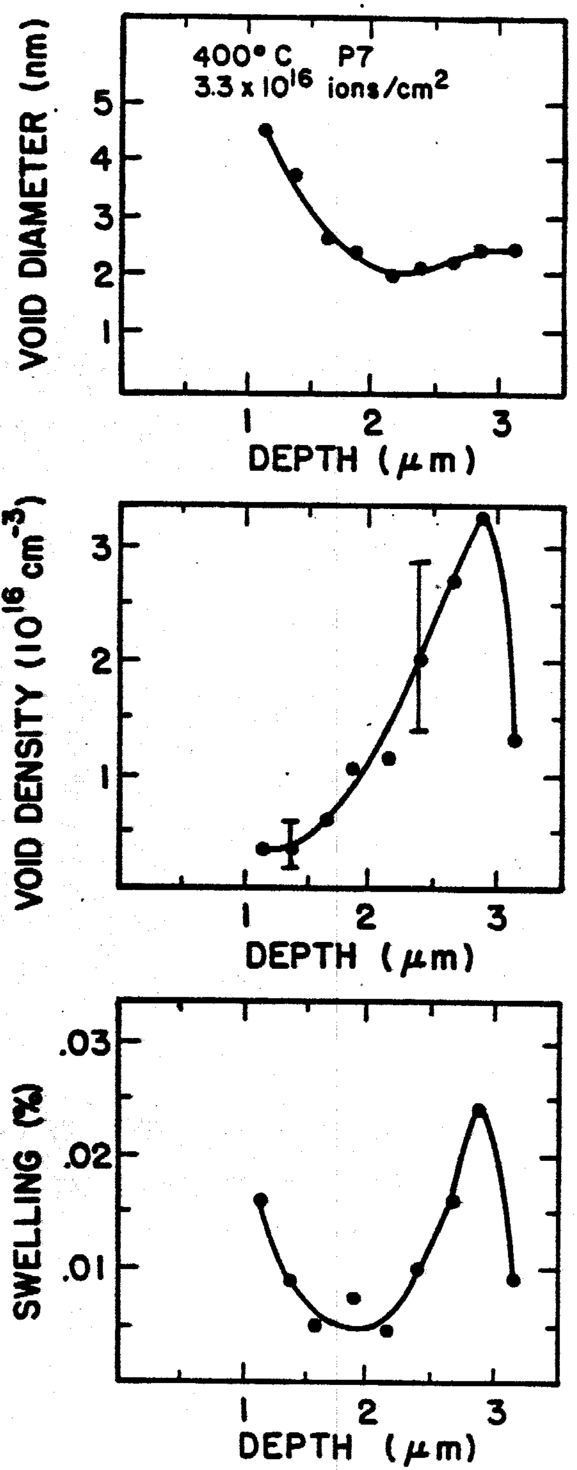

Fig. 5.4. Void parameters of P7 irradiated to 10 dpa at 1 μm at 400°C. The condition of the plated sample did not allow analysis at depths < 1 μm.

Table 5.2. Dislocation Structure for Ion-Irradiated P7 Alloy

Temperature (°C)	Dose (dpa)	Average Loop Diameter (nm)	Loop Density (cm^{-3})	Network Density (cm^{-2})
400	10	13	1.4×10^{16}	---
	40	14	1.4×10^{16}	---
500	2.4	19	2.0×10^{15}	5×10^{9}
	10	21	2.2×10^{15}	4×10^{9}
500	10	25	2.5×10^{15}	6×10^{9}
	40	28	2.4×10^{15}	7×10^{9}
550	3	32	1.0×10^{14}	2.1×10^{10}
	12	31	1.2×10^{14}	1.9×10^{10}
650	2.3-100	---	---	$1\text{-}3 \times 10^{10}$

2.4 μm range (40 dpa) of the bombarding ions (2.0 nm). In addition, the cavity number density increased from 1 to 3 x 10^{16} cm^{-3} after the approximate 2.5 μm depth which corresponds to the calculated end of range of the injected ion species. Note in Fig. 5.4 that the range of void density suppression does not match the 2.0-2.5 μm range (Fig. 2.1) of the injected ions. This may be due in part to the estimated profile of the implanted ions. Monte Carlo calculations show a more skewed range distribution of ions with a tail extending towards the target surface.(3) Figure 5.5 shows the TEM micrographs which span

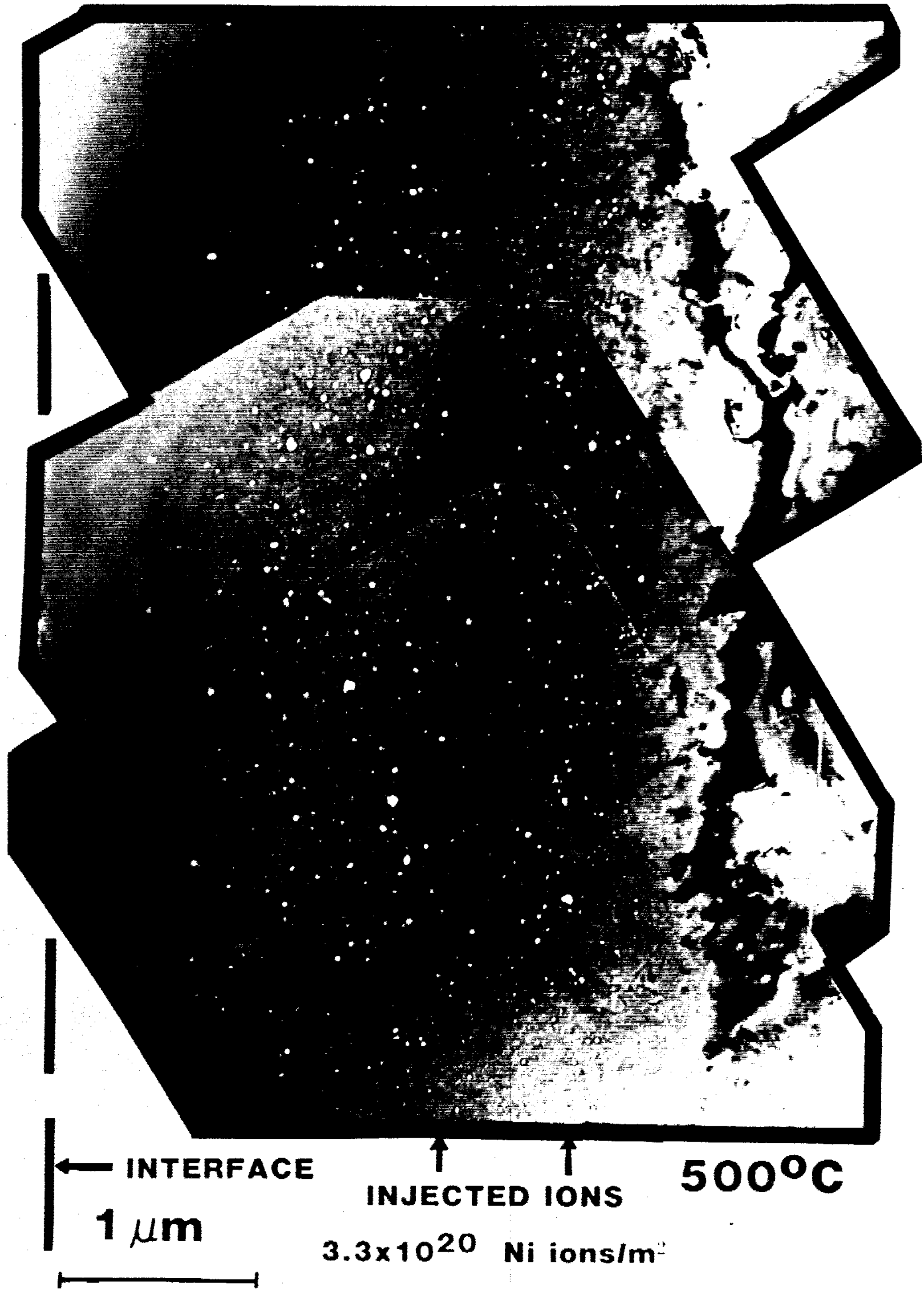

Fig. 5.5. TEM micrographs of the P7 alloy irradiated to 10 dpa at 1 μm at 500°C. Note the band of suppression of void size and number density which occurs over depths corresponding to the range of the injected nickel ions.

the entire damage region of the high fluence (40 dpa peak) P7 sample irradiated at a temperature of 500°C. Figure 5.6 shows the average cavity diameter, cavity density, and cavity-induced swelling as a function of distance from the sample surface for the low (10 dpa peak) and high fluence (40 dpa peak) irradiation conditions. It can be seen in the high fluence sample in Fig. 5.6 that there is a suppression in the average cavity diameter and number density in a region approximately 2.0 to 2.6 μm from the sample surface. This region is coincident with the range of the bombarding nickel ions. The suppression of cavity growth(4) and cavity density (nucleation)(5,6) in the 400° and 500°C samples is thought to be caused by these injected ions which provide interstitials in excess of the Frenkel defects produced during the irradiation.

A discrepancy exists, however, in the low fluence 500°C sample where no dip in the density is observed at the peak damage region. This result may be attributed to the difficulty in distinguishing small cavities (1-2 nm) from artifacts in a foil 100 nm thick and therefore the discrepancy lies within the error estimation of the density. Also, note that the dpa level at 1 μm in the high fluence sample (10 dpa at 1×10^{-3} dpa/s) was the same as the peak dpa value of the low fluence sample (at 4×10^{-3} dpa/s), yet the cavity number density was slightly greater in the peak damage region of the low fluence sample (see Fig. 5.6).

No suppression in cavity size or density was noted in a P7 sample irradiated to 3 dpa at 1 μm at 550°C. Figure 5.7 shows the

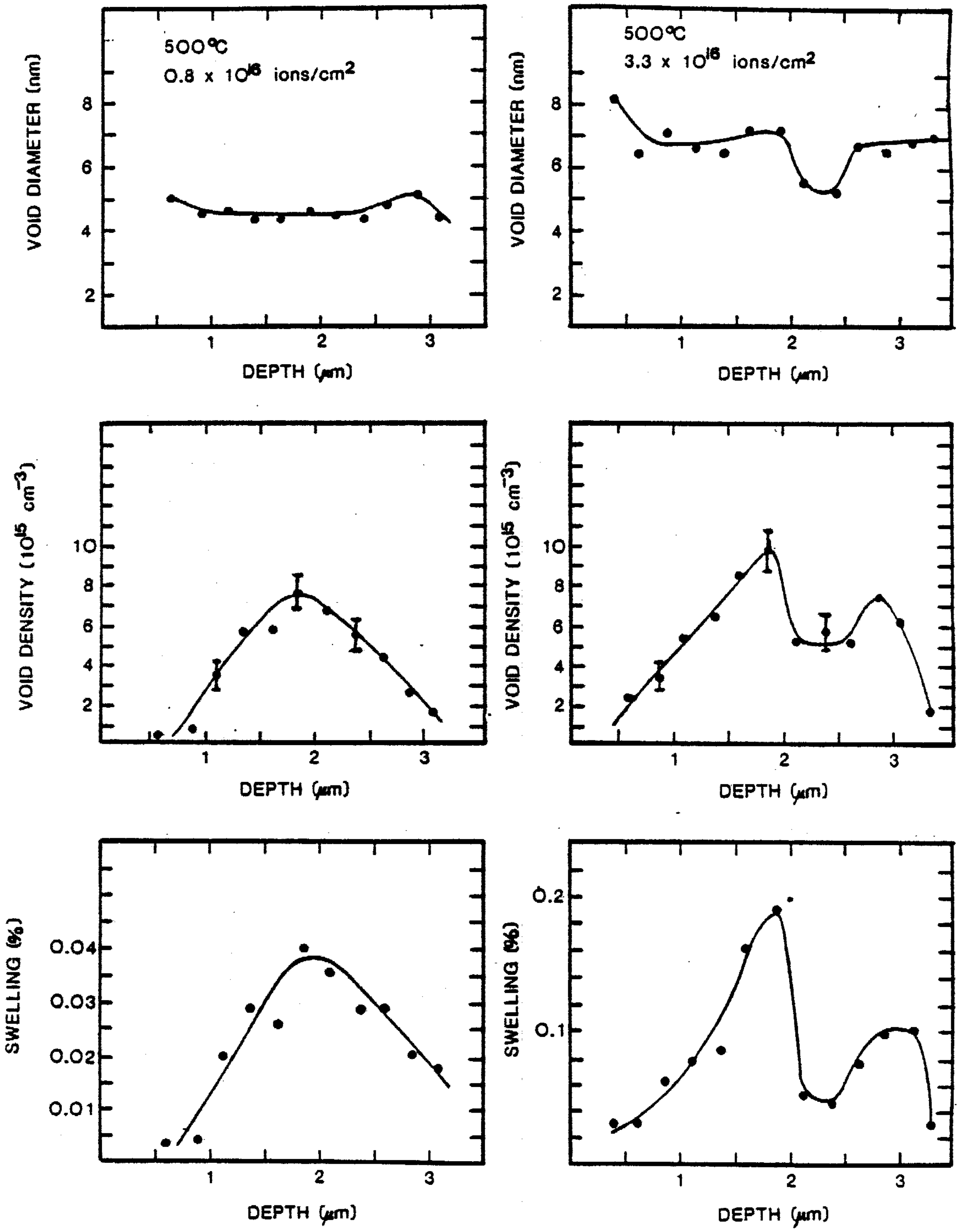

Fig. 5.6. Void parameters of P7 samples irradiated to doses of 2.4 dpa and 10 dpa at 1 μm at 500°C. A 30% decrease in the average cavity diameter and a 50% decrease in the cavity number density occurred over 2-2.5 μm depths.

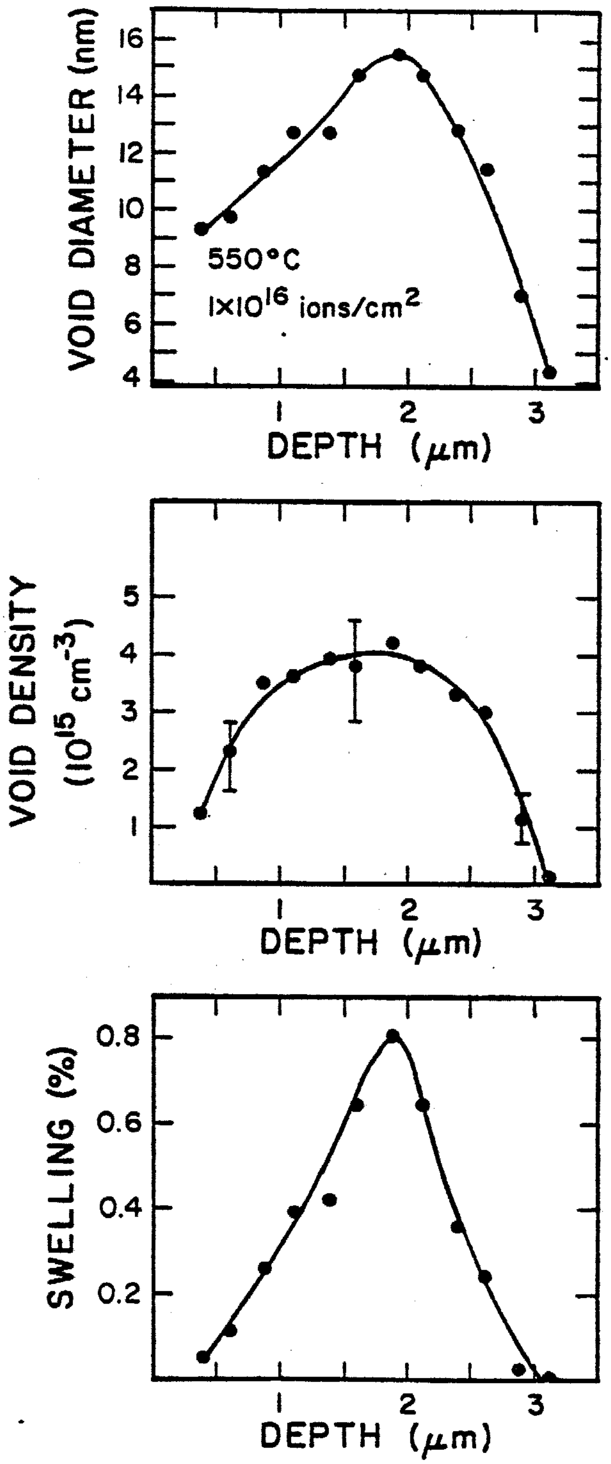

Fig. 5.7. Void parameters of P7 irradiated to 3 dpa at 1 μm at 550°C. Both the average cavity diameter and number density are seen to be maximum near the damage peak at 2.2 μm.

void parameters obtained from this specimen which was irradiated using 14 MeV Cu-ions. Both the average cavity size (16 nm) and the cavity density (4.2×10^{15} cm^{-3}) are maximum at the peak damage region.

A.2. 650°C Irradiations of P7

Samples of as-received P7 were irradiated at 650°C to four fluence levels (see Table 5.1). This temperature is near the peak swelling temperature for 4 MeV Ni-ion-irradiated (at 2×10^{-3} dpa/s) P7 reported by Packan and Farrell.(7) Figure 5.8 plots the swelling versus temperature data for this study at 40 dpa along with that of Farrell and Packan taken at 70 dpa. The swelling value at 40 dpa at 550°C in this study was linearly extrapolated from the 12 dpa swelling value assuming a 0.3%/dpa swelling rate. Also, note the close agreement in the magnitude of swelling between the 68 dpa, 650°C data point from this study with the data of Farrell and Packan.

Figure 5.9 displays the low contrast TEM micrographs which highlight the voids present in the 2.4 dpa, 1 μm and the 10 dpa, 1 μm samples. It is apparent that a bimodal void size distribution has developed in the peak damage region. To aid in distinguishing the two distributions, cavities > 100 nm were classified as "large voids" whereas those < 100 nm were labeled "small voids" in the void parameter graphs in Fig. 5.10. The diameters of the "large voids" in the high fluence specimen approach the value of the TEM specimen thickness in this region (~ 250 nm). Hence, many of these voids intersect the foil surface. Stereo microscopy analysis in thicker regions of

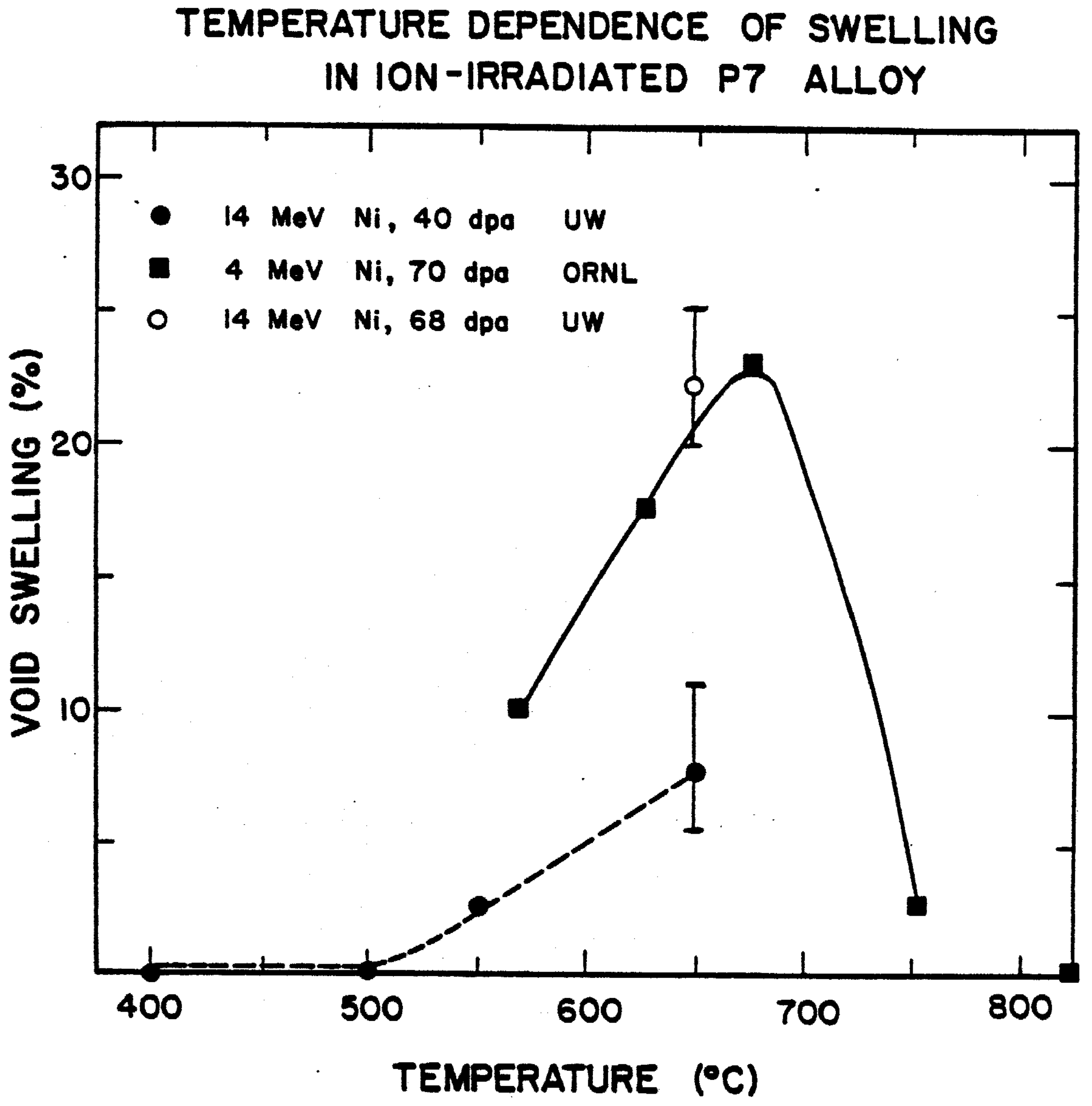

Fig. 5.8. Temperature dependence of swelling of P7 at 70 dpa (ORNL) and 40 dpa (this study). Note the excellent agreement of the swelling level at 68 dpa (this study) with the data of Packan and Farrell(6) at 70 dpa at 650°C.

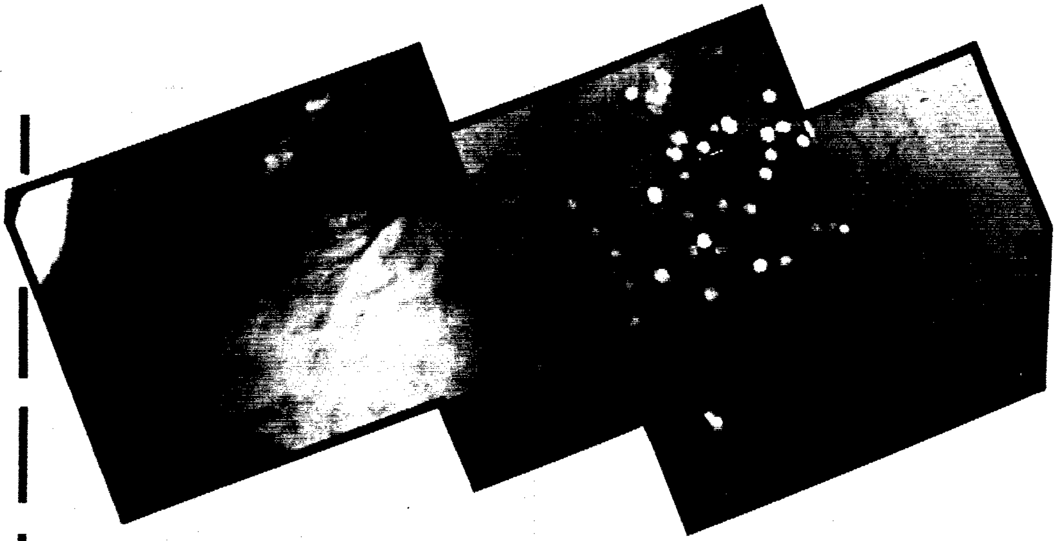

0.8 x 10^{16} 14 MeV Ni Ions/cm^2

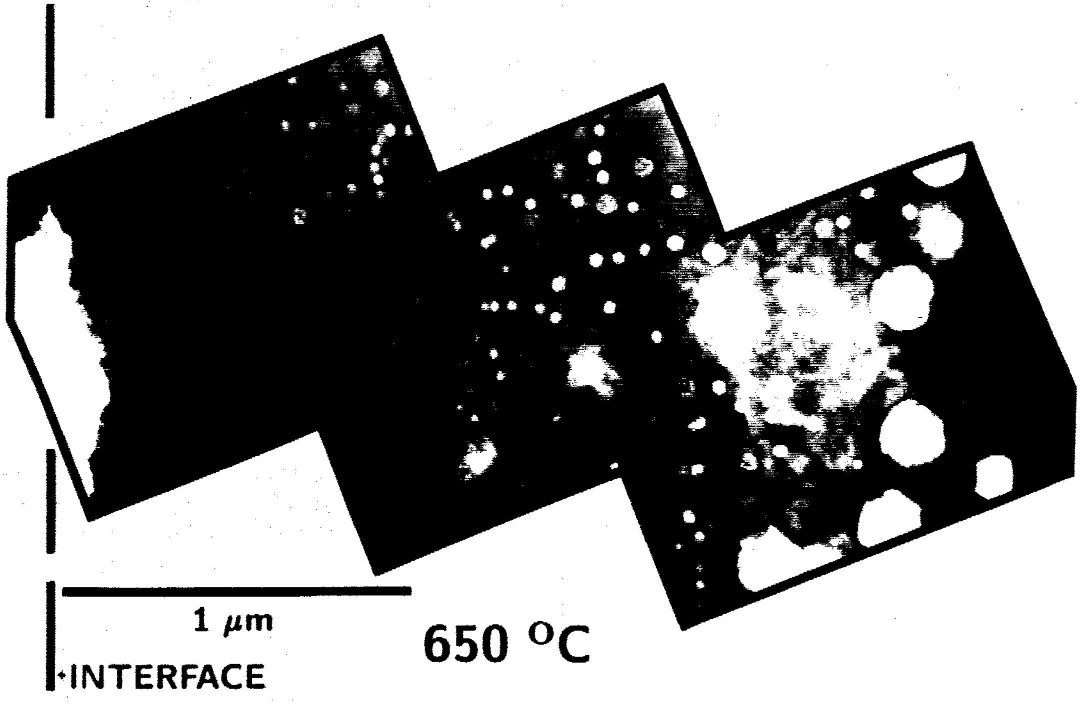

3.3 x 10^{16} 14 MeV Ni Ions/cm^2

Fig. 5.9. Low contrast TEM micrographs of P7 samples irradiated to doses of 2.4 dpa and 10 dpa at 1 µm at 650°C. The voids at the 2.2 µm in the low fluence sample are the precursor for the large voids seen at the peak damage depth in the high fluence sample.

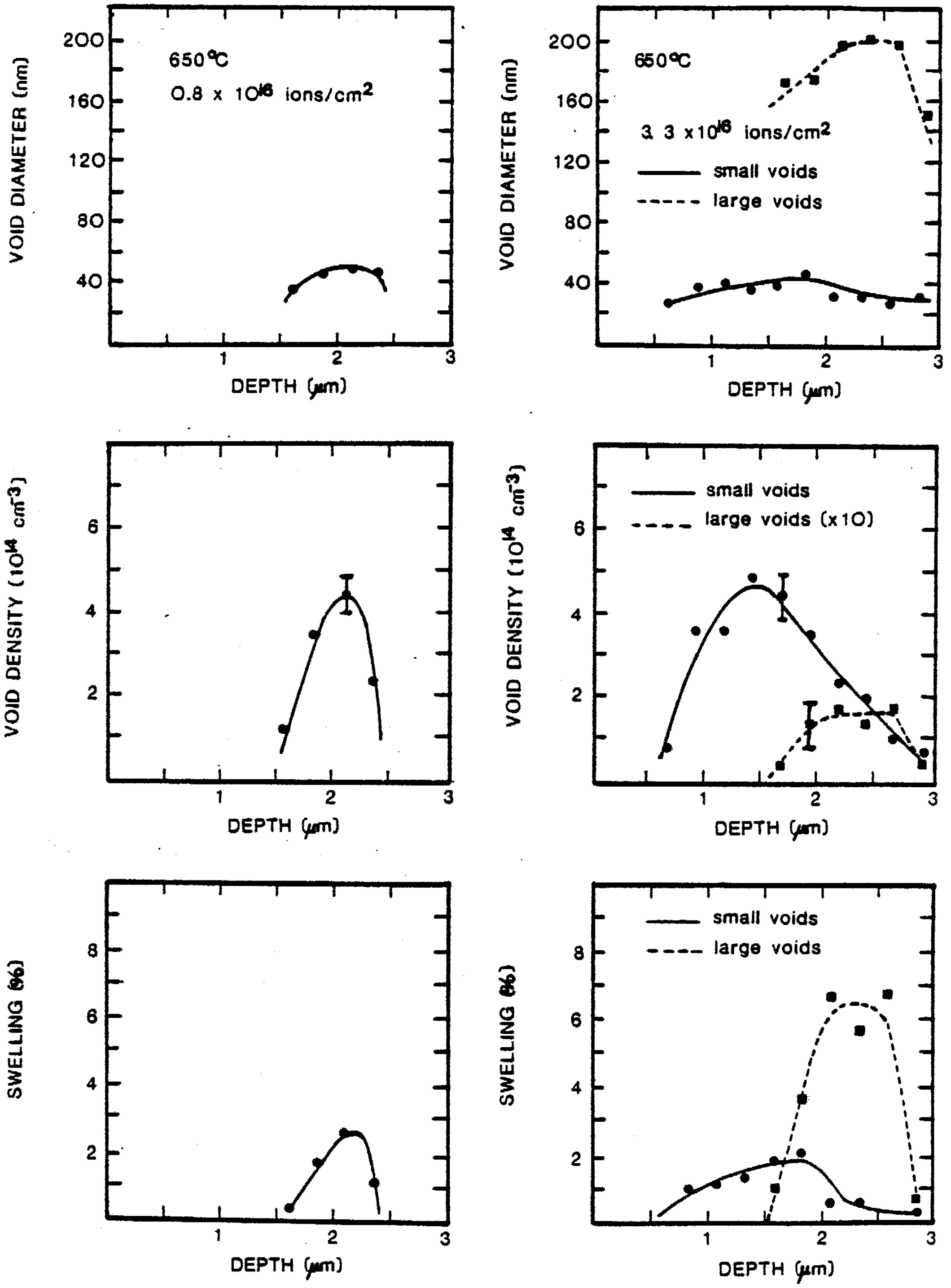

Fig. 5.10. Void parameters of P7 irradiated to 2.4 dpa and 10 dpa (at 1 µm) at 650°C. Due to the presence of a bimodal void size distribution in the high fluence sample, voids > 100 nm were classified as "large voids" while those < 100 nm were labeled "small voids."

the foil revealed that these features are not artifacts, but are completely contained within the specimen. Figures 5.9 and 5.10 suggest that the voids present at the low fluence are the precursor distribution in the high fluence sample. A denuded zone ~ 0.6 μm in width from the foil surface is still present in the 10 dpa, 1 μm sample. The absence of voids in this region is attributed to the diffusion of defects to the free surface. Garner and Thomas(7) have shown in HVEM studies that a 0.6 μm void-free zone also exists at a dose of 6 dpa in 316 SS at 650°C.

Two additional samples of P7 were irradiated at 650°C. A 17 dpa, 1 μm sample was irradiated at ~ 2×10^{-3} dpa/s at 1 μm which is about a factor of 2 higher than the other P7 samples (see Table 5.1). The resultant cavity formation can be seen in Fig. 5.11 with the parameters given in Fig. 5.12. Both the average cavity diameter and the density are seen to increase with depth. The second sample was irradiated to 25 dpa at 1 μm at ~ 1×10^{-3} dpa/s. Figure 5.13 gives the void parameters obtained from this specimen. The depth-dependent void size is again similar to the 10 dpa, 1 μm sample, whereby large (~ 200 nm) voids form in the peak damage region. Figure 5.14 displays a low contrast/high contrast pair which highlight the voids and dislocations present in this sample at the 2 μm depth. The intervoid network density in this region is 2×10^{10} cm^{-2}.

In an attempt to remove the oxygen from the matrix of P7, two P7 foils 0.020" (0.05 mm) thick were annealed at 1050°C for 120 hours at a total chamber pressure < 10^{-10} torr. Details of the High Vacuum

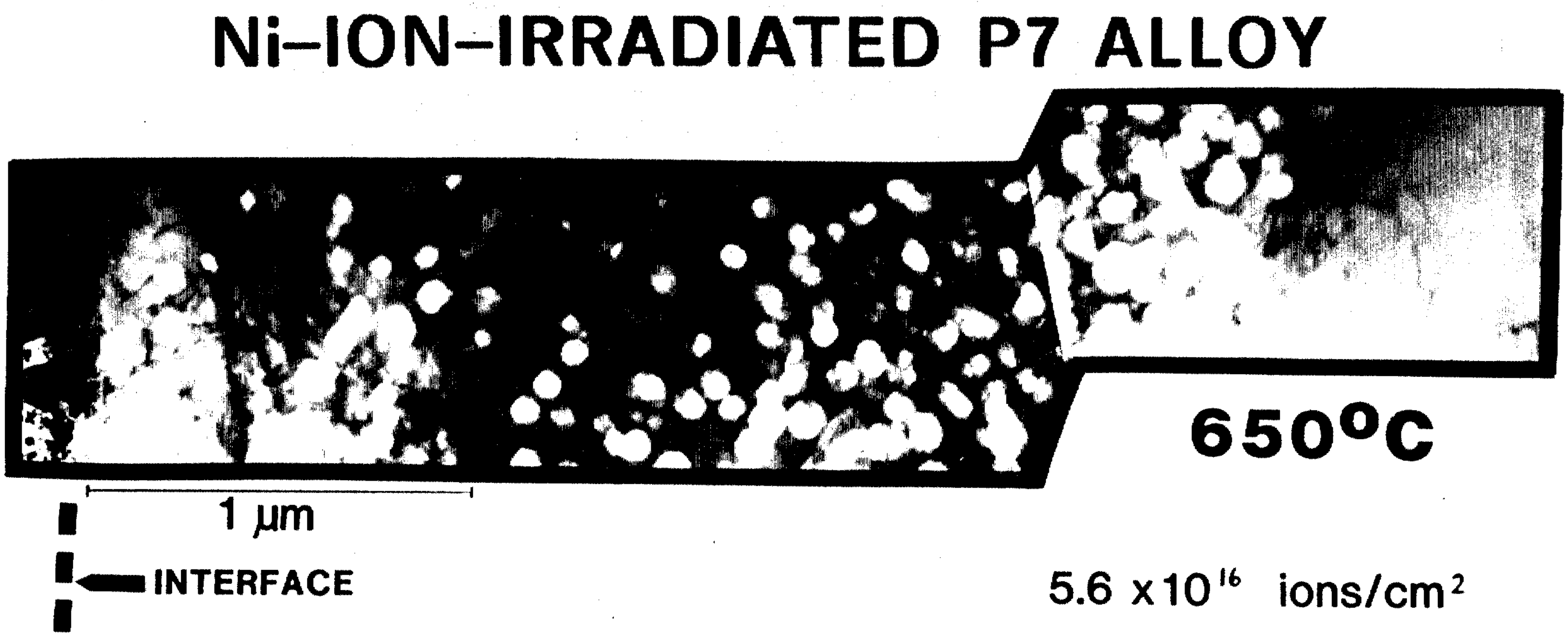

Fig. 5.11. Low contrast TEM micrographs of a P7 sample irradiated to 17 dpa at 1 μm at 650°C.

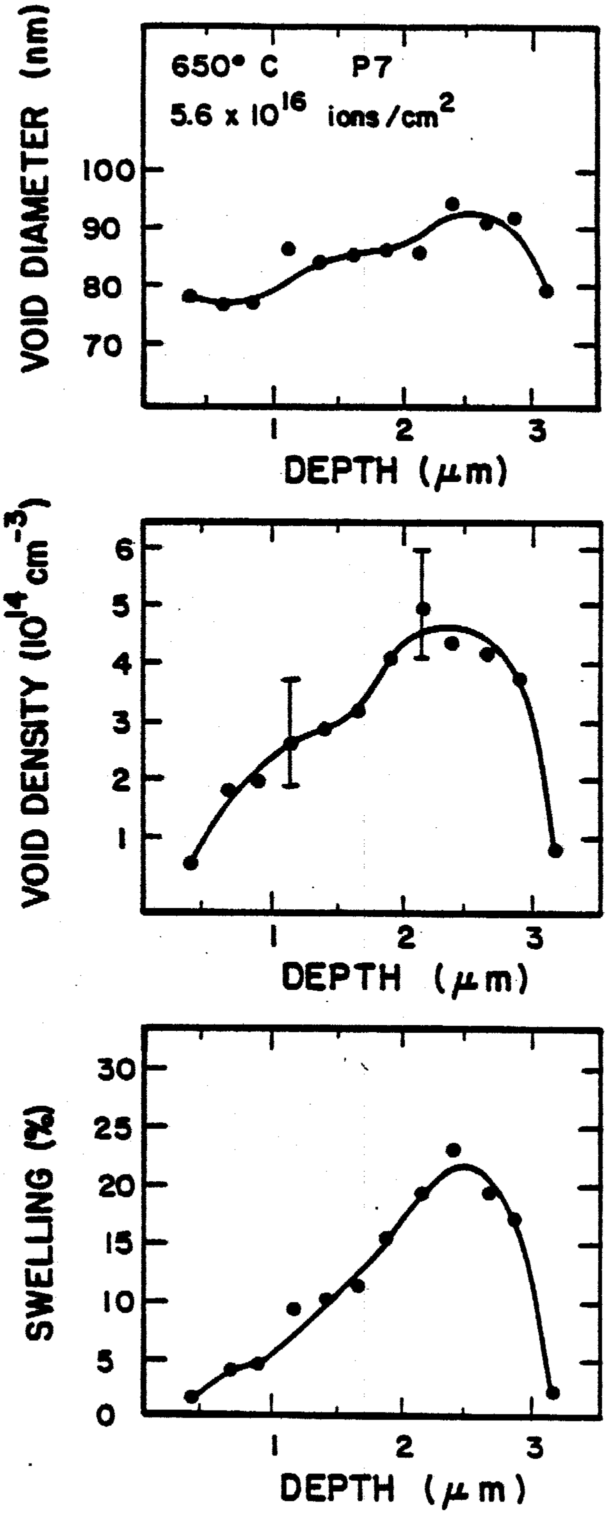

Fig. 5.12. Void parameters of P7 irradiated to 17 dpa (at 1 μm) at 650°C. The absence of 200 nm voids is attributed to the increased cavity nucleation due to the higher damage rate experienced in this sample.

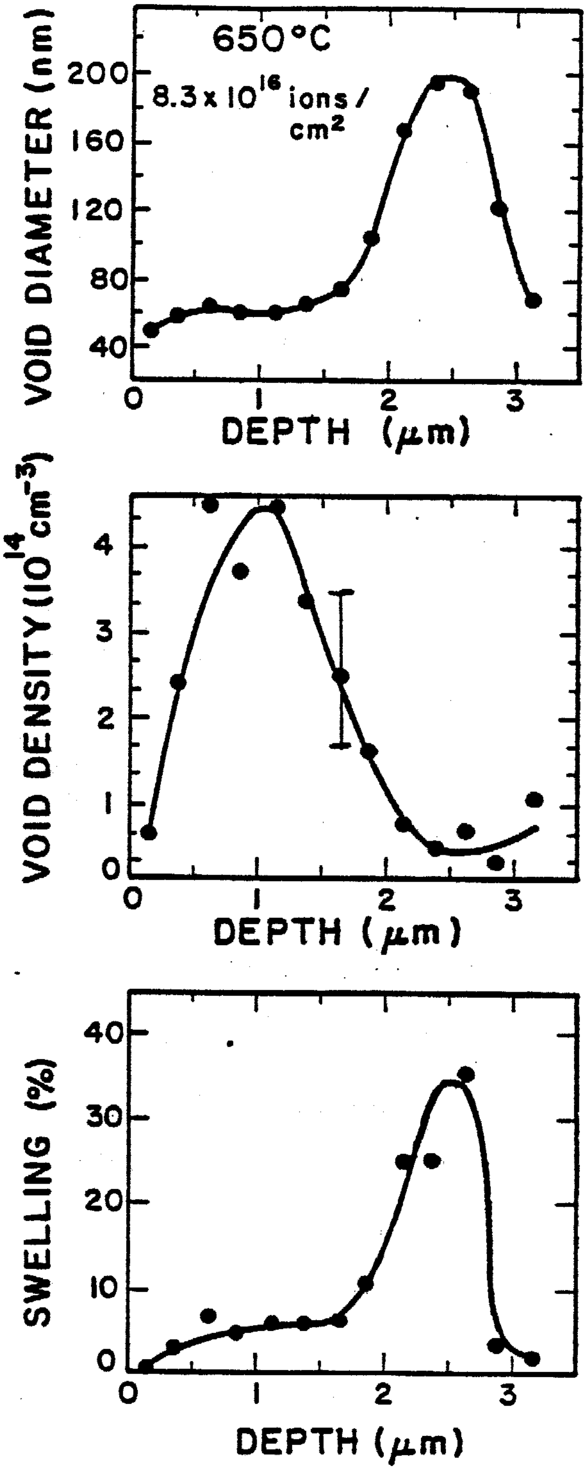

Fig. 5.13. Void parameters of P7 irradiated to 25 dpa (at 1 μm) at 650°C. Note the large (200 nm) voids in the peak damage regions. There were no small cavities in this region at this dose.

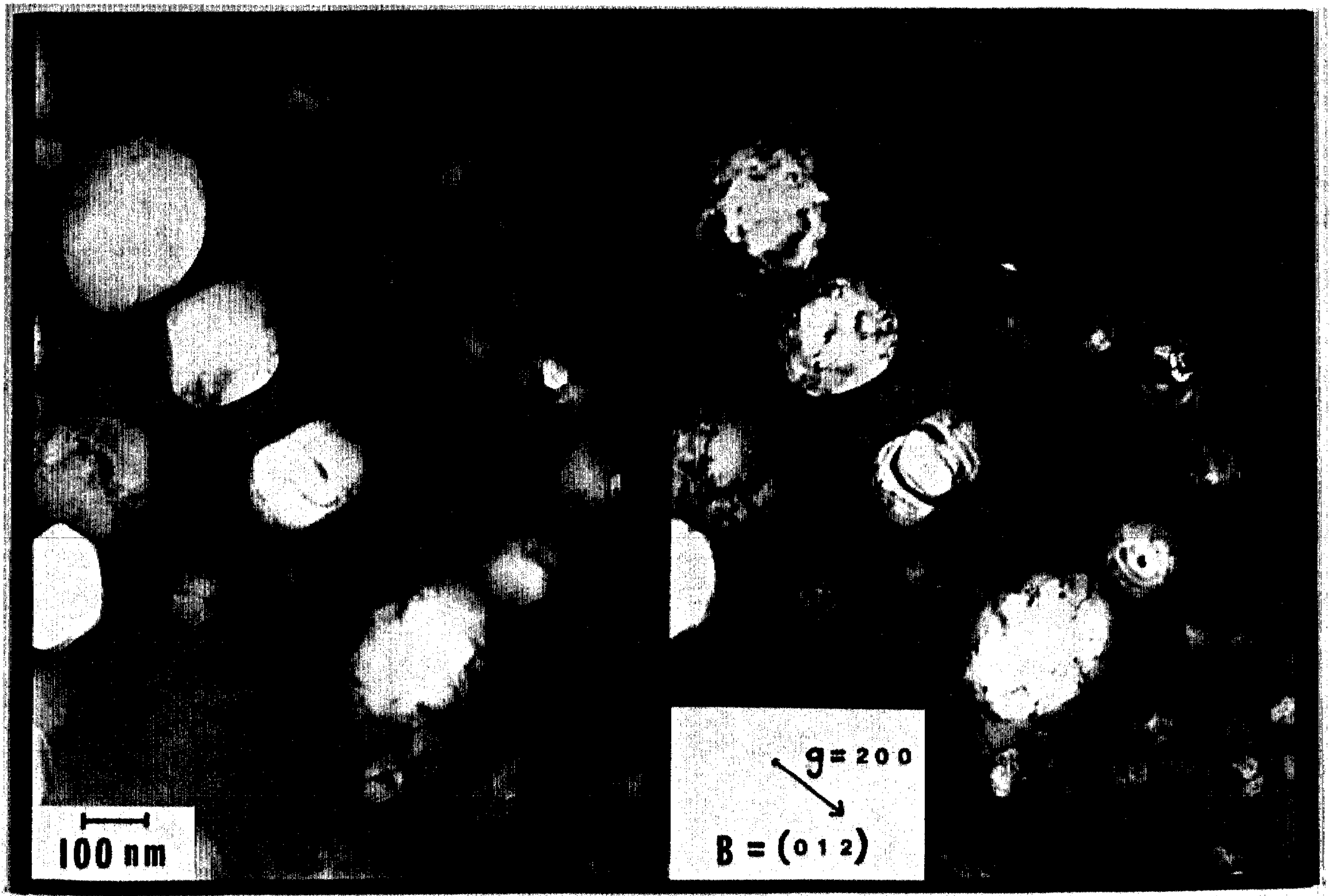

Fig. 5.14. Low and high diffraction contrast at the 2 μm depth in the P7 alloy irradiated to 25 dpa (at 1 μm) at 650°C. Note the coalescence of the two void in the centers of the micrographs. The intervoid dislocation density was determined to be 1.7×10^{10} cm^{-2}.

Furnace facility used for the anneal are given elsewhere.(9) Assuming an oxygen partial pressure of 2 x 10^{-11} torr, application of Sievert's Law yields:

$$x \text{ (at. frac.)} = \sqrt{p_{O_2}} \exp\left(-\frac{\Delta G_{SOL}}{RT}\right) . \quad (5.1)$$

Using the free energy of solution given by Fromm and Gebhardt(10) for $1/2\ O_2 = 0$ (in γ-Fe), $\Delta G_{SOL} = -174.39 + 0.088\ T$ kJ/mole O, a resultant 30 appm concentration of oxygen is estimated to be contained in the annealed foils. This would be a factor of 30 down from the initial 1000 appm concentration. An EDS analysis of these outgassed specimens revealed that a slight modification of the alloying components had occurred during the high temperature anneal. The resultant composition of the alloy was determined by EDS analysis to be 62 Fe-18 Ni-14 Cr-6 Mo. These specimens were subsequently irradiated to doses of 5 and 10 dpa at the 1 μm depth at 650°C. No voids were detected throughout the 3 μm damage range in either sample. Figure 5.15 displays low and high contrast micrographs from the 5 dpa sample. No voids were detected in either sample throughout the complete damage range. The dislocation structure at this high irradiation temperature was 2-3 x 10^{10} cm^{-2} in the first 3 μm from the interface and about 10^{10} cm^{-2} in the region beyond the end of the damage range.

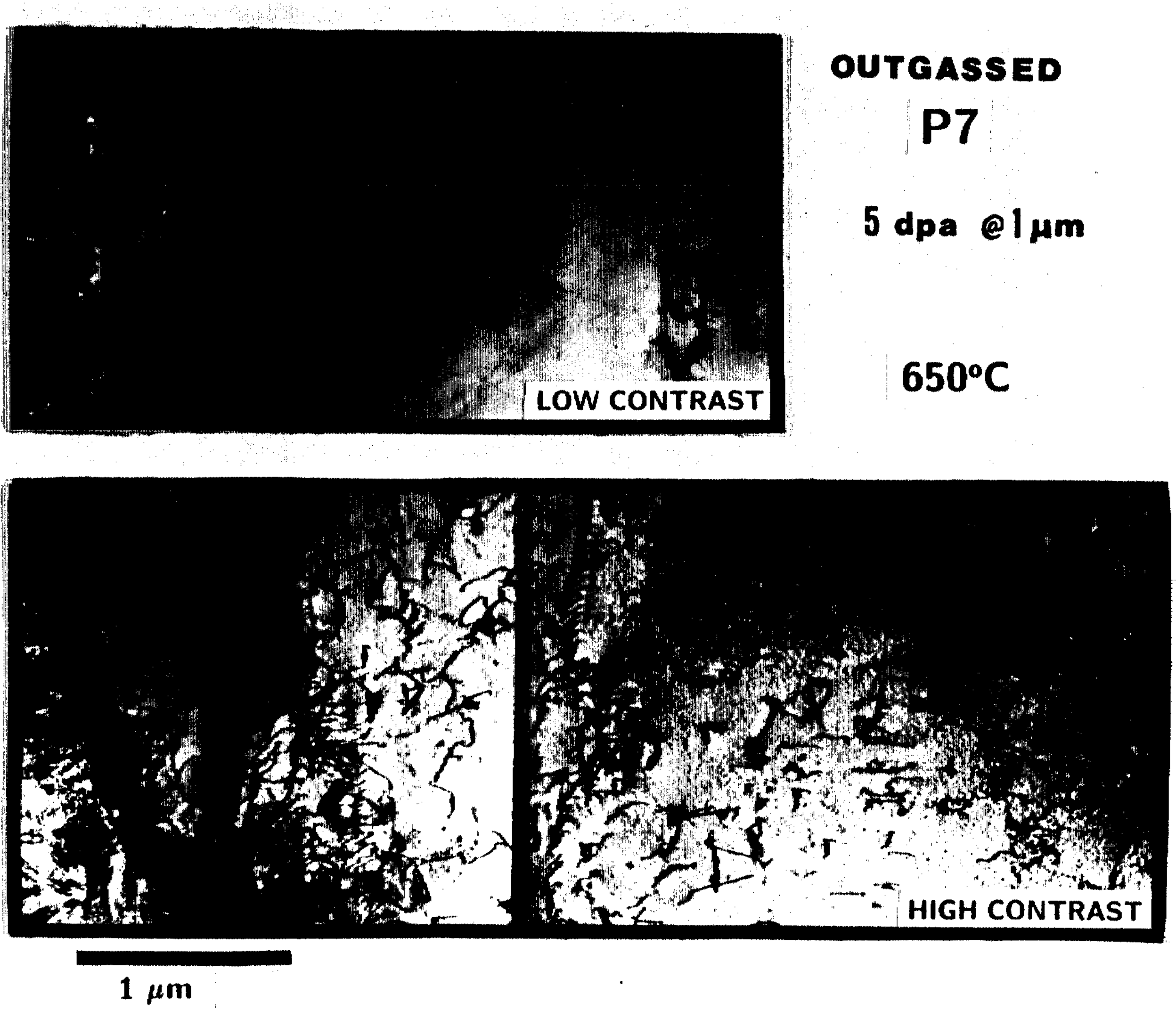

Fig. 5.15. Low and high diffraction conrast micrographs which span the damage range of the 5 dpa (at 1 μm) outgassed P7 sample irradiated at 650°C. No voids were detected in this 5 dpa sample nor an additional outgassed sample irradiated to 10 dpa (at 1 μm).

B. Nickel-Ion-Irradiated 316 SS

The 14 MeV nickel-ion irradiation of solution-annealed 316 SS produced a greatly different microstructural response compared to the P7 results. Radiation-induced or enhanced precipitation occurred over the entire 450-650°C irradiation temperature range surveyed. Heterogeneous void formation was detected over the 450-550°C temperature range with voids only forming only at precipitate interfaces. No 316 SS samples were irradiated below 450°C.

The precipitation over the range 450-550°C can be characterized as small (5-30 nm) blocks or rods which formed in stringers or as isolated particles. Irradiations at 600-650°C produced a radiation-induced phase identified as Fe_2P. No Fe_2P was observed in the control region beyond the 3 μm damage zone. In addition, no marked depth dependency was measured in precipitate size or density over the entire temperature range. These observations include a sample irradiated to 120 dpa (peak damage) at 500°C whose void and precipitation parameters were similar to an additional sample irradiated to 40 dpa (peak damage).

The dislocation parameters from the 316 SS samples are reported in Table 5.3. At these high doses, no marked depth (dose) dependency was noted in the dislocation parameters. Some faulted loops were found at 600°C after a dose of 40 dpa. Saturation in the network dislocation density at 2×10^{10} cm^{-2} was also noted between 550 and 650°C at these dose levels. Figure 5.16 displays the TEM micrographs

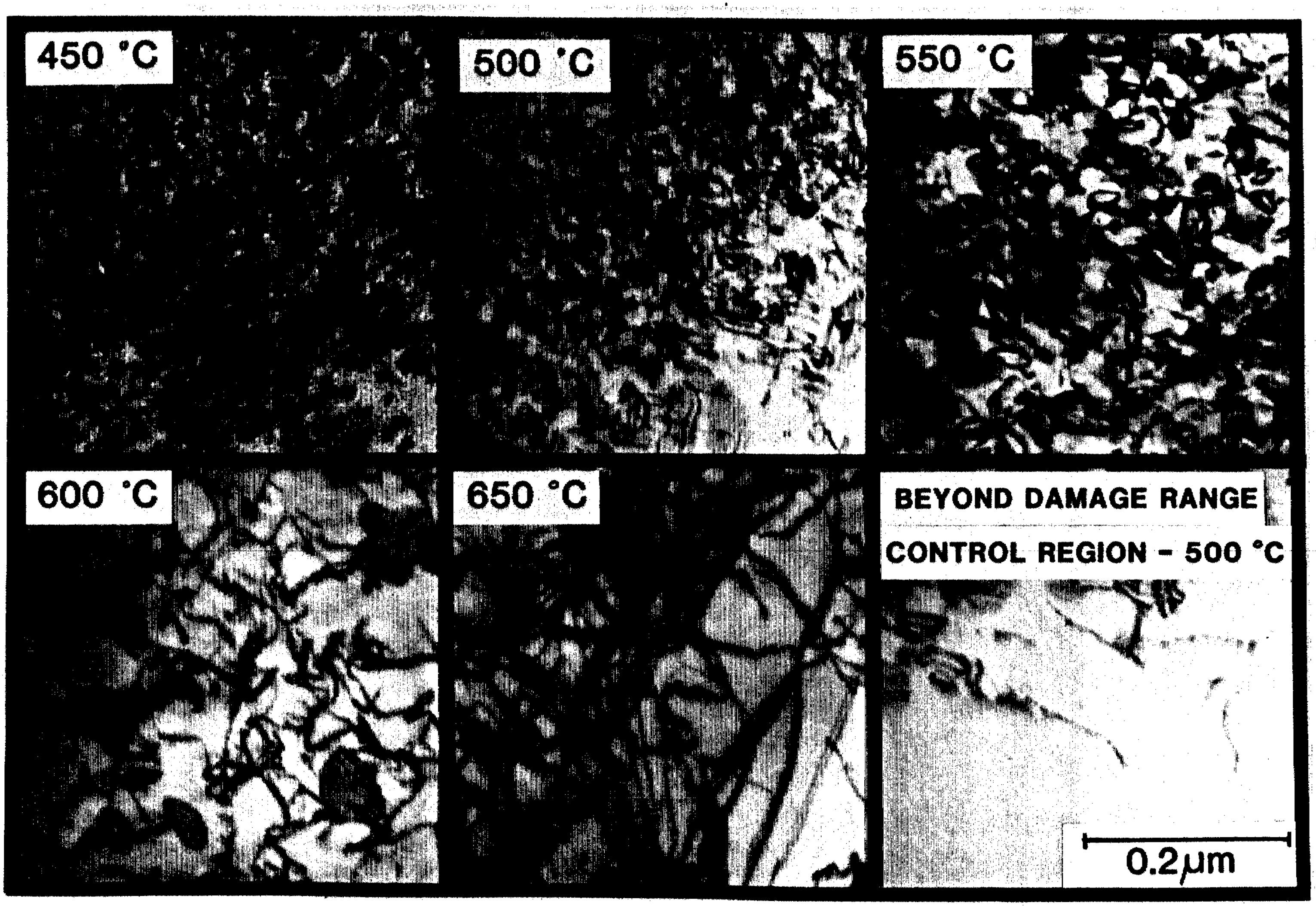

Fig. 5.16. Dislocation structure after 40 dpa in ion-irradiated 316 SS.

Note the loop to network transition with increasing temperature.

Table 5.3. Dislocation Structure for Ion-Irradiated 316 SS

Temperature (°C)	Dose (dpa)	Average Loop Diameter (nm)	Loop Density (cm^{-3})	Network Density (cm^{-2})
450	10*	30	2.8×10^{15}	---
	40**	32	3.0×10^{15}	---
500	10*	46	1.6×10^{15}	---
	40**	47	1.4×10^{15}	---
550	10*	42	1.3×10^{15}	1.0×10^{10}
	40**	34	2.0×10^{15}	2.1×10^{10}
600	10*	72	1.4×10^{14}	2.3×10^{10}
	40**	76	1.8×10^{14}	1.6×10^{10}
650	10*	---	---	1.7×10^{10}
	40**	---	---	2.0×10^{10}

---

*Taken at 1 micron from front surface, 0.8×10^{-3} dpa/s.

**Taken at 2.3 microns from front surface, 3.6×10^{-3} dpa/s.

which illustrate the temperature-dependent dislocation structures at a dose level near 40 dpa (at depths from 2 to 2.5 μm from the surface).

B.1. 450-550°C Irradiations of 316 SS

Voids were detected throughout the damage range at 450, 500 and 550°C. Figure 5.17 shows the void formation in the 450-550°C samples after a dose of 40 dpa. The voids formed at 450°C have a factor of 2 greater density (5×10^{14} cm^{-3}) and smaller average diameter (10 nm) than those at 500 and 550°C (2×10^{14} cm^{-3}, 25 nm). The depth-dependent void parameters of the 450°C sample are given in Fig. 5.18. A 50% increase in the average void diameter can be seen from the surface to the peak damage region at 2.2 μm. No definite trend can be determined from the density data which is scattered around 5×10^{14} cm^{-3}. Large error limits are ascribed to the cavity density measurement of this sample due to the small number of cavities (~ 20) counted at a given depth.

Two irradiations were performed at 500°C. Through-range micrographs of the 10 dpa (at 1 μm) and 30 dpa (at 1 μm) 316 SS samples are shown in Fig. 5.19. Their corresponding void parameters are given in Figs. 5.20 and 5.21, respectively. Both samples exhibited similar microstructural response. A slight (25%) increase in average cavity diameter is noted from the low damage, near surface depths to the damage peak. Also the cavity concentration is greatest near the peak damage depth (2.2 μm). It was difficult to determine whether the bombarding nickel ions as injected interstitials acted to suppress the nucleation or growth of cavities near the peak damage depths in the 450 and 500°C 316 SS samples as was observed in the P7 samples irradiated at 400 and 500°C. However, the nature of the void

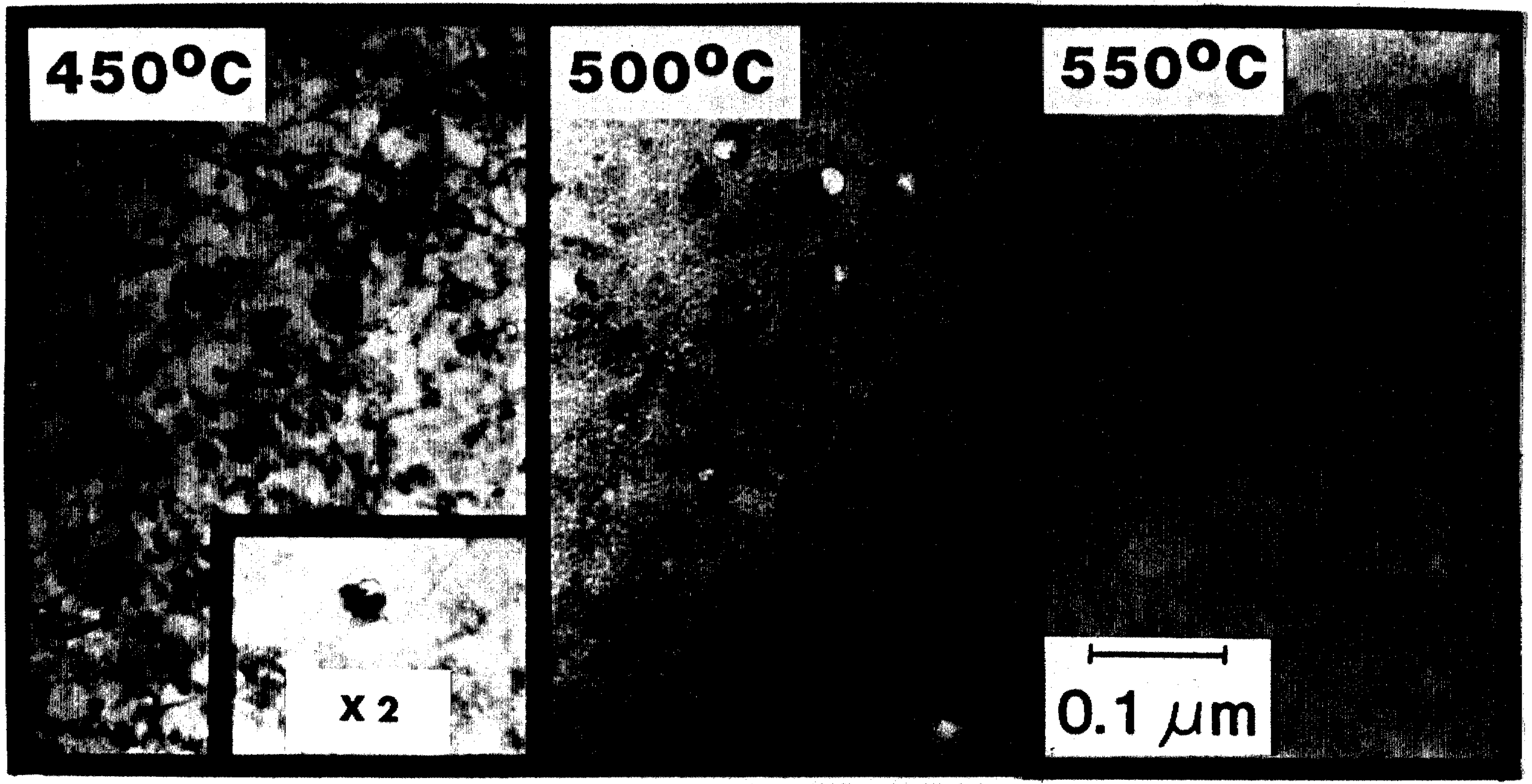

Fig. 5.17. Void-precipitate association in 316 SS irradiated to 40 dpa over 450 to 550°C.

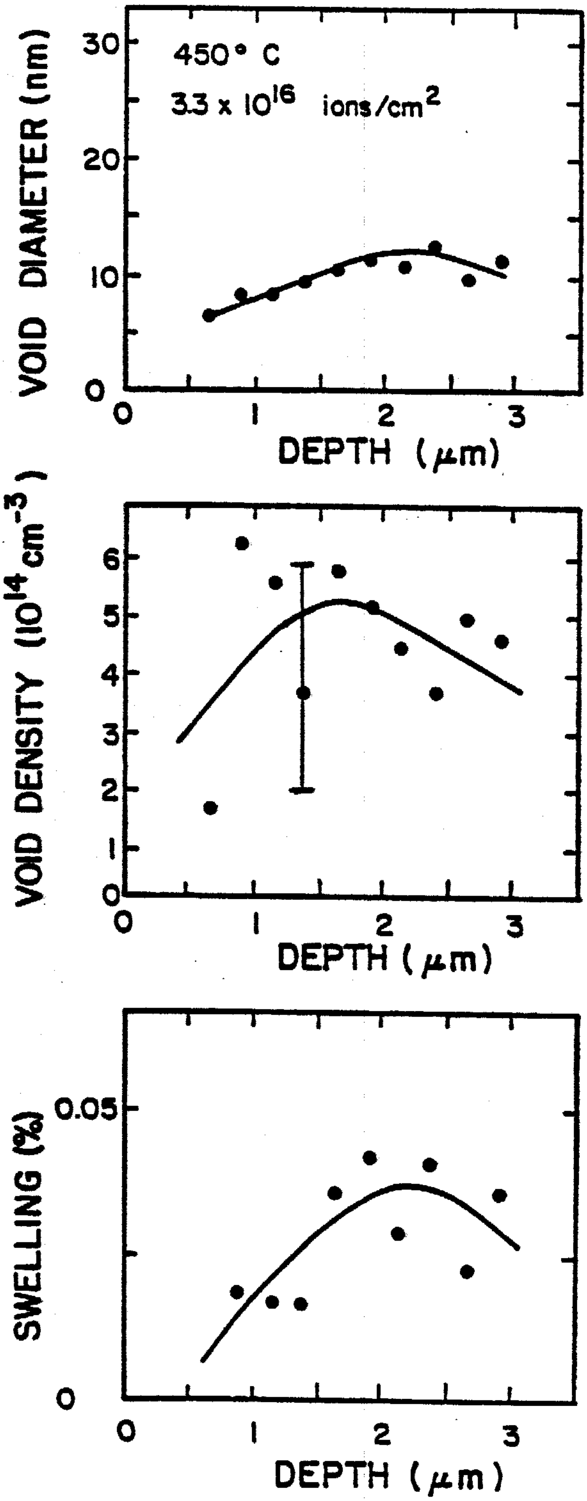

Fig. 5.18. Void parameters of 316 SS irradiated to 10 dpa at 1 μm at 450°C.

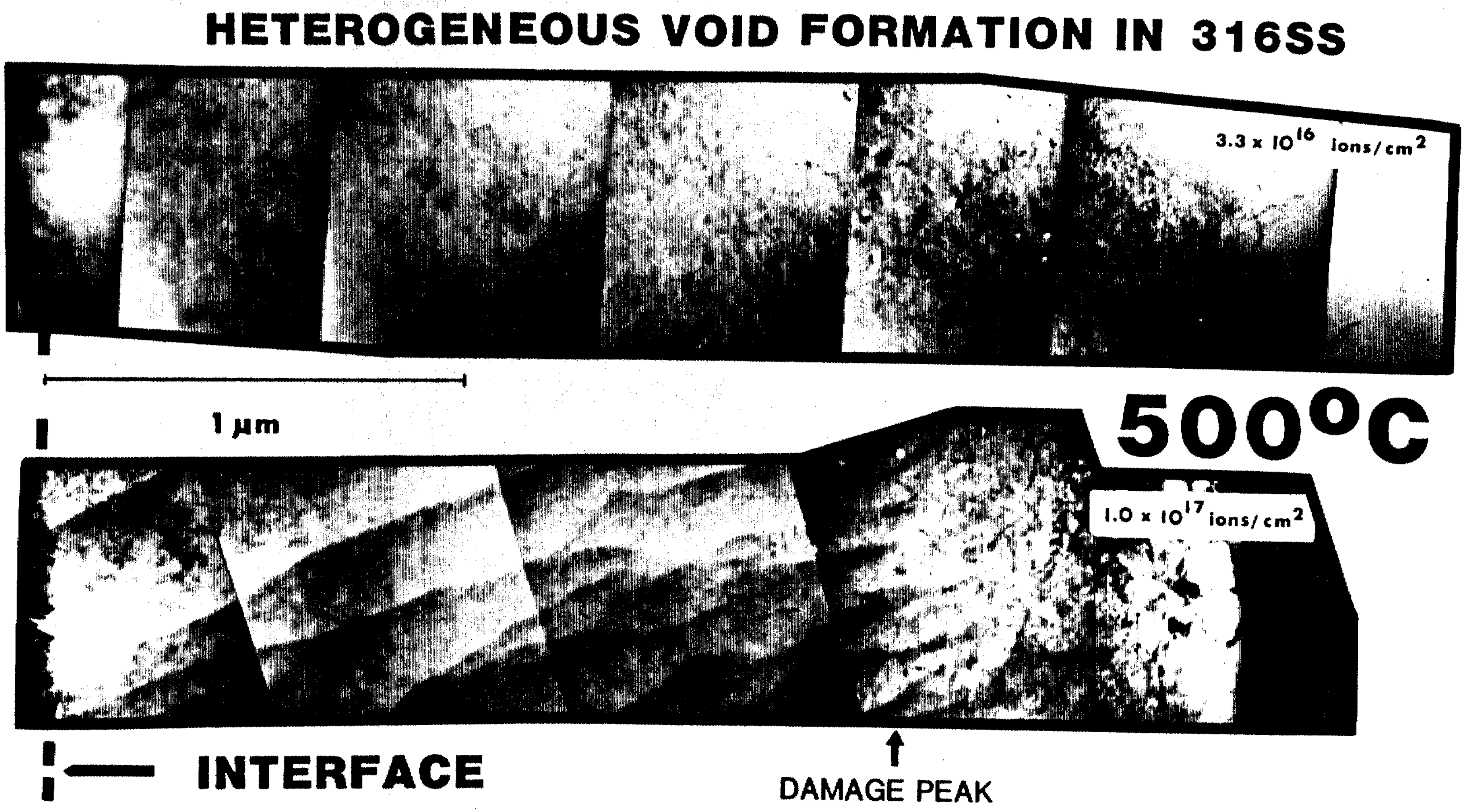

Fig. 5.19. Low-contrast, through-range micrographs of the 500°C 316 SS samples at 10 dpa (1 µm) and 30 dpa (1 µm). Note the predominance of precipitate associated voids at the damage peak.

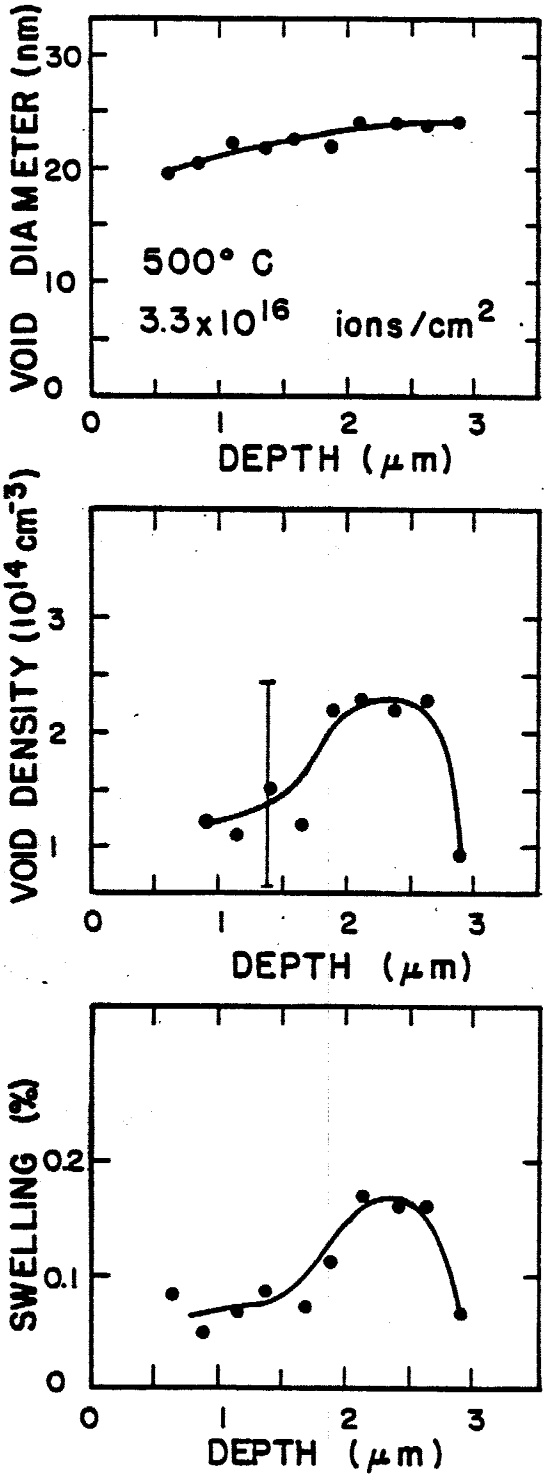

Fig. 5.20. Void parameters of 316 SS irradiated to 10 dpa at 1 μm at 500°C.

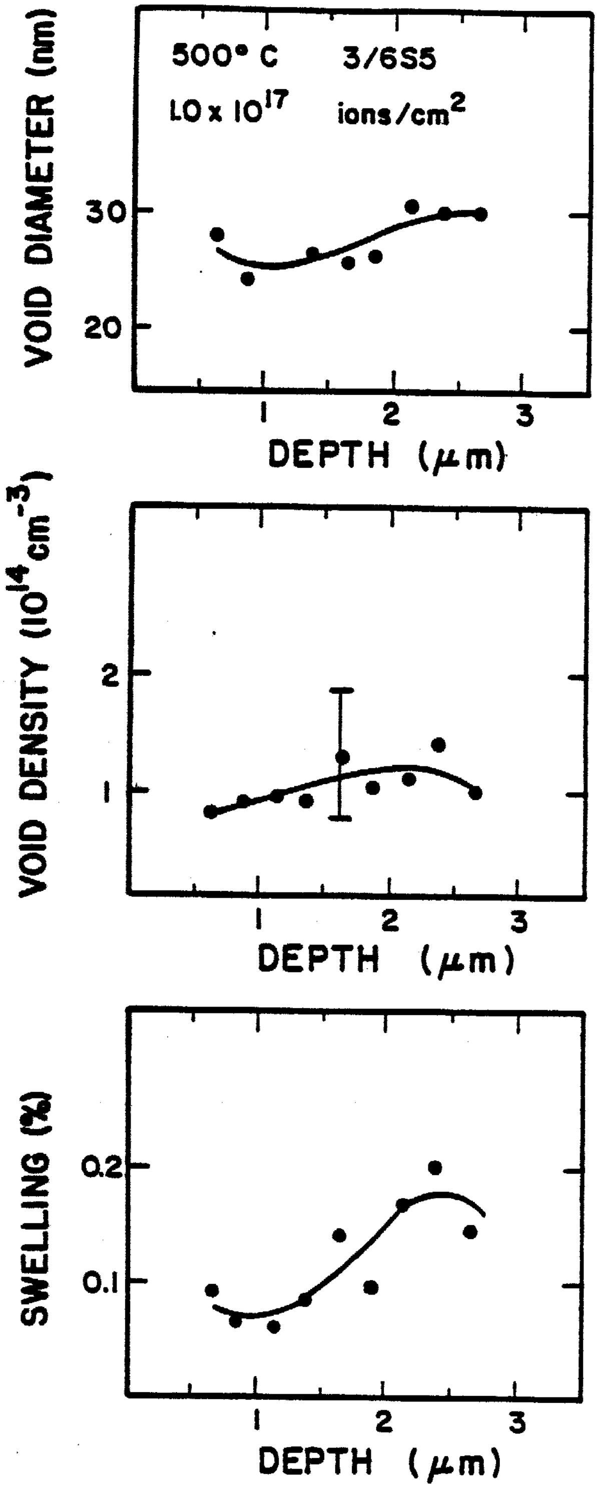

Fig. 5.21. Void parameters of 316 SS irradiated to 30 dpa at 1 μm at 500°C.

formation in the 316 SS was vastly different than that observed in the P7 alloy. In 316 SS, voids were only seen associated with precipitates, i.e. voids appeared to form at or in conjunction with a precipitate interface. This resulted in a low (~ 1×10^{14} cm^{-3}) cavity density in the 316 SS samples at 500°C which is approximately two orders of magnitude lower than the void density in the P7 sample (~ 1×10^{16} cm^{-3}) irradiated to 10 dpa (at 1 μm) at 500°C. Thus, due to the low density and heterogeneous nature of the cavity population, no suppression effects were observed in the 316 SS samples.

Similar void formation was seen at 550°C in a 10 dpa (at 1 μm) 316 SS sample. Figure 5.22 gives the void parameters which show that both the cavity diameter (25 nm) and density (2×10^{14} cm^{-3}) are maximum near the 2 μm depth. Figure 5.23 shows a through focus series of a typical void with an associated precipitate which formed at 550°C and a dose of 40 dpa.

B.2. 600-650°C Irradiations of 316 SS

In contrast to the 450-550°C results, no voids were detected in 316 SS samples irradiated to a peak damage level of 40 dpa at 600 and 650°C.

A key microstructural response of the 316 SS in the 600-650°C range was the formation of the Fe_2P phase. This phase has a thin-lathe morphology which often gives a needle-like appearance when viewed in a thin TEM foil. Figure 5.24 displays the through-range micrographs of the 600°C 10 dpa (at 1 μm) 316 SS sample. No apparent depth dependency was noted in the precipitate size or density. The

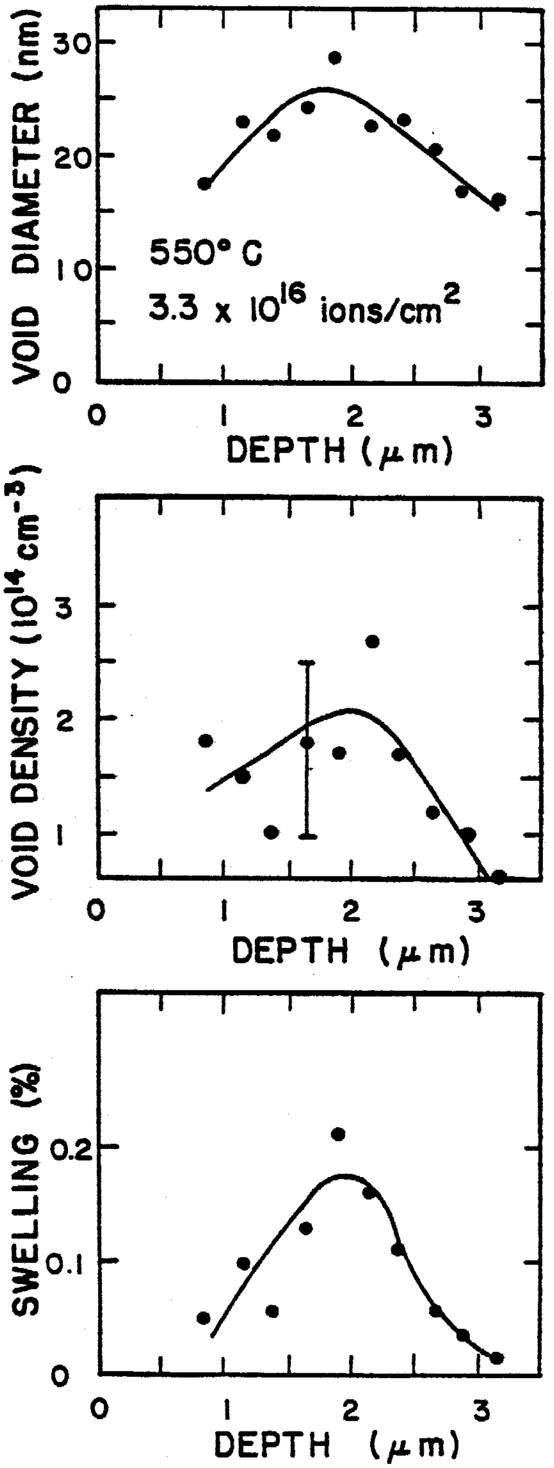

Fig. 5.22. Void parameters of 316 SS irradiated to 10 dpa at 1 μm at 550°C.

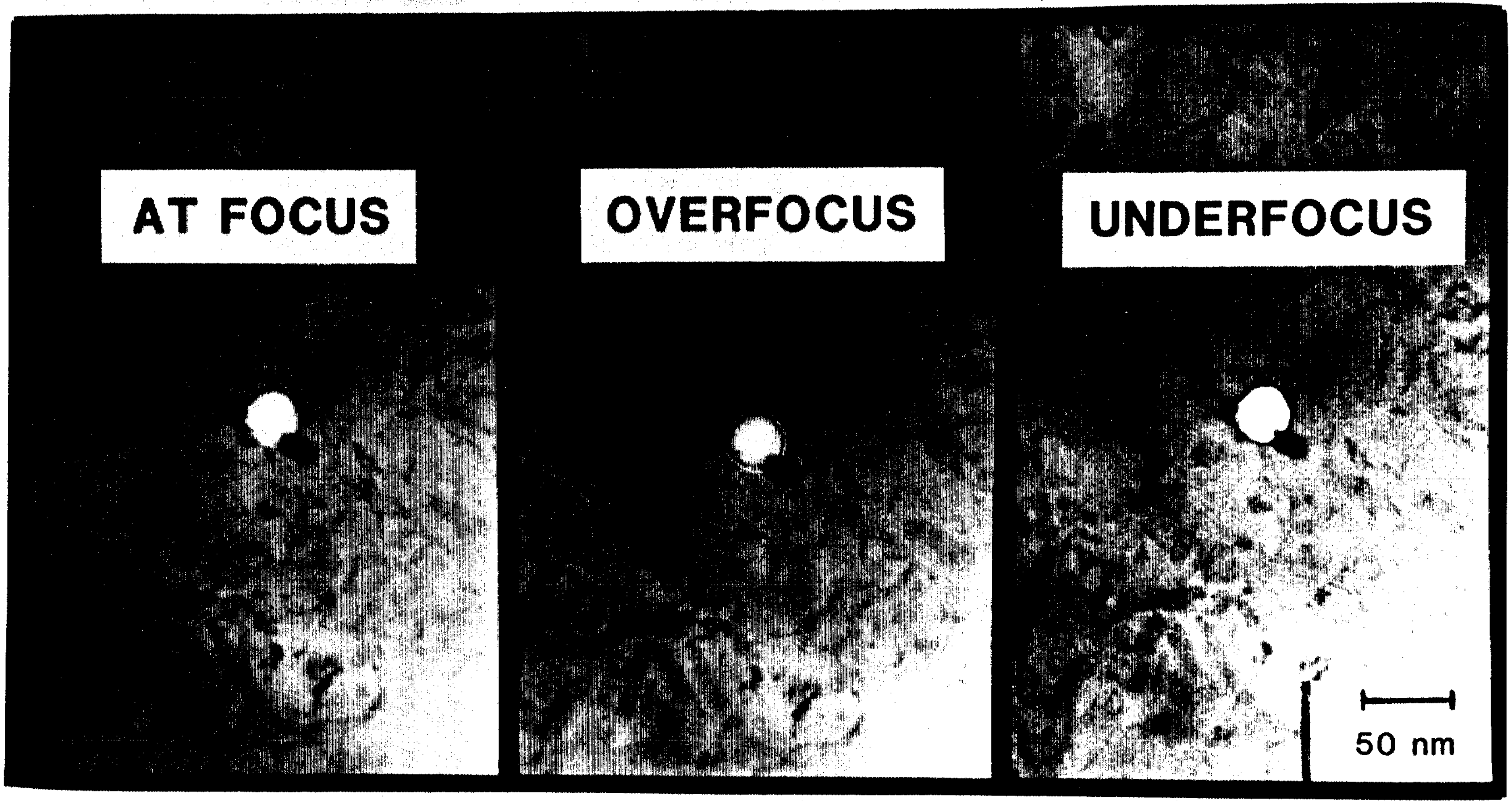

Fig. 5.23. Through-focus void/precipitate which formed at 550°C, 40 dpa.

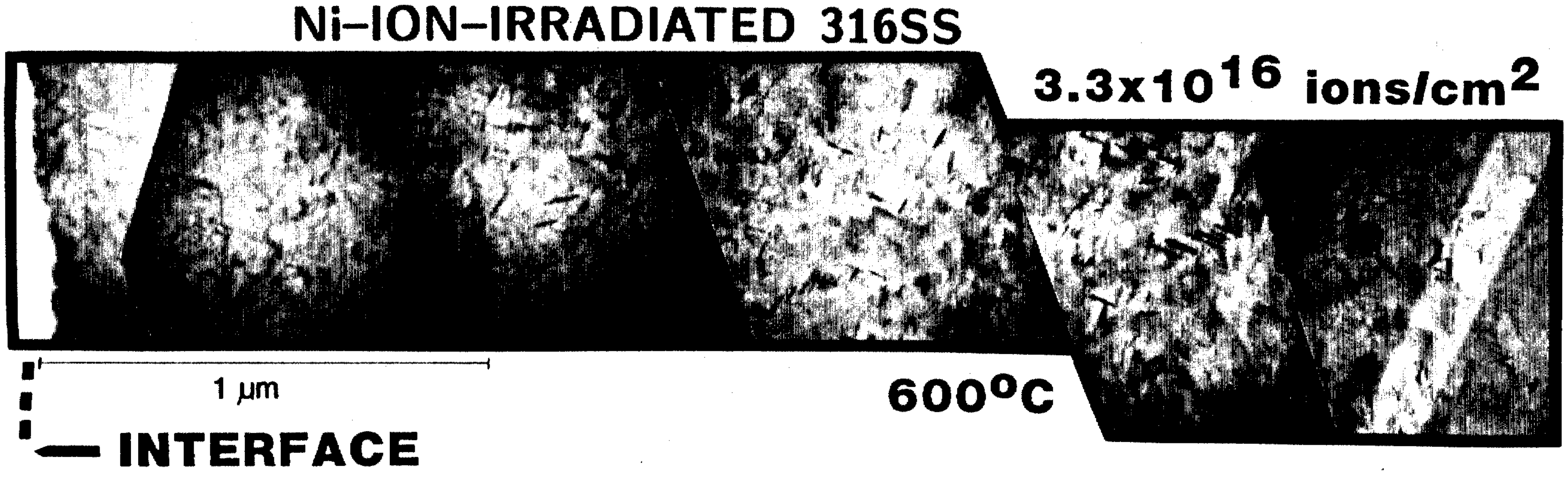

Fig. 5.24. Low-contrast micrographs of 316 SS irradiated to 10 dpa at 1 µm. Note the 50 nm Fe_2P needles throughout the 3 µm damage range.

precipitation response at 650°C can be seen in the through-range micrographs in Fig. 5.25. The iron phosphide precipitation at this temperature can be seen to be more coarse compared to the 600°C sample. A thermal precipitation response was also observed at 650°C and can be seen in the optical and TEM micrographs of Fig. 5.26. Figure 5.26 shows an optical micrograph of the plated 650°C 10 dpa sample which has been etched to reveal the thermally-induced grain boundary precipitation as well as precipitation throughout the 3 μm range from the surface over which displacement damage has occurred. The grain boundary precipitation was identified by electron diffraction as the $M_{23}C_6$ phase and is shown in the TEM micrograph in Fig. 5.26. Figure 5.26 shows Fe_2P precipitation at the 1 μm depth from this sample.

These needle-shaped precipitates which formed in the damage region are similar to those reported in dual-ion irradiation studies on 316-type stainless steels(11-13) as well as neutron-irradiated 316 SS.(14) Lee(14) had reported the Fe_2P phase to be "radiation enhanced" due to an account of Fe_2P formation in 321 SS(15) found after extensive thermal aging. However, no thermal aging studies of 316 SS has shown the Fe_2P phase to form. In addition, Lee et al.(13) noted that a post-irradiation thermal anneal at the irradiation temperature of 675°C for 16 hours caused a partial dissolution of the Fe_2P phase which had formed under dual-ion irradiation conditions. In the present study, a 0.010" (0.04 mm) slice was taken from the nickel-plated 316 SS sample irradiated at 650°C and given a 24 hour post-irradi-

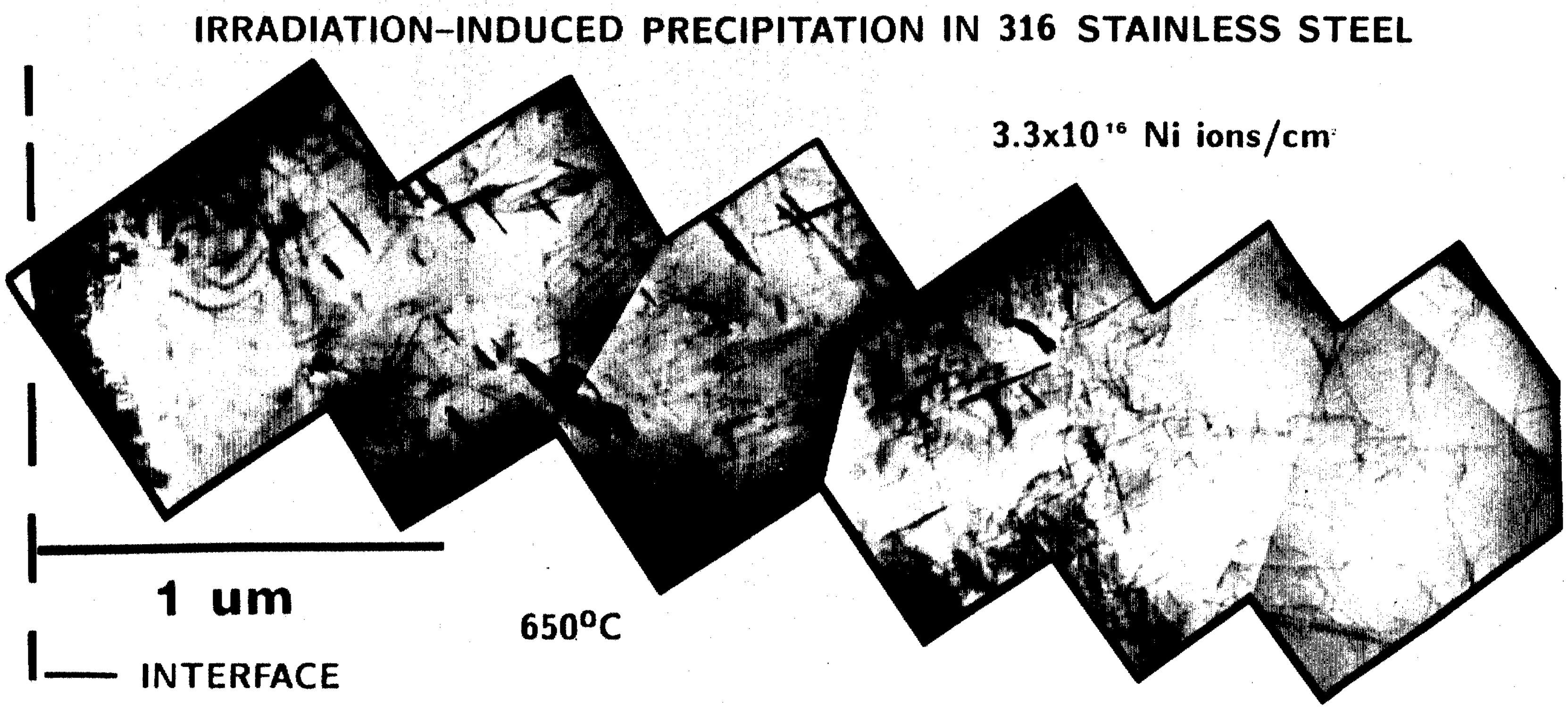

Fig. 5.25. Low-contrast micrographs of 316 SS irradiated to 10 dpa at 1 μm. Note the coarse Fe_2P needles (10-15 nm) throughout the damage range.

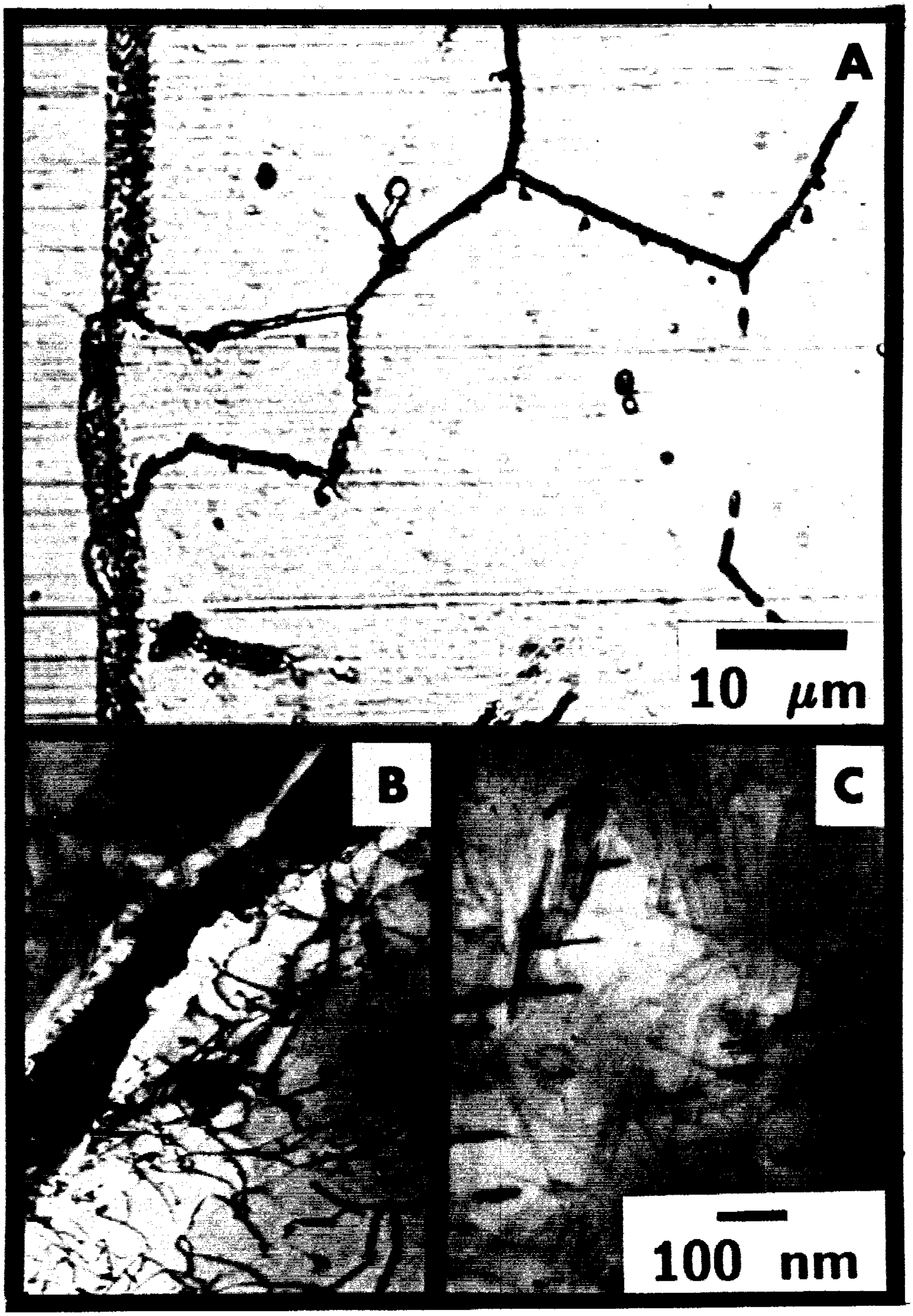

Fig. 5.26. Micrographs which illustrate the radiation-induced and thermally-induced precipitation in the 316 SS sample irradiated to 10 dpa (1 μm) at 650°C. (A) Optical of an etched cross-section specimen showing the 3 μm damage band and the grain boundary precipitation. (B) Grain boundary $M_{23}C_6$ in the control beyond the damage range. (C) Fe_2P needles at 1 μm depth.

ation anneal at 650°C. No needle-shaped precipitates were found to remain thus indicating a reversion of the Fe_2P into the austenite matrix. Thus, this phase is more properly labeled "radiation-induced" according to the convention suggested by Wilkes.(16) The post-irradiation anneal of the plated sample also induced the formation of cavities throughout the nickel plate. The very large H fugacities which are often observed(17) in cathodic charging experiments are assumed to cause the nickel-plate layer to be saturated with hydrogen which allows the formation of voids during the high temperature anneal.

B.3. Precipitation in Ion-Irradiated 316 SS

Table 5.4 reports the number density and average precipitate length over the 450-650°C temperature range. The precipitation over the 450-550°C range is characterized as small block or rod shaped, many of which formed on dislocation loops or segments. Stringers of precipitates were seen at both 500 and 550°C throughout the damage range. Van Aswegan(18) has reported stringer formation of carbide precipitates after quenching studies in stainless steel and he described a loop-punching mechanism for their formation.

No definite precipitate/matrix orientation relationship could be established for this 5-30 nm precipitation at 450-550°C. Selected area diffraction on some of the larger precipitates at 500°C has shown them to have an fcc crystal structure with lattice parameter 1 nm. In addition, in-situ EDS analysis has shown these precipitates to be rich in nickel and silicon as shown in Fig. 5.27. These

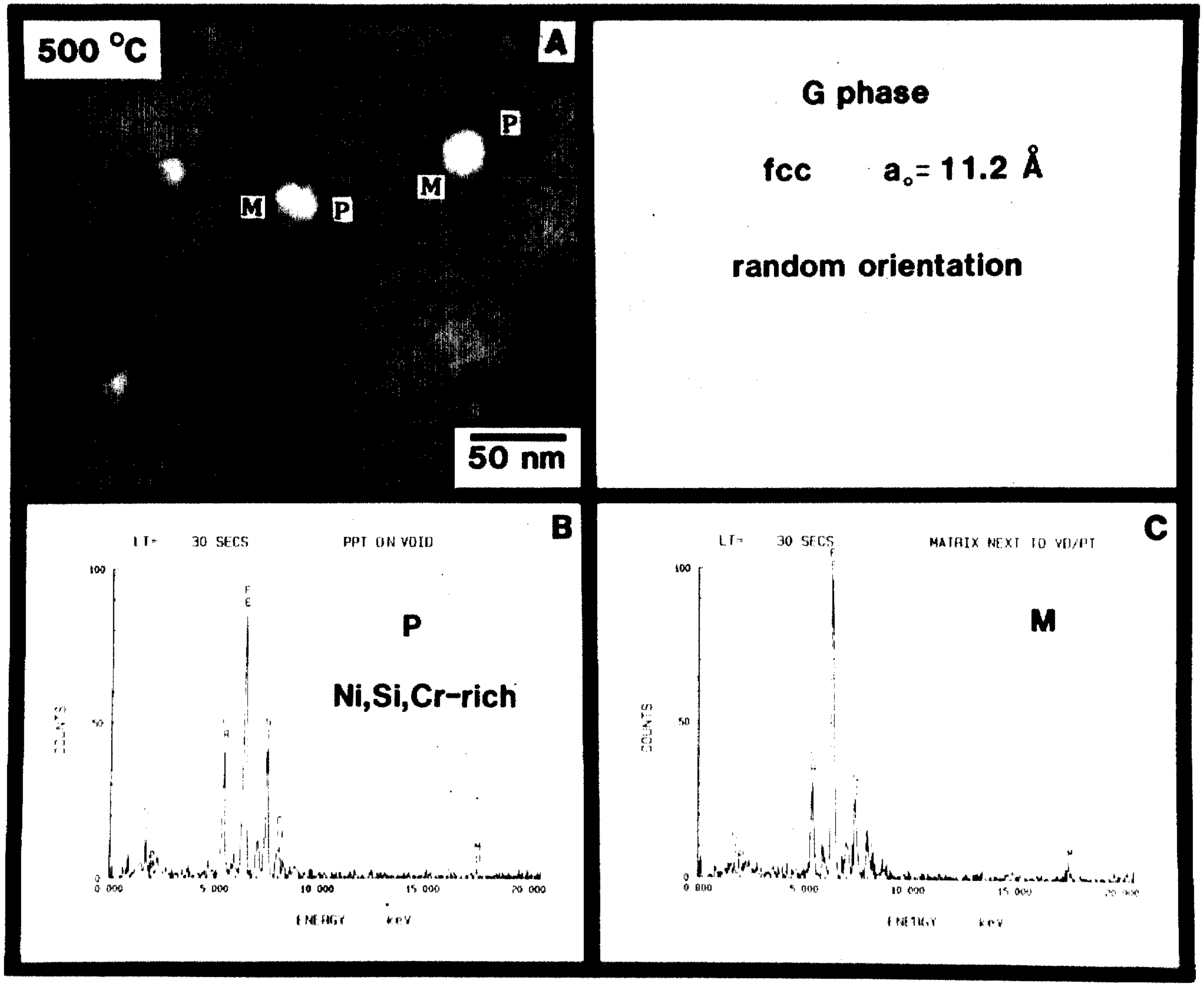

Fig. 5.27. (a) Bright field micrographs for a void/precipitate at 120 dpa, 500°C in 316 SS.
(b) EDS spectra at P illustrating the nickel and silicon enriched precipitate in (a).
(c) EDS spectra at M.

Table 5.4. Precipitation Parameters for Ion-Irradiated 316 SS

		$\bar{d}_{ppt}$ (nm)	N_{ppt} (10^{14} cm^{-3})
450°C	1 µm	6	50 ± 100%
	2.2 µm	8	50 ± 100%
500°C (10 dpa sample)	1 µm	9.2	11
	2.2 µm	16	6.5
500°C (30 dpa sample)	1 µm	10	9.5
	2.2 µm	18	7.0
550°C	1 µm	35	12
	2.2 µm	36	2.7
600°C (Fe_2P)	1 µm	54	9.9
	2.2 µm	58	12
650°C (Fe_2P)	1 µm	92	2.3
	2.2 µm	99	2.6

characteristics suggest that the larger precipitates in the 500 and 550°C samples are the G phase, a nickel silicide.(19)

As mentioned in Section B.2, the formation of the Fe_2P phase was the dominant microstructural feature in the 600-650°C irradiations. Figure 5.28 shows the EDS spectrum taken from an iron phosphide needle extracted on a plastic replica as described in Chapter 4,

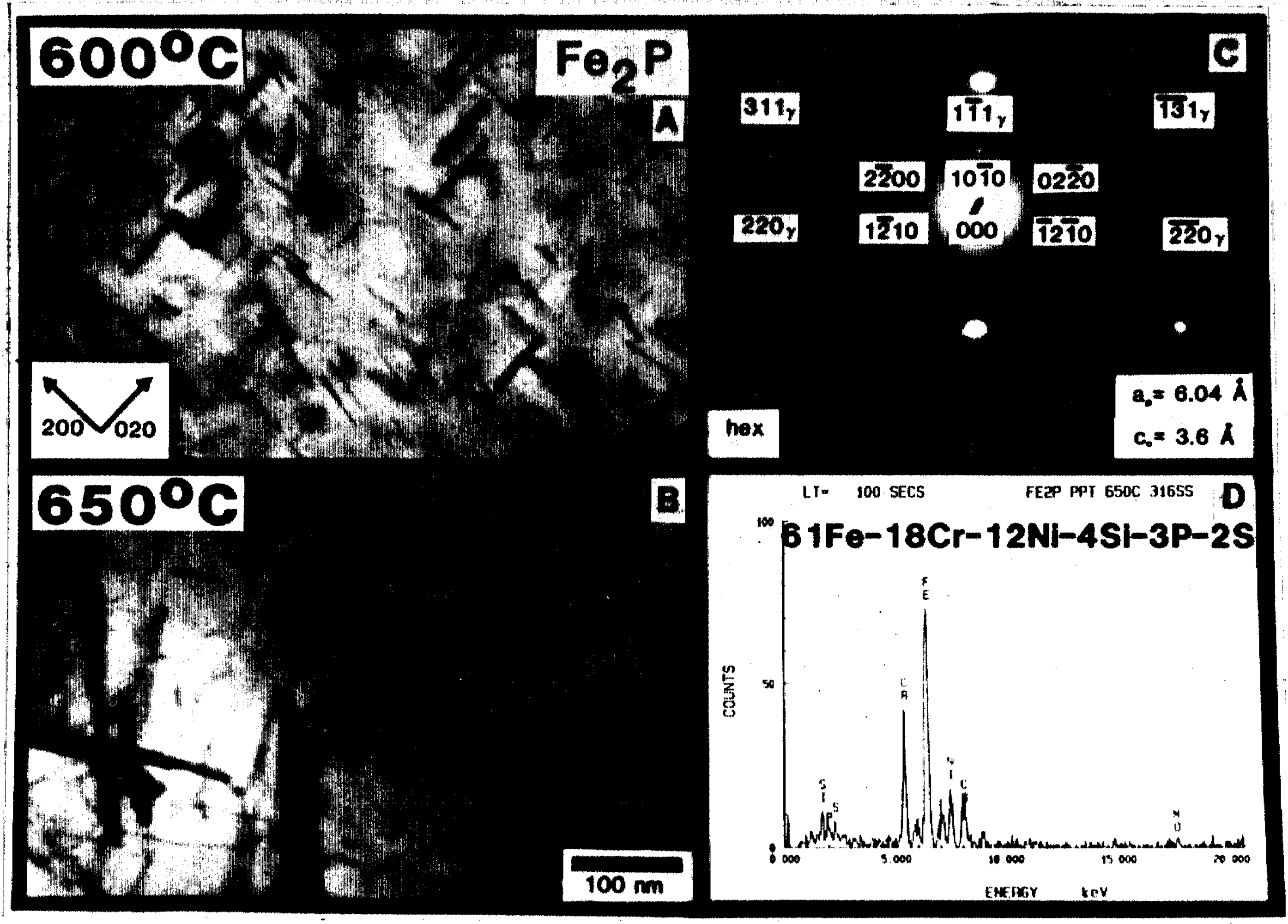

Fig. 5.28. (A & B) Fe$_2$P at 600 and 650°C in 316 SS. (C) Diffraction pattern from precipitates in (B) identifying the hexagonal Fe$_2$P phase. (D) EDS spectrum from the extracted Fe$_2$P needles.

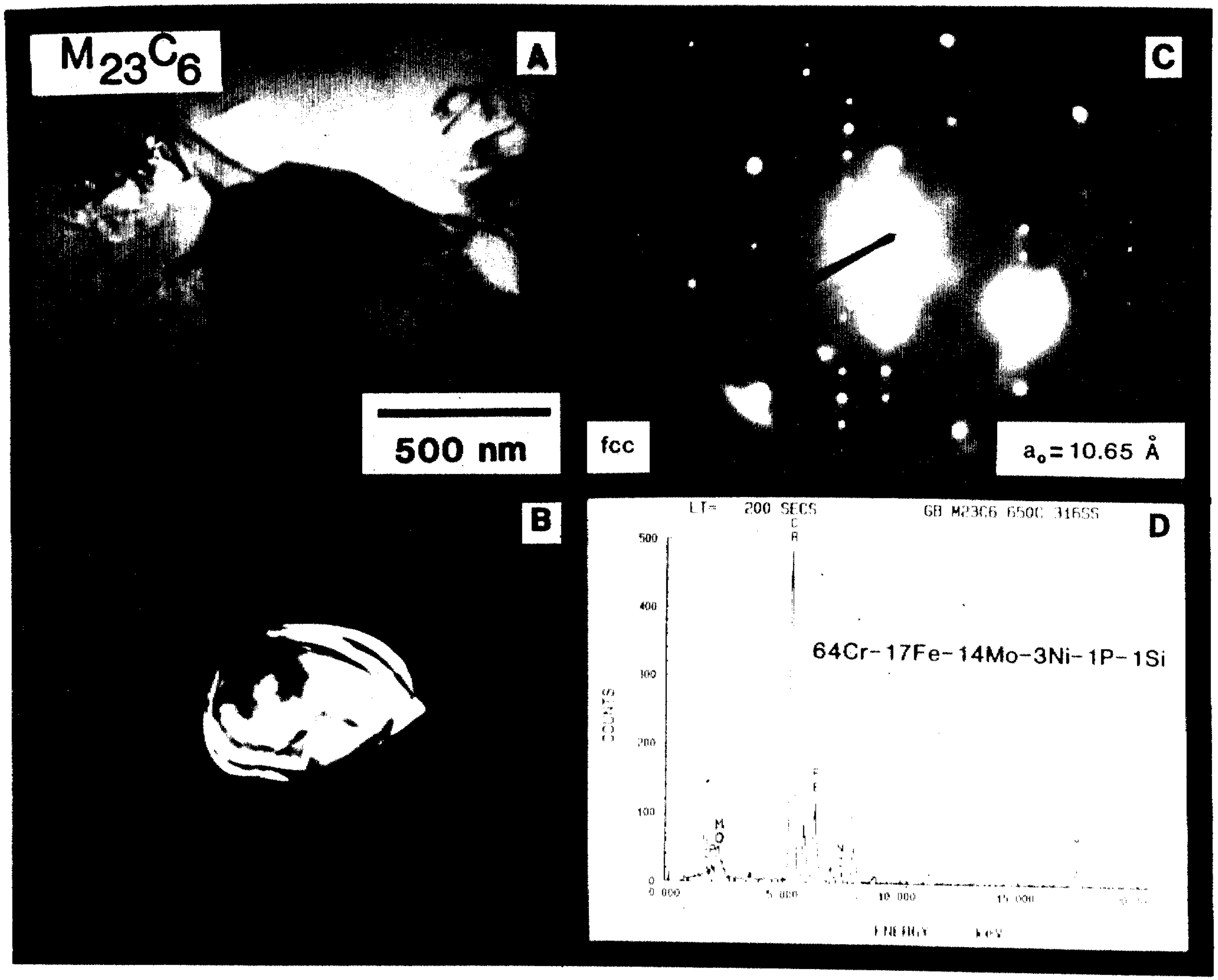

Fig. 5.29. (A & B) Bright and dark field of $M_{23}C_6$ thermally-induced precipitate at 650°C. (C) SAD pattern of $M_{23}C_6$. (D) EDS spectrum from an extracted $M_{23}C_6$ precipitate.

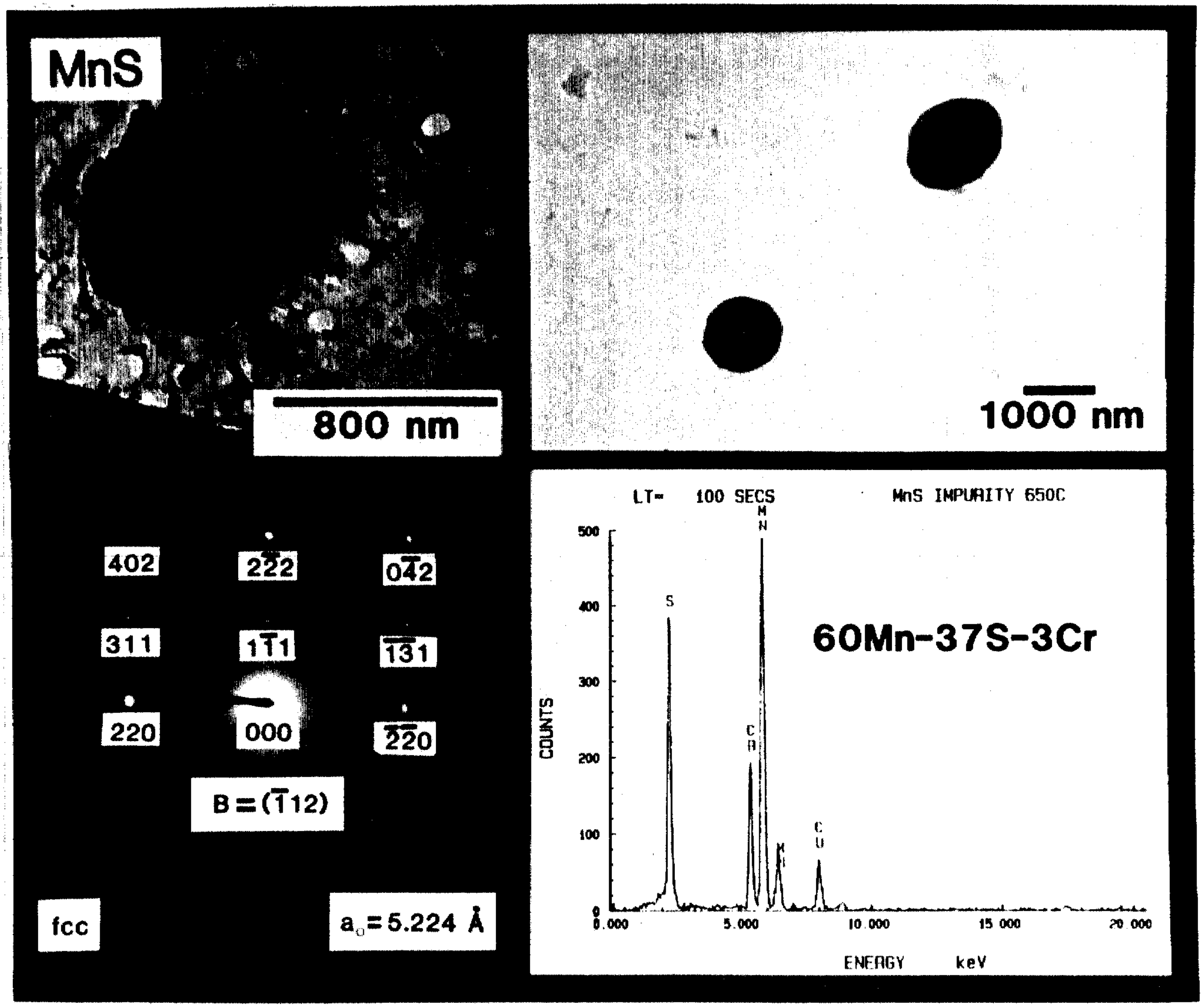

Fig. 5.30. Extracted MnS impurity precipitates (micrographs at top) in unirradiated region (thermally aged) 316 SS at 650°C.

Section C.4. It is seen that this phase is enriched in Si, P and S compared to the matrix composition levels.

The grain boundary $M_{23}C_6$, formed under the thermal anneal during irradiation at 650°C, was extracted from the matrix and yielded the composition (Fig. 5.29) similar to that reported by Maziasz.(20) Lastly, an impurity phase, MnS, was observed (with density ~ 10^{13} cm^{-3}) in the unirradiated matrix region of the 650°C sample. Figure 5.30 shows the EDS spectrum of the extracted MnS precipitate.

References for Chapter 5

1. J.B. Whitley, Ph.D. Thesis, University of Wisconsin, Madison, Wisconsin, 1978.
2. D.B. Bullen, Ph.D. Thesis, University of Wisconsin, Madison, Wisconsin, 1984.
3. H. Attaya, Ph.D. Thesis, University of Wisconsin, Madison, Wisconsin, 1980.
4. A.D. Brailsford and L.K. Mansur, J. Nucl. Mat. 71 (1977) 110.
5. D.L. Plumton and W.G. Wolfer, J. Nucl. Mat. 120 (1984).
6. D.L. Plumton, H. Attaya and W.G. Wolfer, J. Nucl. Mat. 122 & 123 (1984) 650.
7. N.H. Packan and K. Farrell, Nuclear Tech./Fusion 3 (May 1983) 392-404.
8. F.A. Garner and L.E. Thomas, "Effects of Radiation on Substructure and Mechanical Properties of Metals and Alloys," ASTM STP 529 (1973) 303-325.
9. W.J. Weber, Ph.D. Thesis, University of Wisconsin, Madison, Wisconsin, 1977.
10. E. Fromm and E. Gebhardt, Gase und Kohlenstoff in Metallen, (Reine und angewandt Metallkunde in Einzeldarstellungen; Bd. 26), Springer-Verlag, Berlin/Heidelberg (1976), p. 583.

11. N.H. Packan and K. Farrell, in "Effects of Radiation on Materials: Eleventh Conference," ASTM STP-782 (1982) 885-894.

12. S. Wood et al., in "Effects of Radiation on Materials: Tenth Conference," ASTM STP 725 (1981) 455-469.

13. E.H. Lee, L.K. Mansur and A.F. Rowcliffe, J. Nucl. Mater. 122 & 123 (1984) 299-304.

14. E.H. Lee, P.J. Maziasz and A.F. Rowcliffe, in Phase Stability During Irradiation, The Metallurgical Society of AIME, J.R. Holland, L.K. Mansur and D.I. Potter, eds., pp. 191-218.

15. J. Bentley and J.M. Leitnaker, in The Metal Science of Stainless Steels, Proceedings of the symposium on the 107th AIME Annual Meeting (1978), Eds. E.W. Collings and H.W. King, The Metallurgical Society of AIME, pp. 70-91.

16. P. Wilkes, J. Nucl. Mater. 83 (1979) 166-175.

17. L. Nanis, "Chemical and Electrochemical Factors Affecting Hydrogen Absorption in Metals," Symposium on the Environment Sensitive Fracture of Engineering Materials, TMS-AIME, October 1977, Z.A. Foroulis, ed.

18. J.S.T. Van Aswegan, R.W.K. Honeycombe and D.H. Warrington, Acta Met. 12 (1964) 1-13.

19. W.J.S. Yang, H.R. Brager and F.A. Garner, in Phase Stability During Irradiation, L.K. Mansur and D.I. Potter, Eds., (1980) 257-269.

20. P.J. Maziasz, Scripta Met. 13 (1979) 621-626.

CHAPTER 6. DISCUSSION

A. Effect of Impurities on Void Swelling

The most significant observation of the response of 316 SS and the P7 alloy to heavy-ion irradiation is the copious void formation in the P7 alloy over its entire temperature range of irradiation compared to the heterogeneous void formation which occurred in 316 SS over a more limited temperature range. The differences in the impurity content in these otherwise similar alloys most likely leads to the widely different response to irradiation. Recall that the P7 alloy contains significantly higher oxygen and lower carbon, silicon, phosphorous and sulphur levels than the MFE heat of 316 SS (Tables 4.1-4.3).

Increased carbon in solution has been observed to reduce the peak temperature swelling level in ion-irradiated alloys.(1-4) Gessel and Rowcliffe(1) have reported a decrease in swelling at 675°C from 50% to 10% with the addition of 0.4 wt.% C to a Fe-7.5 Cr-20 Ni ternary austenitic stainless steel alloy ion-irradiated to 170 dpa. Makin(2) and Williams(3) have observed similar effects in ion-irradiated 316 SS. Bates and Johnson,(5) however, observed a slight increase in swelling with carbon content in an ion-irradiated Fe-15 Cr-20 Ni ternary at 675°C. These studies made no mention of any carbide precipitation response which would reduce the carbon in solution. Although the level of swelling seems to be reduced with the soluble carbon content, no shift in the temperature peak of swelling has been observed thus far.(1,2)

These results may be described in terms of the void growth model with solute trapping (discussed in Section 2.A.3). The model considers the effects of interstitial and vacancy trapping by solute atoms. This trapping is characterized by a certain binding energy, E^B, for either vacancies or interstitials and leads to a lower free defect population. Since only mobile vacancies can increase the void size, vacancy trapping effectively decreases the void growth rate.

Silicon has been shown to suppress void nucleation during fast neutron irradiation.(6) Silicon has also been reported to significantly reduce void swelling and create a downward "shift" in the peak temperature of swelling by suppression of high temperature swelling(1,5) in ion studies. Makin,(2) however, did not observe any shift in the temperature dependence of swelling in ion-irradiated 316 SS with the silicon content from 0.04 to 0.4 wt.%.

Garner and Wolfer(7) have suggested that silicon, a fast diffuser in Fe-Cr-Ni alloys, acts to reduce void nucleation, particularly at higher temperatures, by increasing D^v_{eff}, the effective vacancy diffusivity of the host metal. This increase in D^v_{eff} is a result of an increase in the diffusivities of all components of Fe-Ni-Cr alloys.(8-10) Thus, since the flux of radiation-produced vacancies, $D_v^{eff}C_v$ is a constant, the increase in D_v^{eff} reduces the concentration C_v of radiation-produced vacancies and thereby reduces the vacancy supersaturation.

Phosphorous also is a fast-diffusing element in iron-based austenitic alloys(11) and it will increase the diffusivity of nickel(12) and chromium(13) in iron alloys. It has recently been shown that additions of phosphorous reduce the vacancy formation energy(14) in Fe-Cr-Ni alloys. This also will reduce the vacancy supersaturation of vacancies present during irradiation.(15)

Although most impurities present in 316 SS act to suppress void swelling, it is possible that the different swelling responses occurring in this study are influenced even more by the variations in gaseous nucleating agents in the two alloy matrices. It is this area that we will examine in more detail in the next section.

A.1 Effect of Oxygen on Void Swelling

Experimental studies have shown that oxygen is a potent agent for void nucleation. Ion-irradiation studies of copper,(16) nickel alloys,(2) vanadium(17) and niobium(18) have shown increased void formation and swelling with increasing oxygen content. Excessive amounts of oxygen can, however, reverse this trend and act to decrease the level of swelling in these alloys.(17,18)

The results in this thesis show void formation over the entire 400-650°C temperature range of the P7 alloy. In addition, outgassed samples of P7 with an estimated 30 appm oxygen (see Section 5.A.2) irradiated to 40 dpa at 650°C contained no visible voids. Thus, it is postulated that the high oxygen content (1000 appm) of P7 is responsible for its prolific swelling during irradiation at high temperatures.

If one compares the heat of solution of oxygen to the heat of chemisorption, one can obtain an indication of the tendency of free matrix oxygen to remain in solution or to be attracted to the clean, free surface of subcritical void embryos. Calculations using oxygen solubility data from Fromm and Gebhardt,(19) the heat of chemisorption equations of Tanaka and Tamaru,(20) and the heat of oxide formation of Fe_2O_3 from Robie et al.,(21) show that the heat of chemisorption of oxygen on γ-Fe (-272 kJ/mole oxygen at 650°C) is greater than the heat of solution of oxygen in γ-Fe (-93 kJ/mole oxygen at 650°C). Oxygen should therefore be attracted to free surfaces and thus, affect the surface energy of the cavities. According to Bernard and Lupis(22) the change in surface energy due to a surface coverage of oxygen, θ_o, on steel is given by

$$\Gamma - \Gamma(\theta_o) = \frac{kT}{A}\left[\frac{1}{2}\ln\frac{1}{1 - 2\theta_o} + \frac{2g\theta_o^2}{kT}\right] \tag{6.1}$$

where g corresponds to an interaction energy between neighboring adsorbed oxygen atoms and A is the area effectively occupied by a chemisorbed oxygen atom. Zinkle et al.(23) have recently demonstrated that, with a reduction in surface energy, the voids can become that most stable vacancy cluster in austenitic stainless steels.

The mobility of oxygen in the P7 alloy may be estimated from the diffusion equation for oxygen in γ-iron given in Ref. 24:

$$D = 5.75\exp\left(-\frac{40{,}300}{1.98\ T}\right)\frac{cm^2}{s}\ . \tag{6.2}$$

At 650°C, $\sqrt{Dt} \approx 3$ μm for t = 1 minute, and thus for a microstructure with no oxygen traps, oxygen will be readily mobile. This freely moving oxygen could be chemisorbed at vacancy clusters which form at the peak damage depth, thus promoting their stabilization and rapid growth while providing an even better sink for the oxygen. As the irradiation proceeds, additional void nucleation occurs throughout the damage range. This would explain the observed bimodal void size distribution at the damage peak in the P7 irradiated to 40 dpa.

A.2 Heterogeneous Void Formation

In contrast to the P7 results, limited void formation occurred in 316 SS from 450-550°C. The voids formed at precipitate interfaces or in conjunction with the nickel-rich precipitates (reported in Section 5.B.3). Figure 6.1 shows this void-precipitate association (void density $\approx 2 \times 10^{14}$ cm^{-3}) after a dose of 40 dpa at 500°C. It is not known whether the void formation preceded the associated precipitate formation or the voids formed at the preexisting precipitate-matrix interface. However, the precipitate number density exceeded that of the voids and the likely conclusion is that the precipitate formation did not require the presence of voids.

After a 4 MeV nickel-ion-irradiation of 316 SS at 650°C, Lee et al.(25) observed a void density of 7×10^{13} cm^{-3} which were <u>not</u> generally associated with precipitates. A swelling level of ~ 4.0% was observed after a dose of 100 dpa. The 316 SS specimens were prepared with a pre-irradiation electropolish and this step may have allowed

Fig. 6.1. Cavities attached to G-phase precipitates in 316 SS at 40 dpa. Note that the precipitate formation is not dependent on cavity formation.

oxygen to enter the specimen(26) and, as discussed in the previous section, promote void formation.

The results of the two 316 SS samples irradiated at 500°C do not show any increase in the void density (2×10^{14} cm^{-3}) and swelling level from 40 to 120 dpa. It is postulated that the free matrix oxygen in the 316 SS is insufficient to allow significant void formation to occur. The total oxygen content was measured at 160 appm and it is expected that the gettering action of silicon (12,000 appm) wt.%) will bind up most of this oxygen. In order for voids to nucleate with this low gas content, another mechanism to reduce the free energy barrier for void nucleation must be envisaged.

A significant reduction in the free energy of void formation is predicted to occur at a matrix-precipitate interface. Bates(27) has considered the variables associated with heterogeneous nucleation of voids on second phase precipitate surfaces. The model developed for such nucleation is based on the kinetic approach of Russell(28) who has shown that the free energy change for nucleation of a cluster of n vacancies, $\Delta G'_n$, can be written as (Section 2.A.2):

$$\frac{\Delta G'_n}{kT} = \sum_{j=0}^{n-1} \left[\ln \frac{\beta_i(j+1)}{\beta_v(j)} + \exp \frac{\delta G^o_j}{kT}\right] . \qquad (6.3)$$

Bates has derived the following expression for δG^o_n:

$$\delta G^o_n = -kT \ln \frac{C}{C_o} + \lambda[(n+1)^{2/3} - n^{2/3}] \qquad (6.4)$$

where the first term is the free energy term for the reduction of the vacancy supersaturation and the second term is the free energy term which accounts for the various surface energies involved and mechanical equilibrium at the cluster surfaces. The value of λ is given as:

$$\lambda = \pi^{1/3} \left(\frac{3\ \Omega}{8\ f(\theta)}\right)^{2/3} \left[(4 - 4 \cos \theta)\sigma_{vm} - (\sin^2\theta)\sigma_{mp}\right] \quad (6.5)$$

where: $f(\theta) = \dfrac{2 - 3 \cos \theta + \cos^3\theta}{4}$

and σ_{vp} = the free energy of the void-precipitate surface $\approx \sigma_{vm}$

σ_{vm} = the free energy of the void-matrix surface

σ_{mp} = interfacial free energy between the precipitate and matrix phase.

There is an additional mechanical equilibrium constraint of $\cos \theta = \sigma_{mp}/2\sigma_{vm}$, where θ is the contact angle between the nucleating cluster of vacancies and the matrix as shown in Fig. 6.2. It was shown(27) that a significant decrease in both the free energy of void formation and the number of vacancies in the critical nucleus will occur for a contact angle of 80° and $\sigma_{vm} \approx 1\ J/m^2$. It is also readily apparent from Eqs. (6.3)-(6.5) that a reduction in σ_{vm} will also enhance void nucleation.

This nucleation mechanism may cause the void formation observed at 450-550°C in the 316 SS. The precipitate densities are factors of 2 to 5 greater than the void distributions, thus they provide the nucleation sites for the observed void formation.

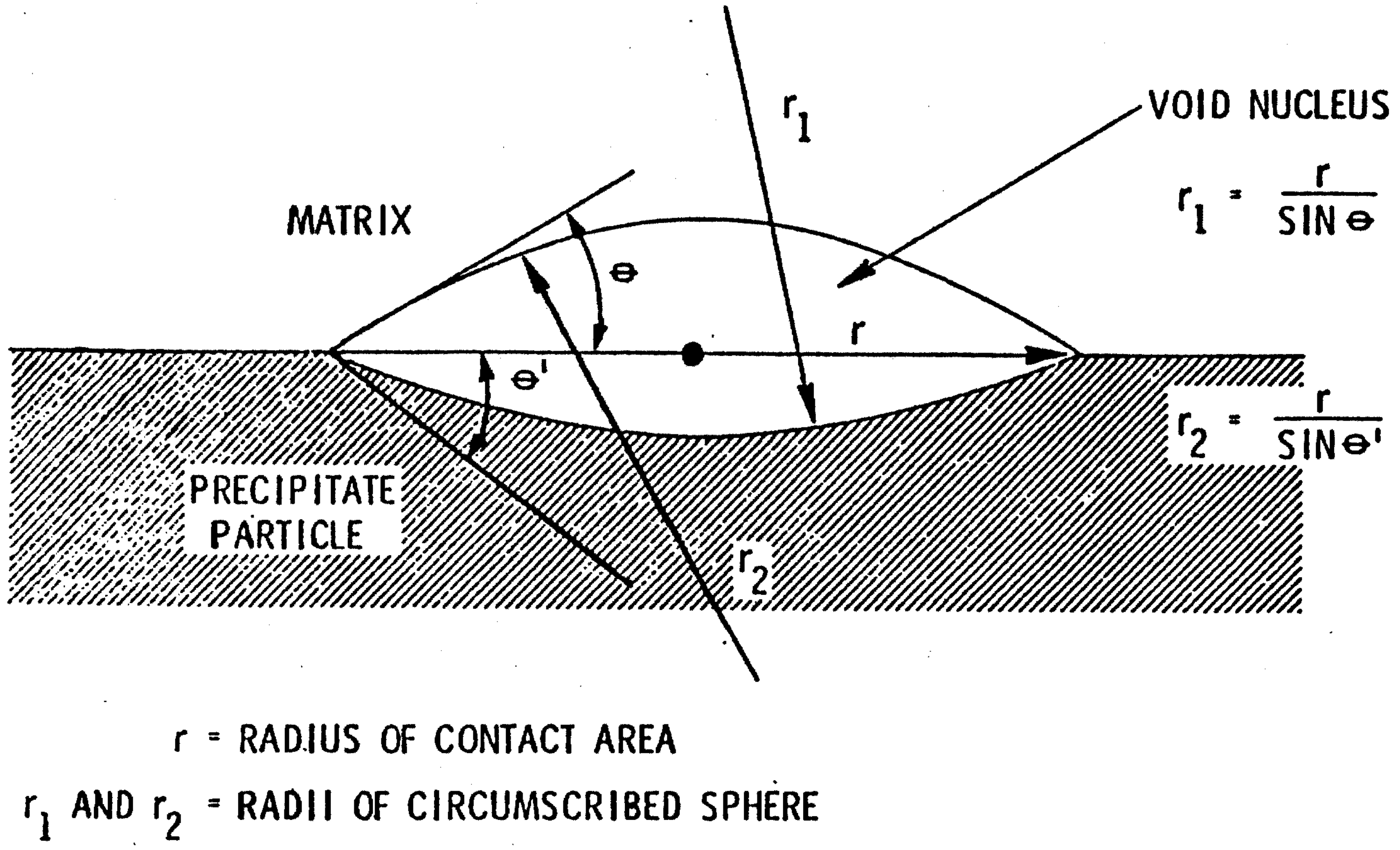

Fig. 6.2. Void nucleus at a precipitate-matrix interface. θ is the void-matrix contact angle.(27)

It is also observed (Fig. 6.1) that the voids nucleated at small precipitates. That is, small voids were observed with similarly sized precipitate shells. No small voids appeared at the interface of large precipitates. This allows the large contact angles predicted in the above model.

A.3 Temperature Dependence of Void Formation

The 316 SS void swelling results at 40 dpa in this study are plotted in Fig. 6.3 along with the void swelling data of Hudson.(29) In that study, 316 SS and 321 SS, whose compositions are given in Table 6.1, were preinjected with helium to 10 appm and irradiated to 40 dpa at a rate of 1-3 x 10^{-3} dpa/s with 46.5 MeV nickel ions. Data for the swelling curves plotted in Fig. 6.3 were taken from the peak damage region in each study (at ≈ 2 μm in this study, 4.5 μm in the Hudson study). The displacement rates were similar (≈ 3 x 10^{-3} dpa/s) and damage gradient effects were precluded by data acquisition at a given depth, i.e. dose (in this case, 40 dpa). It may be argued that void data extracted in the damage peak is influenced by the injected ion species (see Section 6.B). However, results from the irradiation of the P7 alloy in this study show that suppression of void nucleation and growth is significant only at temperatures < 500°C. The absence of voids at 600 and 650°C in this present study cannot be ascribed to injected interstitial effects. In addition to the large difference in the amount of swelling, a "shift" in excess of 100°C between the peak swelling temperatures is noted for this common dose swelling plot. This "shift" is actually a lack of void formation at

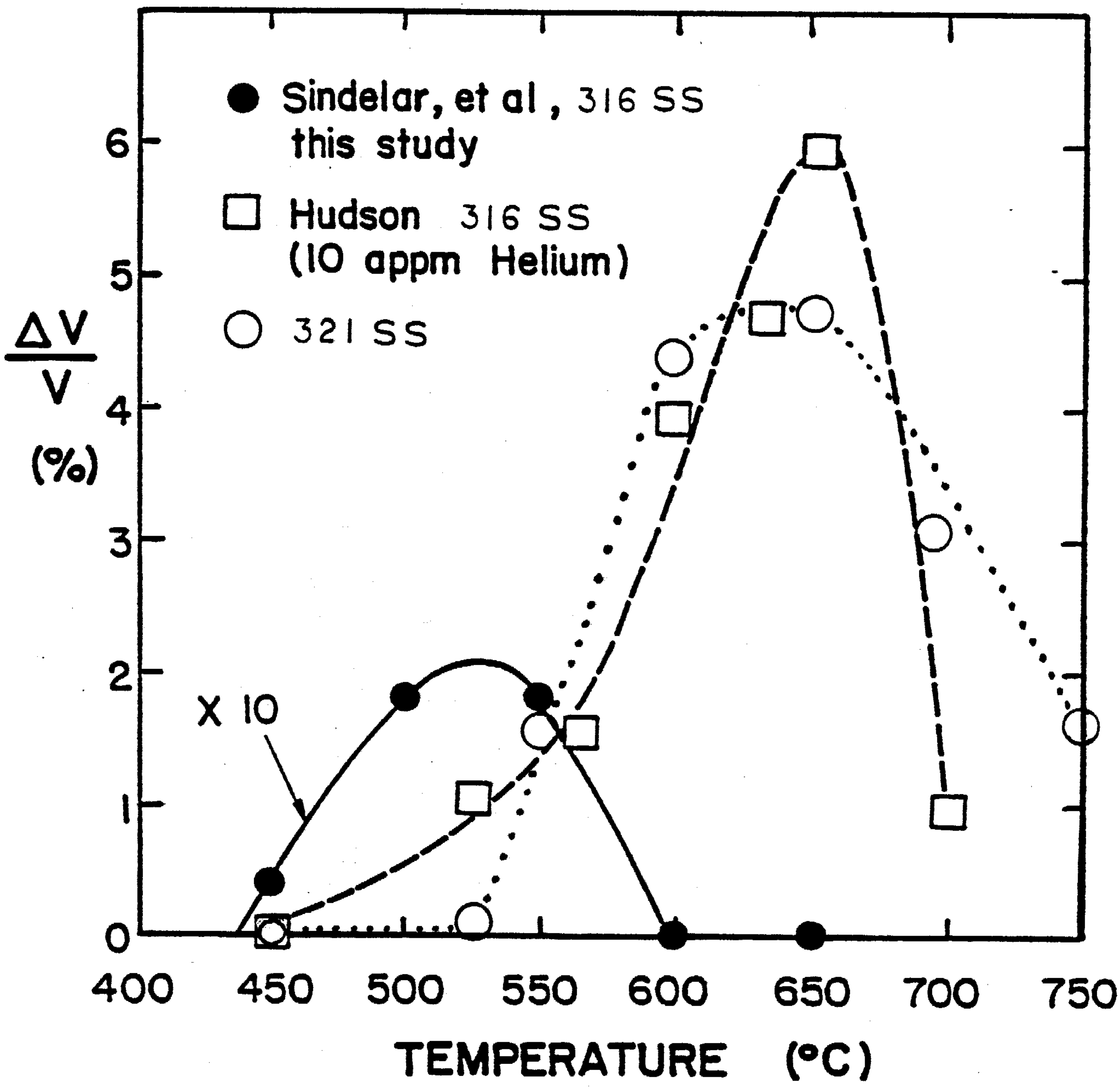

Fig. 6.3. Swelling curve for Ni-ion irradiated 316 SS to a common 40 dpa dose without He (this study) and preinjected to 10 appm He (Hudson(29)).

Table 6.1. Composition of the MFE Heat (#15893) 316 SS, the P7 Alloy, the Firth-Vickers 555 316 SS, and the En588 321 SS in wt.%. The Oxygen and Nitrogen Contents Were Determined by Inert-Gas Fusion Analysis

MFE 316 SS

Cr	Ni	Mo	Mn	Si	C	P	S	Ti	O	N	Fe
17.4	12.6	2.2	1.81	0.65	0.05	0.030	0.020	<0.001	0.005	0.046	Bal.

Firth Vickers 555 316 SS[(a)]

Cr	Ni	Mo	Mn	Si	C	P	S	Ti	O	N	Fe
17.5	11.8	2.5	1.1	0.3	0.03					0.023	Bal.

En588 321 SS[(a)]

Cr	Ni	Mo	Mn	Si	C	P	S	Ti	O	N	Fe
18.1	9.57		1.76	0.42	0.05	0.025	0.03	0.33			Bal.

P7 Alloy

Cr	Ni	Mo	Mn	Si	C	P	S	Ti	O	N	Fe
17	16.7	2.5	0.03	0.1	0.005			0.01	0.03	0.004	Bal.

(a) Used by Hudson(29)

600 and 650°C in this present study which is attributed to the absence of helium as a nucleating agent.(30) Studies of the effect of impurity content on void swelling do not show peak temperature shifts much greater than 50°C.(1) Thus, the differences in the level of impurities between the two heats of 316 SS alone would not account for the large (> 100°C) temperature "shift" in peak swelling. In addition, Hudson found no difference in the peak swelling temperatures for the 316 SS and 321 SS which vary in impurity content (Table 6.1).

Farrell and Packan(31) have reported a helium-induced upward shift in the temperature dependence of swelling in the P7 alloy. They determined the peak swelling temperature for 4 MeV Ni single-ion-irradiated P7 to be approximately 670°C, which agrees with the results of this study (see Fig. 5.7). This temperature is ≈ 125°C higher than the peak swelling temperature found for 316 SS in this study (see Fig. 6.3). Makin(2) has found no difference in the peak swelling temperatures between ion-irradiated 316 L (with 0.01 C, 0.04 Si), 316 M (0.06 C, 0.36 Si), and 316 H (0.2 C, 0.4 Si). Thus the difference in peak swelling temperatures between the 316 SS and the P7 alloy might be attributed to an oxygen-induced shift in the temperature dependence of swelling. A study wherein a controlled oxygen content is present in 316 SS would be needed to confirm this speculation.

B. Effects of the Injected Interstitials

Results from the irradiation of P7 at temperatures from 400 to 500°C show a marked decrease in void number density and size occurring at depths corresponding to the range of the bombarding nickel for samples. No apparent suppression was observed in samples irradiated at 550 and 650°C.

Suppression of the growth rate of voids due to the influence of the injected interstitials (bombarding ions) was first postulated by Brailsford and Mansur.(32) They concluded that a significant decrease in the void growth rate occurs at low irradiation temperatures, where recombination is the most likely fate of point defects. Mansur and Yoo(33) have considered the effect of injected interstitials on the void growth rate as a function of bias, sink strength and vacancy migration energy. Figure 6.4a,b depicts a large decrease in the void growth rate associated with an alloy with a low bias, low sink strength, and high vacancy migration energy. Current estimates of the net bias of 80 to 120%(34) along with a vacancy migration energy, E_m^v, of 1.1 eV,(35) result in a negligible effect on the void growth for a moderate sink strength of 4×10^{10} cm^{-2}. Garner(36) states that the theory may have to be recalibrated and/or expanded to account for the experimental observations which imply that the bias and sink strengths are high for a 1%/dpa rate.

Brailsford and Mansur(32) have shown that swelling saturation will ultimately occur in ion-irradiated alloys at the level corresponding to

$$4\pi r_v C_v/\rho_d = g/\varepsilon_i \qquad (6.5)$$

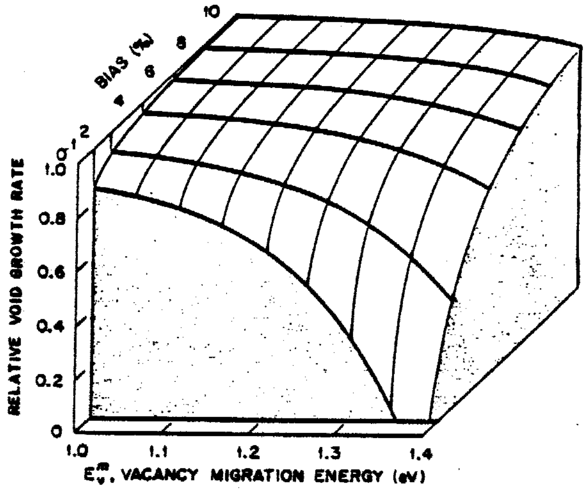

Fig. 6.4a. Relative void growth rate (with injected interstitials) as a function of E_v^m, and bias.(33)

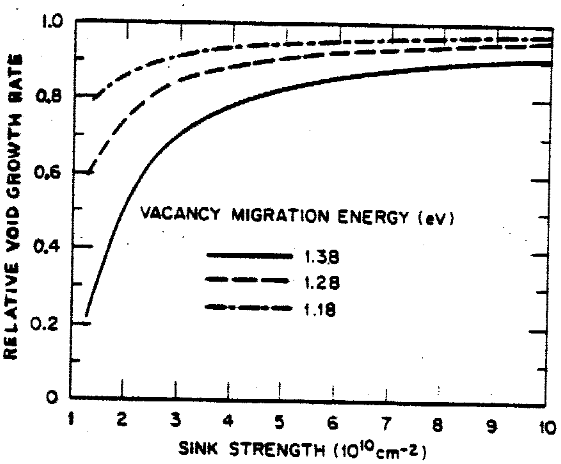

Fig. 6.4b. Relative void growth rate (with injected interstitials) as a function of E_v^m and sink strength.(33)

where r_v is the void radius, C_v the void concentration, ρ_d the dislocation density, and ε_i is the excess interstitial fraction, taken as the ratio of deposited ions to the interstitials produced by damage that survive cascade recombination and g is related to the net bias of the microstructure. The level of swelling at which saturation occurs can be written as:(32)

$$S_m = \frac{1}{3} \frac{(g\rho_d/\varepsilon_i)^3}{(4\pi C_v)^2} . \tag{6.6}$$

With ε_i chosen as 10^{-3}(37) and g chosen as 0.8,(34) Eq. (6.6) predicts that an extremely large saturation level of swelling (500%) will occur for the dislocation ($> 3 \times 10^{10}$ cm^{-2}) and cavity (10^{14}-10^{16} cm^{-3}) densities which occur in the ion-irradiated P7. With a net bias of $g = 0.01$, $\rho_d = 5 \times 10^9$ cm^{-2}, and $C_v = 2 \times 10^{15}$ cm^{-3}, Brailsford and Mansur predicted a saturation of swelling at 7% in ion-irradiated nickel. Nickel has been observed to exhibit swelling saturation near this level during ion-irradiation.(38-40) The results of the high fluence irradiations of P7 at 650°C do not show a saturation in swelling at doses of 100 dpa and swelling levels of 35%, consistent with the above prediction.

The effect of the injected interstitials on cavity nucleation has been modeled by Plumton and Wolfer.(41) Their treatment, based on the void nucleation theory of Si-Ahmed and Wolfer,(42) predicts that the suppression of void nucleation will be stronger at low irradiation temperatures, where recombination of point defects is an important process. Strong suppression effects with this trend have been observed in nickel by Whitley(39) and Bullen.(43) Nucleation suppression is characterized by a decrease in the cavity number density at depths which correspond to the range of the injected ions.

Good qualitative agreement of the temperature-dependent response to the depth-dependent nucleation calculations can be seen in Fig. 6.5. The strong suppression of nucleation at 400 and 500°C is in agreement with the decreased cavity density measurements at the ≈ 2 μm depth. At 550°C, no characteristic "dip" in the nucleation rate at the ion range depths is predicted; however, the predicted nucleation rate is a factor of 10 to 100 less with the injected interstitials than without the injected interstitials. It is noted experimentally that the peak void density at 550°C occurs at the damage peak and thus no apparent suppression of nucleation has occurred. It can be concluded that suppression of nucleation due to enhanced recombination is not significant at temperatures > 550°C. Void nucleation at 650°C is predicted to be extremely difficult, factors of 10^5 to 10^7 below 550°C. A reduction in surface energy to 0.1 J/m^2 yields a nucleation rate at 650°C which corresponds to the measured cavity number density.(37) Although this value is unrealistically low, the high oxygen content in the P7 is predicted to stabilize voids at this temperature through a significant reduction in the surface energy of three-dimensional vacancy clusters (see Section 6.A.1).

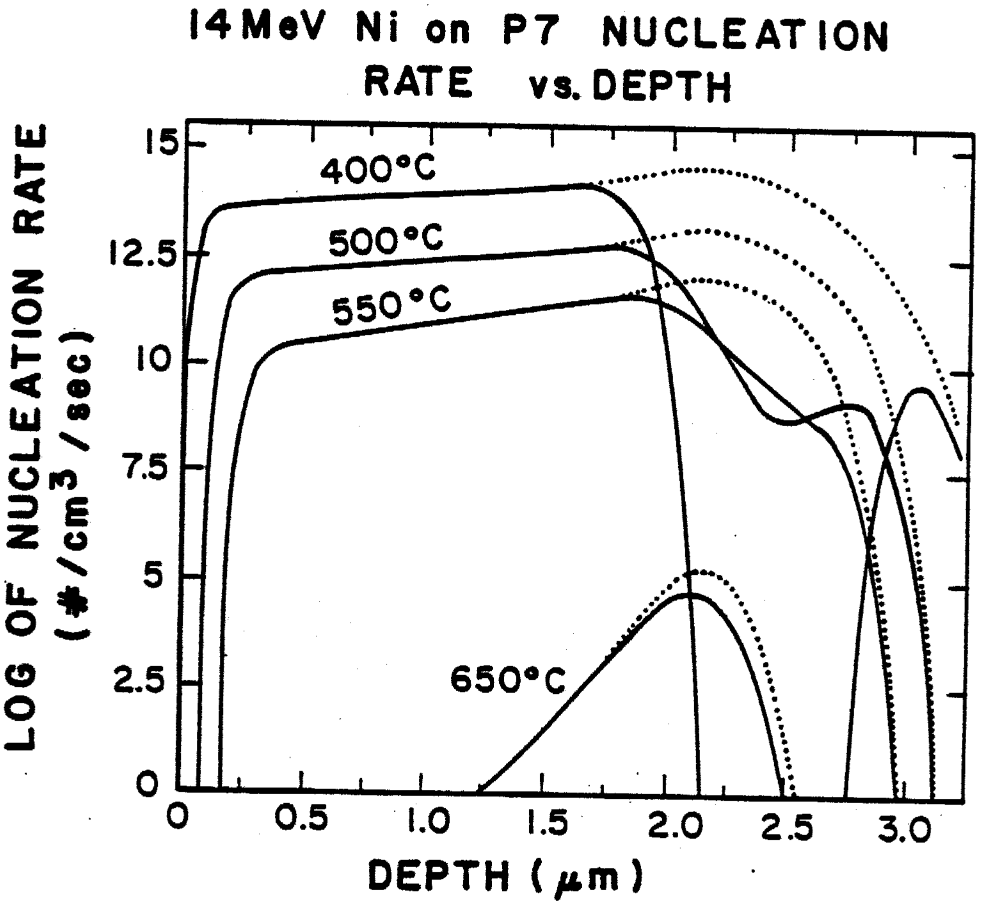

Fig. 6.5. Depth-dependent steady state void nucleation rate as a function of irradiation temperature. The dashed curves represent the nucleation rate in the absence of the injected ions (calculations courtesy of D.L. Plumton).

C. Swelling Rates of Austenitic Stainless Steels

C.1 Heavy-ion Swelling Rates of P7 and 316 SS

The parameters of the P7 samples irradiated to four fluence levels at 650°C are given in Table 6.2. Figure 6.6 displays the evolution of the swelling profile by a series of micrographs of three of the P7 samples.

The dpa values in Table 6.2 correspond to dose levels at the 1 μm depth and the 2-2.2 μm peak damage depth given by Fig. 6.7. Figure 6.7 is only valid for void-free material, however, and the damage model must account for cavitation in the high-swelling P7 alloy to obtain the time-dependent damage profile. First-order corrections (see Section C.4) are applied to these samples by assuming the peak swelling value occurs at the peak displacement level, as indicated in Fig. 6.7.

The swelling data from the 1 μm and peak swelling depths with the corresponding dpa values given in Table 6.1 are used to construct the swelling curve in Fig. 6.8. It is seen that a constant swelling rate approaching 0.4%/dpa is obtained when using data from the 1 μm depth as well as data from the swelling peak.

Previous irradiations of P7 with 5 MeV nickel ions at 625°C(44) and 4 MeV nickel ions at 635°C(45) used step height techniques(46) to determine the swelling as a function of displacement dose up to peak dose levels of 300 dpa. It can be seen in Fig. 6.9 that the swelling rate approaches 0.45%/dpa. Irradiations with 4 MeV nickel ions(40,47-49) have also yielded swelling rate of 0.3-0.4%/dpa at

Table 6.2. Parameters for a 14-MeV Ni-Ion Irradiation of P7

Displacement Efficiency K = 0.8, E_d = 40 eV, T_{irr} = 650°C

dpa at 1 μm	Peak dpa	Fluence (ions/cm^2)
2.3	20	0.8×10^{16}
10	40	3.3×10^{16}
17*	68*	5.6×10^{16} *
25	100	8.3×10^{16}

*Damage rate at 1 μm from surface is 1.6×10^{-3} dpa/s, at the peak it is 6.4×10^{-3} dpa/s; the other samples were irradiated at 0.8×10^{-3} dpa/s at 1 μm and 3.2×10^{-3} dpa/s at the peak damage region.

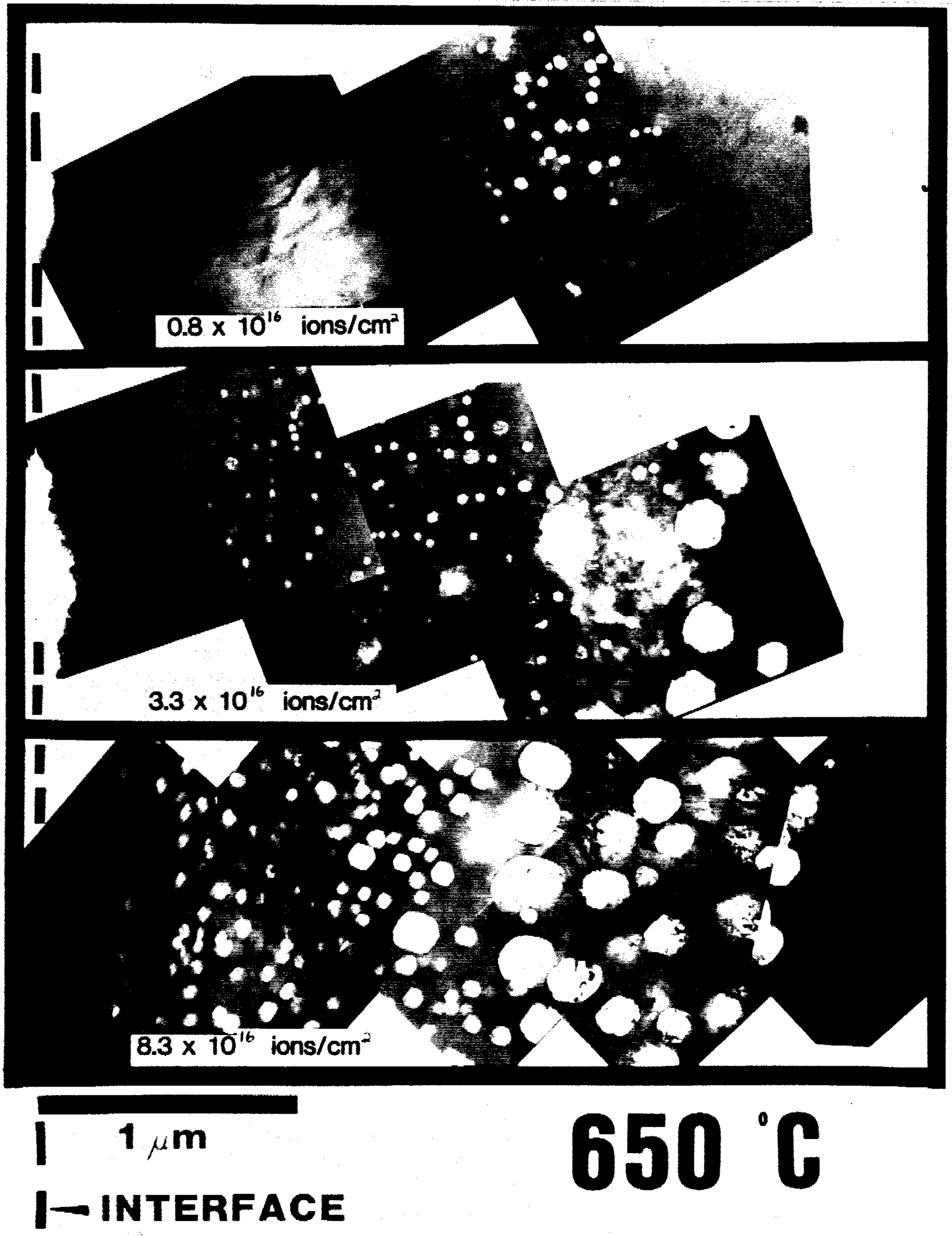

Fig. 6.6. Depth-dependent swelling in P7 irradiated to 2.3, 10 and 25 dpa at 1 μm.

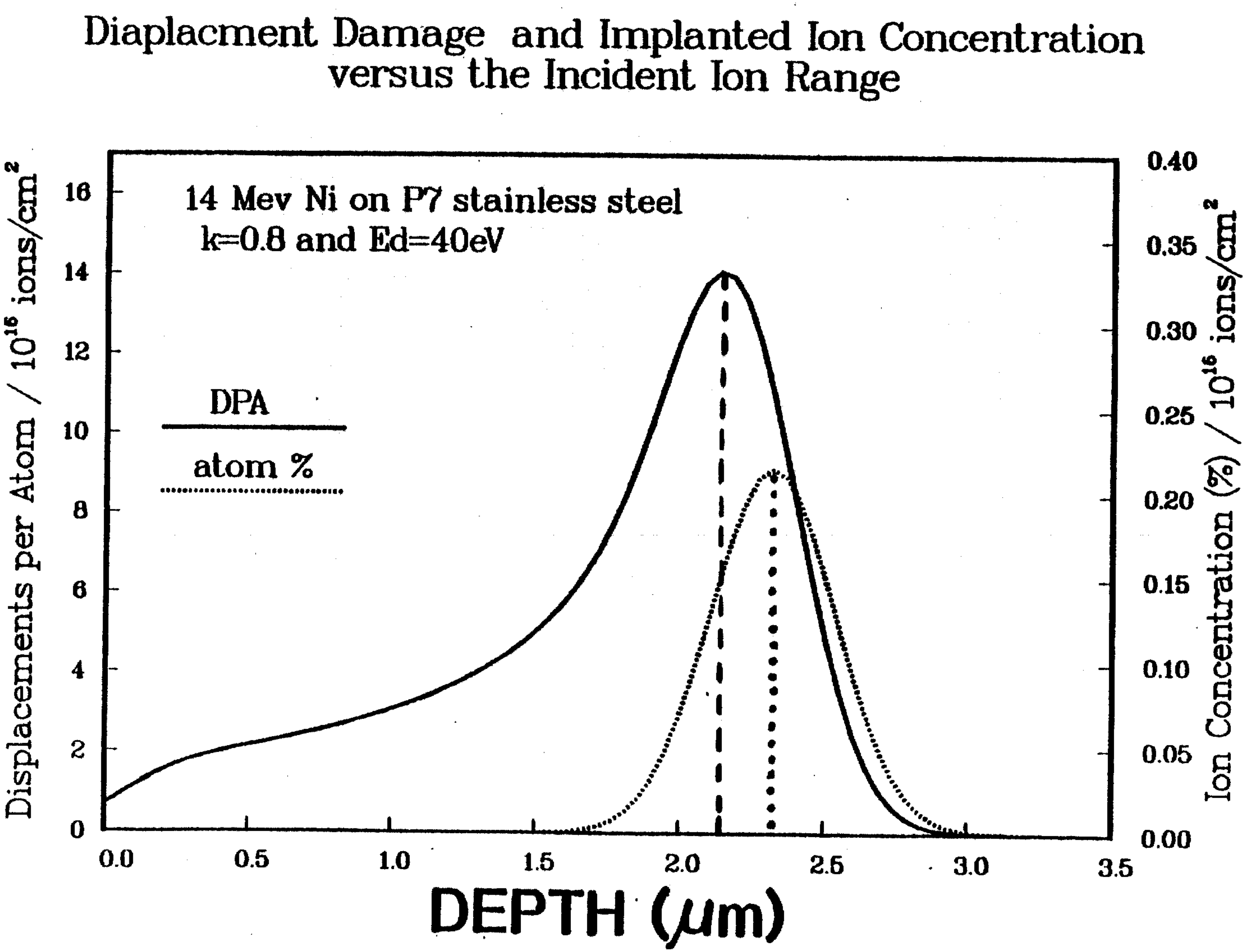

Fig. 6.7. Depth-dependent displacement damage in void-free P7.

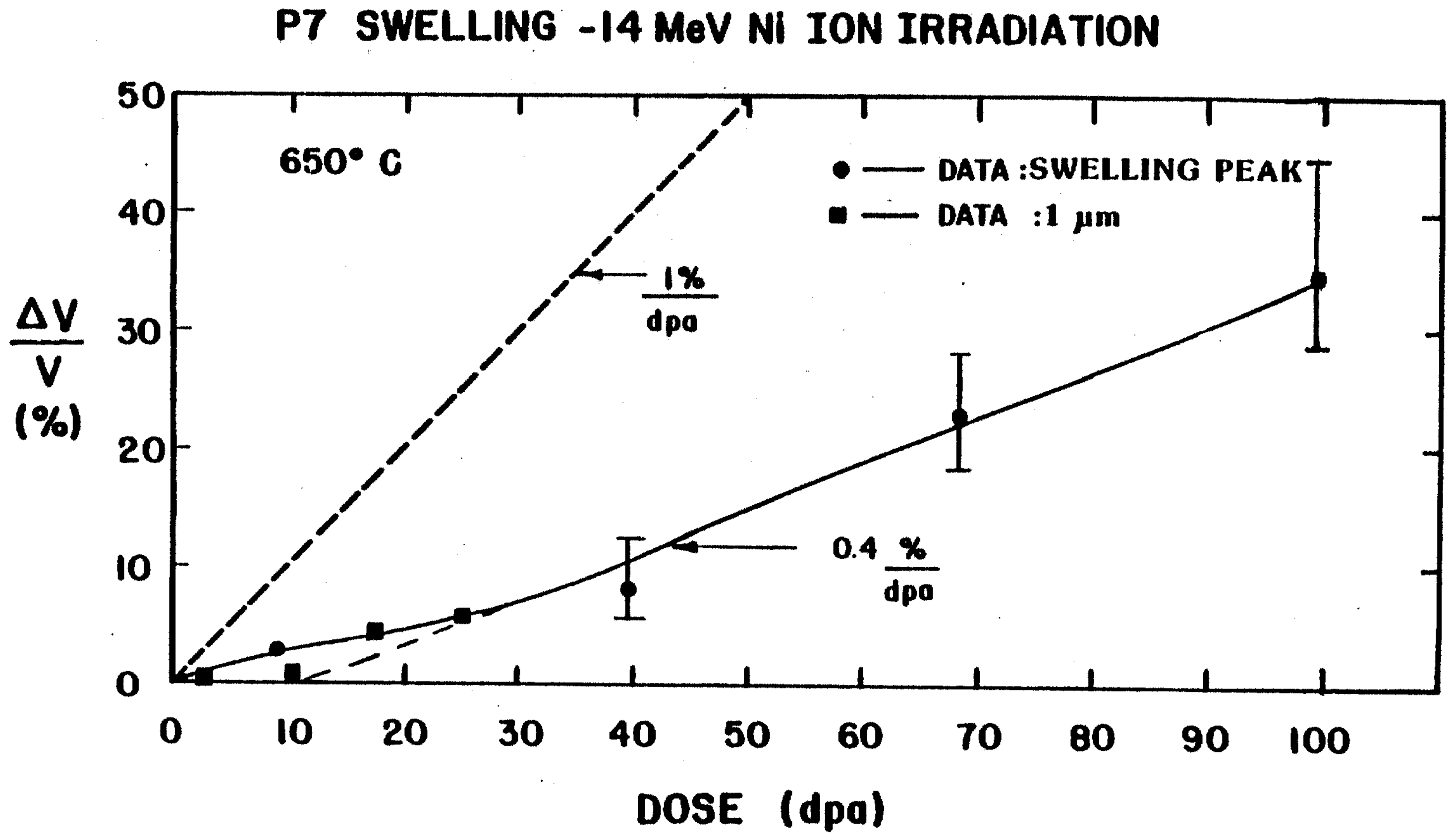

Fig. 6.8. Swelling vs. dose in 14 MeV ion-irradiated P7 alloy. First-order corrections to the dose are applied at the peak swelling depth. See text.

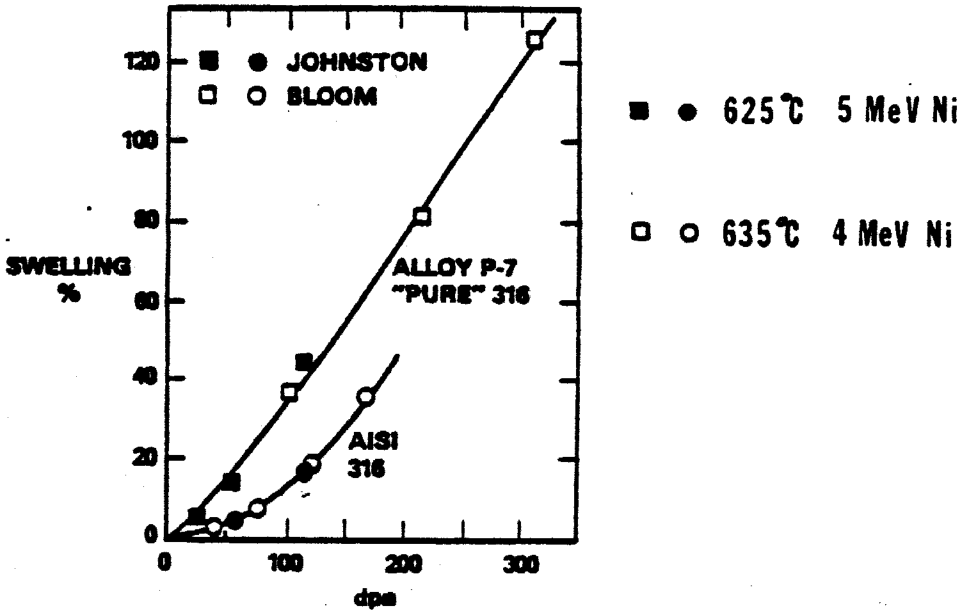

Fig. 6.9. Determinations of swelling as a function of composition in nickel-ion-irradiated Fe-Ni-Cr alloys.(44,45)

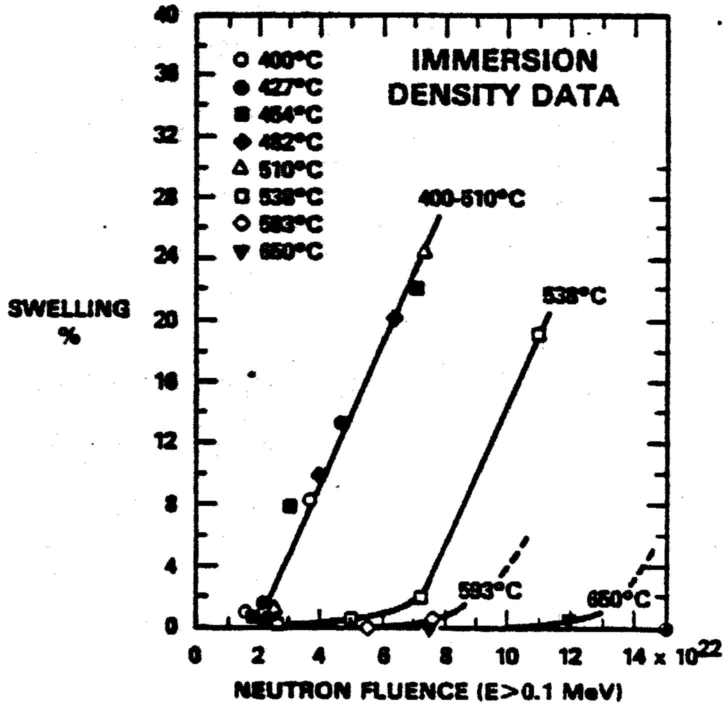

Fig. 6.10. Swelling of the ADIP alloy (Fe-15 Cr-25 Ni) in EBR-II in the range 400-650°C as measured by immersion density.(36)

temperatures near 650°C using data extracted from the damage peak in TEM specimens.

Ion irradiation studies of commercial purity 316 SS have shown swelling rates from 0.1-0.3%/dpa,(44,45,50-52) slightly lower, but similar to those of the P7 alloy. It can be seen from Fig. 6.9, however, that a long transient period of low swelling exists in nominal purity 316 SS.

These swelling rates, however, are a factor of 2 to 3 lower than the fast neutron swelling rates (see Section C.2). Garner has stated(36) that the discrepancy of the ion-induced swelling rates with the intrinsic 1%/dpa neutron-induced rate is due to the suppression effects on void swelling exerted by the injected ions used in the bombardment studies (see Section B). Garner(36) reassessed the findings of the Alloy Development Intercorrelation Program (ADIP) experiment, in which a well-characterized alloy (Fe-15 Cr-25 Ni) was pre-implanted with 6 appm helium at room temperature and subsequently irradiated with nickel ions at temperatures from 600-750°C. In that study, a rate of 0.2%/dpa was independently determined from damage-peak data after irradiation with 5 MeV (General Electric), 2.8 MeV (Naval Research Laboratories) and 3.5 MeV (Westinghouse-Advanced Reactor Division) nickel ions.(53) Garner cites later work by Johnston,(54,55) where anomalous "subsurface" swelling is detected at the near-surface depths (100-300 nm) in 4 MeV nickel-ion-irradiated 304 SS and 316 SS sectioned by ion-milling to various depths. It is important to note that these samples were pre-implanted to 15 appm helium and electropolished at room temperature prior to irradiation. Whitley(39) noted the strong effect of a pre-irradiation electropolish on void formation during heavy-ion irradiation. Thus, the results of Johnston could be influenced by this experimental step.(56) Johnston irradiated an additional 304 SS specimen which had 500 nm of the surface sputtered away after the electropolish. The post-irradiation specimen still exhibited the anomalous "subsurface" swelling. Garner(36) also cites heavy-ion irradiations of nickel at 525°C by Whitley(39) in which swelling rates approach 0.8%/dpa when determined from near-surface data, which are free from the injected interstitial effects.

The results of the present P7 irradiations at 650°C (see Fig. 6.6) do not exhibit any anomalous subsurface swelling behavior and the previous discussion in Section B shows that the influence of the injected ion species is not observed in P7 at temperatures $>$ 550°C. In addition, a recent study by Bullen(43) has shown swelling rates of 0.2%/dpa in 14 MeV nickel-ion-irradiated nickel at 1 μm.

C.2 Fast Neutron and Electron Swelling Rates of Austenitic Stainless Steels

For the past several years it has been reported(36,57) that austenitic stainless steel alloys eventually swell at a rate of 1%/dpa under fast neutron irradiation. This rate is reached after a transient regime, an initial dose period of relatively low swelling. Various factors effect only the duration of the transient regime, not the post-transient rate. These include the irradiation temperature,(58-60) major and minor solute levels,(61,5) degree of cold work(62) and helium content.(63) Figure 6.10 displays typical fast neutron swelling results of an austenitic steel ternary alloy and 316 SS.

Data from HVEM studies of 316 SS show an approach to the 1%/dpa rate.(64) Surface effects act to reduce the swelling, however, and data must be extracted from the foil interior.(65) Garner and Thomas(66) approximate the void-free zone of a surface to be $L_{vf} \sim (D_v/P)^{1/2}$ where L_{vf} is the width of the void-free zone, D_v is the diffusivity of vacancies and P is the point defect production rate.

C.3 Factors Which Determine the Swelling Rate of Austenitic Stainless Steel

A model to explain the temperature and solute level insensitivity of the swelling rate in austenitic stainless steels have been developed by Wolfer and Garner.(34,35,67) For bias driven(67) swelling Wolfer and Garner have shown(35) that the steady state swelling rate can be expressed by

$$\frac{d}{dt}\frac{\Delta V}{V} = \frac{S_o S_d}{(S_o + S_d)^2} \cdot B \cdot F(P,T) \qquad (6.7)$$

where S_o and S_d are the sink strength of voids and dislocations, respectively, B is the net bias, and F is a weakly dependent function of temperature and total sink strength, but strongly dependent on the rate of point defect production, P, written as

$$P = \beta \dot{D} \tag{6.8}$$

where $\dot{D}$ is the displacement rate and β (≈ 0.1) is the fraction of defects which survive in-cascade recombination and clustering. The swelling rate in units of (%/dpa) can now be written

$$\frac{d(\Delta V/V\ \%)}{d(\text{dpa})} = \frac{S_o S_d}{(S_o + S_d)^2} 100\ \beta B(F/P)\ . \tag{6.9}$$

The first term, containing void and dislocation sink strengths, is relatively insensitive to temperature since both S_o and S_d possess similar temperature dependencies. Also, for a microstructure of balanced sink strengths, $S_o \approx S_d$, the first term equals 0.25, independent of temperature. Figure 6.11 shows that the term (F/P) is temperature insensitive and equal to 0.5 when the sink strength of the microstructure exceeds 2×10^{10} cm^{-2} and the vacancy migration energy is 1.1 eV.(34,35) Recent measurements by Khanna and Sonnenberg(68) and Smedskjaer et al.(69) show that the vacancy formation energy in nickel is 1.7 eV. The activation energy for self-diffusion in nickel $(E_v^f + E_v^m)$ is a well-established value of 2.8 eV.(70) Thus, Wolfer and Garner have chosen the migration energy of 1.1 eV in their swelling rate model. Using the above values in Eq. (6.9), the swelling rate becomes

$$\frac{d(\Delta V/V\ \%)}{d(\text{dpa})} \leq 1.25\ B\ (\%/\text{dpa})\ . \tag{6.10}$$

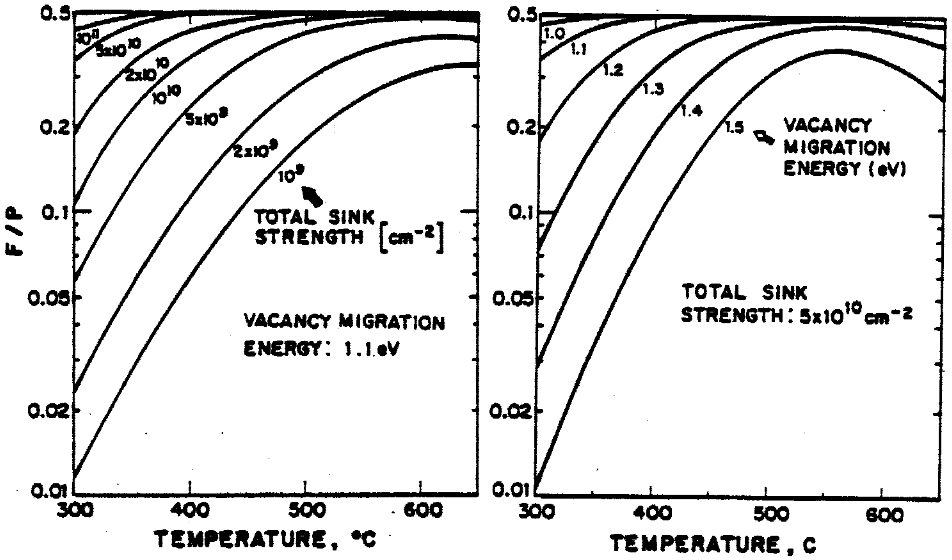

Fig. 6.11. The function F/P, which determines the temperature dependence of the steady state swelling rate, depends on total sink strength, temperature, and vacancy migration energy.(35)

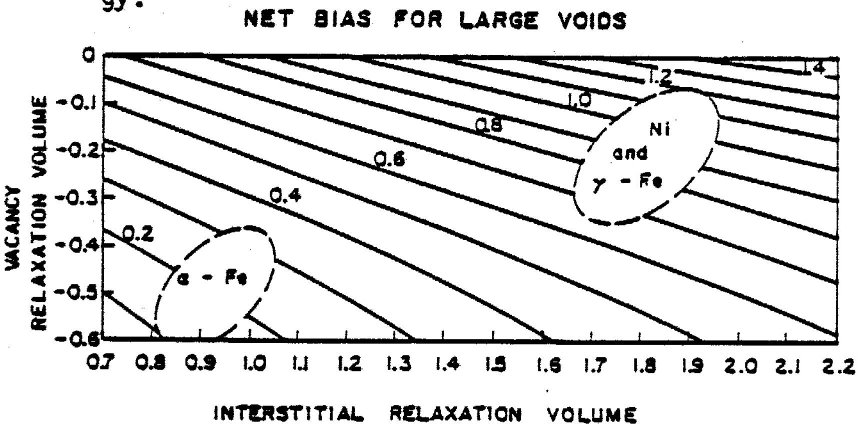

Fig. 6.12. Net bias as a function of the relaxation volume.(34)

Sniegowski and Wolfer(34) have shown that the large interstitial relaxation volume in fcc metals along with the small vacancy relaxation volume leads to a net bias, B, of ~ 0.8 (Fig. 6.12). Thus, the swelling rate in austenitic alloys is predicted to swell at a rate of ≈ 1%/dpa, in close agreement to the empirical value derived from fast neutron data.

The above model of the post-transient swelling rate, which is independent of temperature and dose rate, is applicable to heavy ion irradiation data. Several possible mechanisms may account for the swelling-rate discrepancy of heavy-ion data with fast neutron data. These mechanisms include:

1. foil surface effects acting to decrease swelling at near-surface depths;
2. injected interstitial effects acting to suppress void nucleation and growth at depths which correspond to the range of the bombarding species;
3. damage efficiency differences between ion-induced and fast-neutron-induced defect production that result in unequivalent microstructures for similar damage levels;
4. void-straggling effects acting to spread out the damage energy and thus cause a finite decrease in the dpa profile created during ion irradiation;
5. diffusional spreading of point defects away from the damage peak caused by spatial variations in the production of point defects causing a decrease in the void growth rate at the damage peak;

6. anisotropic stresses along the damage range effecting the void growth rate;
7. a temperature-dependent bias accounting for a reduced swelling rate at high temperatures, characteristic of ion data.

As previously mentioned, foil surface effects and injected interstitial effects alone do not account for the lower swelling rate at 650°C observed in this study. Diffusional spreading of the point defects down the gradients caused by the spatial peak in point defect generation can also lead to a decrease in the swelling rate.(33) However, the absorption mean free path, L, is $1/\sqrt{S}$ where S is the total sink strength. For our sink strength of 4×10^{10} cm^{-2}, it is estimated that the escape of point defects from the peak damage region is negligible.

C.4 Effects of Cavitation on Damage Calculations in Ion-Irradiated P7

A possible explanation for the swelling rate discrepancy lies within the dose values ascribed to the swelling profile in ion-irradiated targets. The depth-dependent voidage in ion-irradiated targets alters the damage profile (Fig. 6.7) of a void-free material.

Using transport theory for the distribution of deposited (damage) energy, Wolfer and Benchikh-Lehocine(71) have considered the effect of density changes on the damage energy profile. They did not model the discrete nature of void formation; rather, they homogenized the swelling at a particular depth into a uniform density decrease at that depth. Wolfer found that the effect of a uniform density decrease is to cause the energy deposition profile to shift to greater depths with increasing swelling. This shift of the energy deposition profile is defined as a first-order effect of cavitation. This shift is observed in the experimentally determined swelling profile data in Fig. 6.13. Note that swelling peak, which presumably coincides with the damage peak, "shifts" to greater depths as the swelling level increases with ion fluence. This model shows that there is no reduction in the accumulated displacement dose at the damage peak compared to the dose in void-free material.

Consideration of the discrete nature of voids, absent in the aforementioned approach, yields a different conclusion. Effects of a discrete distribution of voidage on the deposited energy (damage) has been addressed by Odette et al.(72) This study applies the model of Odette in order to estimate the accumulated dose at a particular mass depth (e.g., the peak swelling depth) during the 14 MeV nickel ion irradiation of the P7 alloy.

Following the notation and approach of Odette et al.(72) we let $\lambda(y)$ be the distance within voids through which the bombarding particle has passed upon reaching depth y. That is, a charged particle that penetrates a depth x in a solid target would penetrate a distance y in void-containing material where

$$y = x + \lambda(y) \qquad (6.11)$$

The average value of $\lambda(y)$, $\langle\lambda(y)\rangle$, can be calculated from the volume

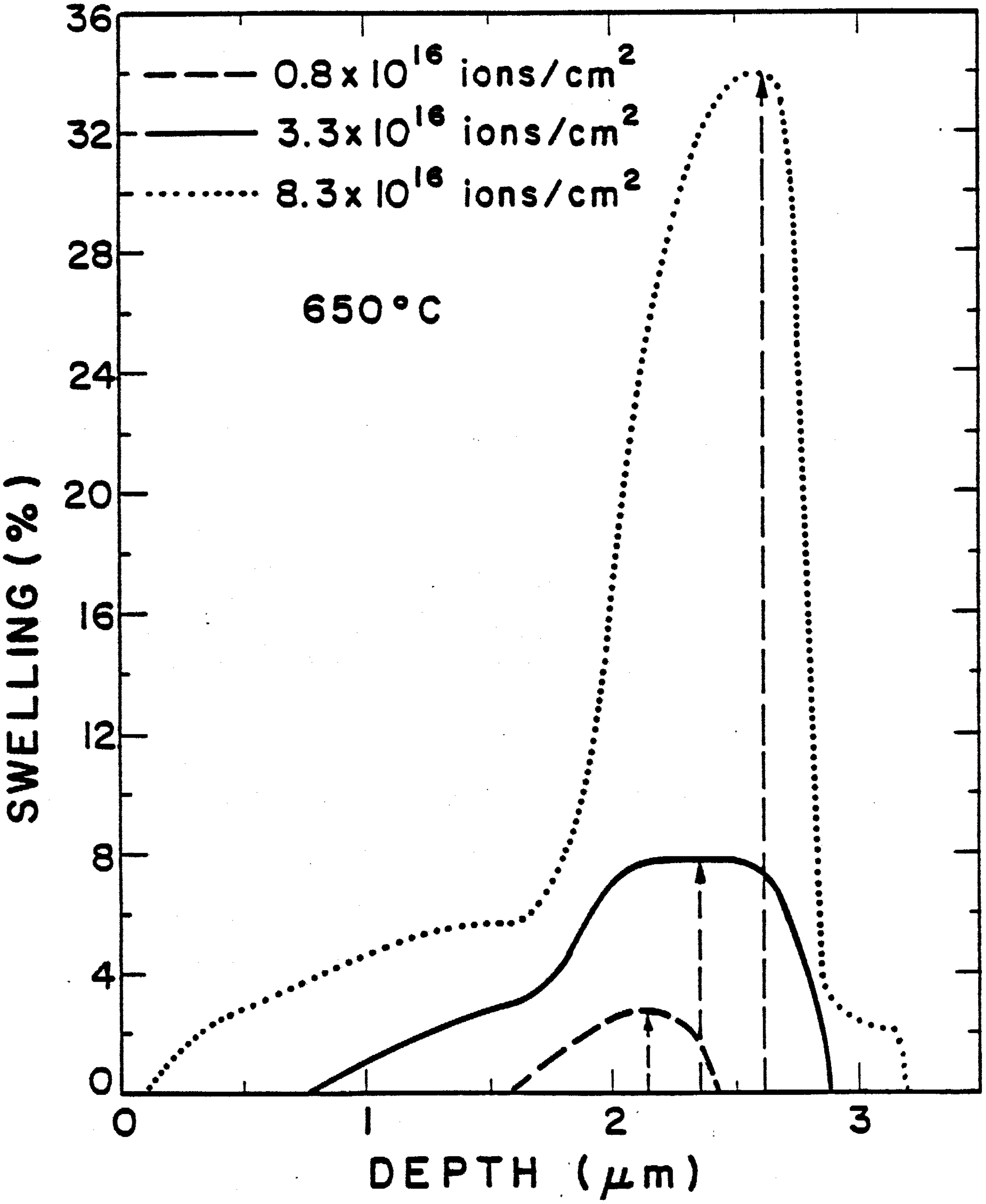

Fig. 6.13. Depth-dependent swelling in the P7 alloy as a function of ion fluence. Note the shift of the swelling peak to greater depths with fluence.

fraction of voids, $\Phi(y)$, by

$$\langle\lambda(y)\rangle = \int_0^y \Phi(y')dy' = \int_0^y \frac{S}{1+S}\, dy' \qquad (6.12)$$

where y' is the integration variable and S is the local swelling, defined by the ratio of void volume to original volume.

Heavy ion irradiation damage is created by a unidirectional beam of projectiles and thus is subject to statistical fluctuations in the energy of the particles at a certain depth based on the number of atomic collisions (prior history) the particles have undergone. This effect is well-known as Bragg straggling(73) and is the intrinsic straggling associated with energy deposited in a solid target. In a void-containing target, the distance traveled through voids by particles reaching depth y will vary as a result of the statistical fluctuations in the number and sizes of voids a particle encounters. This effect is termed(72) "void-straggling" and creates an additional spread in the energy distribution of the particles at depth y which is superimposed on the spread due to intrinsic straggling. The average number of interactions, $\langle n_v\rangle$, between the bombarding ions and voids can be given by

$$\langle n_v\rangle = \langle\lambda(y)\rangle / D \qquad (6.13)$$

where D is a characteristic void length, equivalent to length of the average track of the void. Noting that the average chord length of a sphere of radius R is given by 4/3 R, we will use

$$D = 2/3\ D_{ave} \qquad (6.14)$$

where D_{ave} is the average void diameter.

Next we will approximate the distribution of the number of voids that the particle hits as a Poisson distribution.(74) Thus $\langle n_v \rangle$ is equal to $\sigma_n{}^2$, the variance of the number of voids encountered. Now the standard deviation in the total length through voids traversed upon reaching depth y can be given by σ_λ,

$$D\sqrt{\langle n_v \rangle} = \sqrt{D\langle \lambda(y) \rangle}\ . \qquad (6.15)$$

During the irradiation of a high-swelling material, both $\langle \lambda(y) \rangle$ and D will increase with depth. Thus the void-straggling phenomenon will create an increasing energy spread at a given mass depth as the irradiation proceeds.

The energy deposition at y is now written as:(72)

$$S_D(y) = [1-\Phi(y)] \int_0^\infty f(R) \int_{\lambda_{min}}^{y} P(\lambda)\ S_A(R-y+\lambda)d\lambda dR \qquad (6.16)$$

where f(R) is the probability distribution function which describes intrinsic straggling(75,76) and $S_A(R-y+\lambda)$ is the deposited (damage) energy for a particle with energy $E(R-y+\lambda)$ where $R-y+\lambda$ is the residual solid range of the particle. The probability distribution function, $P(\lambda)$, which describes the void-induced straggling, and λ_{min} is given by

$$\lambda_{min} = \begin{cases} 0, & y<R \\ y-R, & y>R \end{cases} .$$

Equation (6.16) neglects the influence of secondary atom energy transport and does not correct for secondary energy partition. We have used a first-order estimate for $P(\lambda)$ as a normalized Gaussian distribution with parameters $\langle\lambda\rangle$ given by Eq. (6.12) and σ_λ given by Eq. (6.15).

The factor $1-\Phi(y)$ in Eq. (6.16) does not change the dpa value at depth y since the dpa unit is defined for solid material. Also, using the Brice code (see Fig. 6.7) to calculate the dpa profile with intrinsic straggling for void-free material, we can reduce Eq. (6.16) to simply

$$\mathrm{dpa}(y) = \int_{\lambda_{min}}^{y} P(\lambda)\ \mathrm{dpa}(\lambda-y)\,d\lambda \qquad (6.17)$$

to calculate the instantaneous dpa rate at y in the P7 target with voids.

We have applied a simple first-order estimate to the void-straggling phenomenon by using a single set of parameters, $\langle\lambda\rangle$ and σ_λ for $P(\lambda)$. Figure 6.14 displays the depth-dependent instantaneous dpa rate in the P7 target for cases:

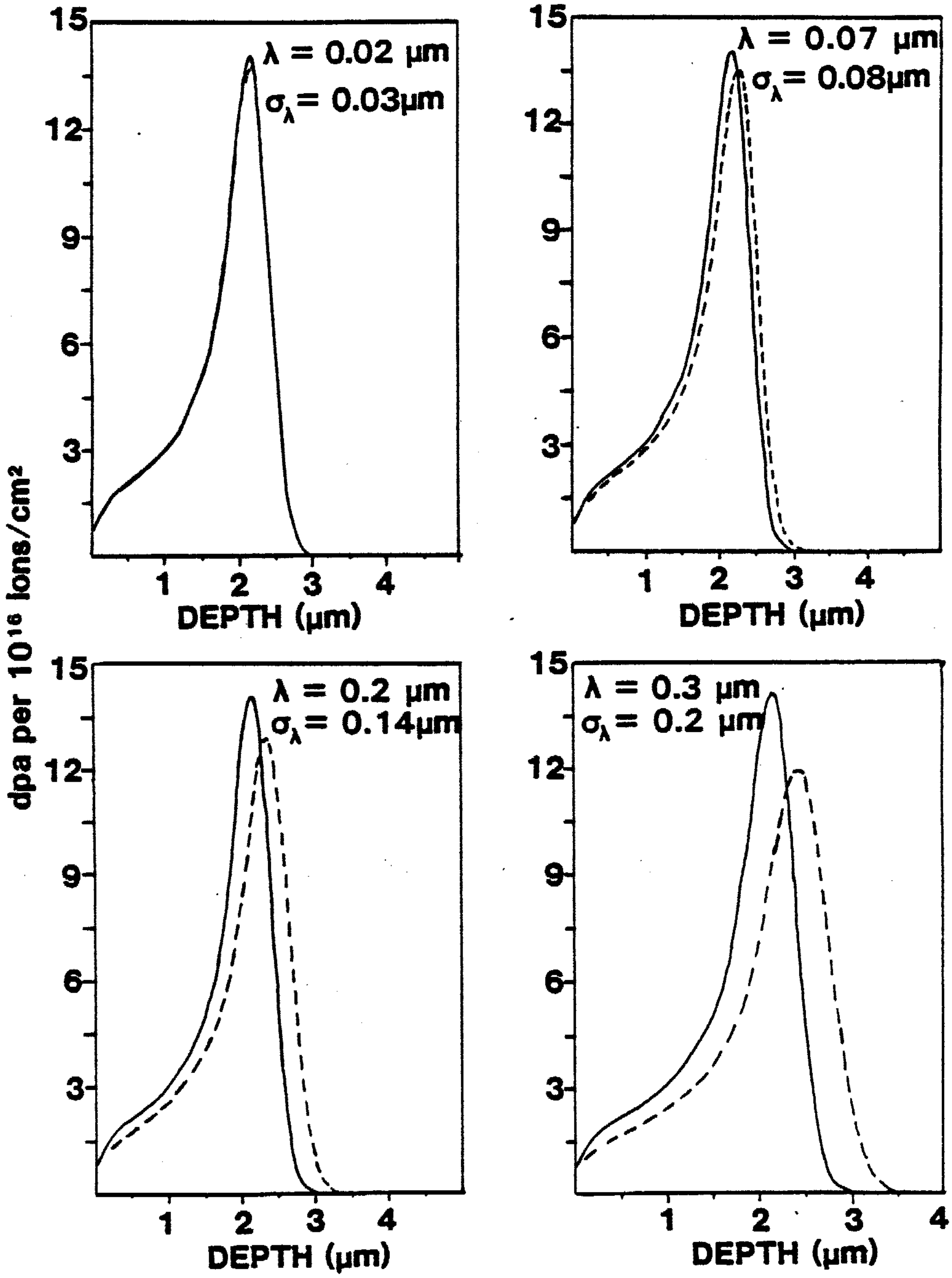

Fig. 6.14. Dpa rate in P7 with voids. Damage profile calculated from Eq. (6.17) with a constant P(λ). An increase in the straggling parameters λ and σ_λ illustrate that (with increased voidage), the peak dpa rate will decrease as the material swells during irradiation (calculations courtesy of S.N. Farrens).

1. $\langle\lambda\rangle = 0.3$ µm, $\sigma_\lambda = 0.2$ µm
2. $\langle\lambda\rangle = 0.2$ µm, $\sigma_\lambda = 0.14$ µm
3. $\langle\lambda\rangle = 0.07$ µm, $\sigma_\lambda = 0.08$ µm
4. $\langle\lambda\rangle = 0.02$ µm, $\sigma_\lambda = 0.03$ µm.

These parameters are consistent with the void parameters of the irradiated P7 samples given in Table 6.3. Note the finite decrease in dpa rate with increasing $\langle\lambda\rangle$ and σ_λ. This decrease, termed second-order void straggling effects, will cause a decrease in the dpa rate to occur with time (dose) at a given mass depth for the high-swelling P7 alloy.

Consideration of these effects of cavitation on the dpa rate of the P7 samples irradiated at 650°C has led to the correction of the swelling versus dpa curve shown in Fig. 6.8. Figure 6.15 displays the curve which is modified to account for the real decrease in dpa at a given mass depth (e.g., swelling peak). The accumulated dose levels are determined by a linear interpolation of the damage rate curves given in Fig. 6.14. It is seen from Fig. 6.15 that the second-order effects become important at swelling levels of 20%. The large ~ 200 nm voids are responsible for the large value of the void-straggling parameter at these swelling levels. The corrected swelling rate of the P7 alloy approaches 0.7%/dpa after a transient dose of 50 dpa and swelling levels ≈ 10%.

Although several possible mechanisms may account for the swelling rate discrepancy between heavy ion and neutron data, the void size and density distribution 14 MeV Ni ion-irradiated P7 necessitate

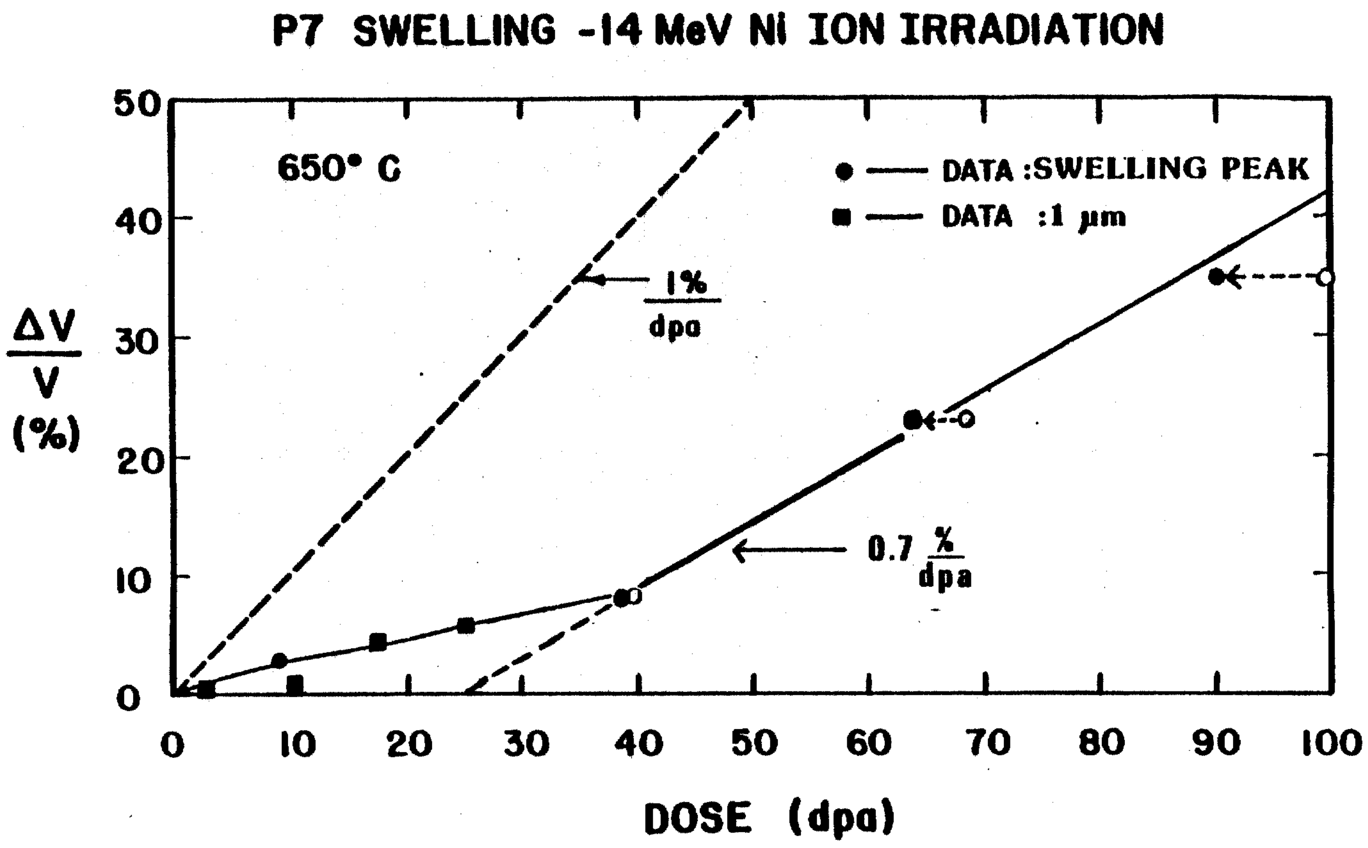

Fig. 6.15. The swelling as a function of dose in P7. Note that the dpa values at the peak swelling depths have been corrected to account for second-order void straggling effects.

the correction of the accumulated dose at the peak swelling depth. Simple first-order corrections applied to the accumulated dose have shown that the void-struggling phenomenon acts to reduce the dpa value at a given mass depth. More accurate calculations are needed however to give a better estimate of the accumulated dose at a given mass depth.

References for Chapter 6

1. G.R. Gessel and A.F. Rowcliffe, in Radiation Effects in Breeder Reactor Structural Materials, M.L. Bleiberg and J.W. Bennett (Eds.), TMS-AIME, 1977, 431-442.
2. M.J. Makin et al., ibid., 645-665.
3. T.M. Williams, J. Nucl. Mater. 88 (1980) 217-225.
4. H. Kawanshi et al., J. Nucl. Mater. 122 & 123 (1984) 284-288.
5. J.F. Bates and W.G. Johnston, in Ref. 1, 625-644.
6. H.R. Brager and F.A. Garner, in Phase Stability During Irradiation, L.K. Mansur and D.I. Potter (Eds.), TMS-AIME, 1980, 219.
7. F.A. Garner and W.G. Wolfer, J. Nucl. Mater. 102 (1981) 143.
8. S.J. Rothman, L.J. Nowicki and G.E. Murch, J. Phys. F 10 (1980) 383.
9. W. Assassa and P. Guiraldeng, Metal Science (1978) 123.
10. G.B. Fedorov and A.N. Seminikhim, Metallurgy and Metallography of Pure Metals Moscow, (1960) Vol. II, 252.
11. H. Oikawa, Tech. Reports, Tohoku Univ. 47, No. 2, (1982) 215.
12. C. Narayan and J.I. Goldstein, Met. Trans. 14A (1983) 2437-2439.
13. G.R. Kegg, J.M. Silcock and D.R.F. West, Met. Sci. 8 (1974) 337-343.
14. A. Azarian and K. Kheloufi, J. Nucl. Mater. 97 (1981) 25-26.

15. F.A. Garner and H.R. Brager, "A Model Describing the Role of Phosphorous on the Swelling and Creep of Austenitic Alloys," presented at First International Conference on Fusion Reactor Materials, Tokyo, 6-8 December 1984.

16. L.D. Glowinski et al., J. Nucl. Mater. 61 (1976) 29.

17. S.C. Agarwal, D.I. Potter and A. Taylor, Met. Trans. A 9A (1978) 569.

18. B.A. Loomis and S.B. Gerber, J. Nucl. Mater. 97 (1981) 113-125.

19. E. Fromm and E. Gebhardt, "Gase and Kohlenstoff in Metallen," Reine und Angewandt Metallkunde in Einseldarstellungen, Band 26, Springer-Verlag, 1976.

20. K. Tanaka and K. Tamaru, J. of Catalysis 2 (1963) 366.

21. R.A. Robie et al., "Thermodynamic Properties of Minerals and Related Substances at 298.15 K and 1 Bar (10^5 Pa) Pressure and at Higher Temperatures," U.S. Government Printing Office, Washington, 1978.

22. G. Bernard and C.M.P. Lupis, Surface Science 42 (1974) 61-85.

23. S.J. Zinkle, L.E. Seitzman and G.L. Kulcinski, "Stability of Vacancy Clusters in Copper and Other Metals," DAFS Quarterly Progress Report DOE/ER-0046/21, April 1985.

24. J.H. Swisher and E.T. Turkdogan, Trans. Met. Soc. AIME 239 (1967) 426-431.

25. E.H. Lee, A.F. Rowcliffe and E.A. Kenik, J. Nucl. Mater. 83 (1979) 79-89.

26. R.L. Sindelar, R.A. Dodd and G.L. Kulcinski, "A Note on Reactive Gas Charging During Pre-Irradiation Specimen Preparation," DAFS Quarterly Progress Report DOE/ER-0046/21, April 1985.

27. J.F. Bates, Scripta Met. 11 (1977) 265-269.

28. K.C. Russell, Acta Met. 19 (1971).

29. J.S. Hudson, J. Nucl. Mater. 60 (1976) 89.

30. K. Farrell, Rad. Effects 53 (1980) 175-194.

31. K. Farrell and N.H. Packan, J. Nucl. Mater. 85 & 86 (1979) 683-687.

32. A.D. Brailsford and L.K. Mansur, J. Nucl. Mater. 71 (1977) 110-116.

33. L.K. Mansur and M.H. Yoo, J. Nucl. Mater. 85 & 86 (1979) 523-532.

34. J.J. Sniegowski and W.G. Wolfer, "On the Physical Basis for the Swelling Resistance of Ferritic Steels," in Proceeding of the Topical Conference on Ferritic Alloys for Use in Nuclear Energy Technologies, Snowbird, UT, 19-23 June 1983.

35. F.A. Garner and W.G. Wolfer, J. Nucl. Mater. 122 & 123 (1984) 201-206.

36. F.A. Garner, J. Nucl. Mater. 117 (1983) 177.

37. B. Badger, Jr., et al., Effects of Radiation on Materials: Twelfth Conference, ASTM STP 870.

38. J.A. Hudson and S.J. Ashby, The Physics of Irradiation-Produced Voids, R.S. Nelson (Ed.), (1974) p. 140.

39. J.B. Whitley, Ph.D. Thesis, University of Wisconsin-Madison, 1978.

40. G.L. Kulcinski, J.L. Brimhall and H. Kissinger, Int. Conf. on Radiation Voids in Metals, Corbett and Ianniello (Eds.), (1972), CONF-710601, p. 449.

41. D.L. Plumton and W.G. Wolfer, J. Nucl. Mater. 120 (1984).

42. A. Si-Ahmed and W.G. Wolfer, ASTM STP 782 (1982) 1008.

43. D.B. Bullen, Ph.D. Thesis, University of Wisconsin-Madison, 1984.

44. W.G. Johnston et al., "The Effect of Metallurgical Variables on Void Swelling," in Radiation Damage in Metals, ASM (1976) 177.

45. E.E. Bloom, J.O. Steigler, A.F. Rowcliffe and J.M Leitnaker, Scripta Met. 10 (1976) 303.

46. W.G. Johnson et al., J. Nucl. Mater. 46 (1973) 273-280.

47. K. Farrell and N.H. Packan, J. Nucl. Mater. 85 & 86 (1979) 683-687.

48. K. Miyahara, N.H. Packan and N. Igata, ASTM STP 782, H.R. Brager and J.S. Perrin (Eds.), (1982) 941-952.

49. N.H. Packan and K. Farrell, Nucl. Tech./Fusion 3 (May 1983) 3.

50. J.S. Hudson, J. Nucl. Mater. 60 (1976) 89.

51. S. Wood et al., ASTM STP 725 (1981) 455-469.

52. N.H. Packan and K. Farrell, ASTM STP 782 (1982) 885-894.

53. F.A. Garner et al., "Summary Report on the Alloy Development Intercorrelation Program Experiment," in Proceedings of the Workshop of Neutron and Charged Particle Damage, CONF-760673, p. 177 (1976).

54. W.G. Johnston, J.H. Rosolowski and A.M. Turkalo, J. Nucl. Mater. 62 (1976) 167-180.

55. W.G. Johnston, W.G. Morris and A.M. Turkalo, in Ref. 1, p. 421.

56. R.L. Sindelar, R.A. Dodd and G.L. Kulcinski, in DAFS Quarterly Progress Report DOE/ER-0046/21, April 1985.

57. F.A. Garner, J. Nucl. Mater. 122 & 123 (1984) 459.

58. J.L. Seran and J.M. Dupouy, ASTM STP 782 (1982) p. 5.

59. J.L. Seran and J.M. Dupouy, in Ref. 1, p. 25.

60. F.A. Garner, in Ref. 6, p. 165.

61. W.J.S. Yang and F.A. Garner, ASTM STP 782 (1982), p. 186.

62. F.A. Garner, DAFS Quarterly Progress Report DOE/ER-0046/12 (Feb. 1983) p. 178.

63. H.R. Brager and F.A. Garner, J. Nucl. Mater. 117 (1983) 159.

64. M.J. Makin et al., J. Nucl. Mater. 95 (1980) 155-170.

65. A. Hishinuma, Y. Kafano and K. Shiraishi, J. Nucl. Sci. and Tech. 14 (1977) 644-672.

66. F.A. Garner and L.E. Thomas, in Effects of Radiation on Substructure and Mechanical Properties of Metals and Alloys, ASTM STP 529 (1973) 303-325.

67. W.G. Wolfer, J. Nucl. Mater. 122 & 123 (1984) 367-378.

68. S.K. Khanna and K. Sonnenberg, Rad. Effects 59 (1981) 91.

69. L.C. Smedskjaer et al., J. Phys. F 11 (1981) 2221.

70. J. Askill, Tracer Diffusion Data for Metals, Alloys, and Simple Oxides, Plenum Press, New York, 1970.

71. W.G. Wolfer and M.E. Benchikh-Lehocine, DAFS Quarterly Progress Report DOE/ER-0046/20 (Feb. 1985).

72. G.R. Odette, D.M. Schwartz and A.J. Ardell, Rad. Effects 22 (1974) 217-223.

73. R. Evans, The Atomic Nucleus, McGraw-Hill, New York, 1955, p. 666.

74. Ibid, p. 660.

75. G.L. Kulcinski, J.J. Laidler and D.C. Doran, Rad. Effects 7 (1971) 195.

76. I. Manning and G.P. Mueller, Computer Physics Comm. 7 (1974) 85-94.

CHAPTER 7. CONCLUSIONS

The cross section method of post-irradiation sample preparation was extended and applied to the study of nickel-ion irradiation effects in two types of austenitic stainless steels. This is the first report of heavy-ion irradiation effects in P7 and 316 SS viewed in cross section. The Magnetic Fusion Engineering reference heat #X-15893 of 316 stainless steel and the P7 alloy, a high purity, austenitic stainless steel alloy were irradiated at temperatures from 400-650°C (0.4-0.55 T_m) up to damage levels of 120 dpa. A swelling rate study was conducted on the P7 alloy at 650°C. The post-transient swelling rate (%/dpa) determined in this study was compared to the intrinsic swelling rate observed for neutron-irradiated 316 SS and to past ion-irradiation investigations of austenitic steel alloys. Specific observations in this present study were:

1. Voids were formed in the P7 alloy at damage levels of 2 to 100 dpa over the entire 400-650°C temperature range of investigation. The void number density decreased whereas the average void diameter increased with temperature at a given displacement dose.
2. A suppression in the average void diameter (growth) and number density (nucleation) was noted at depths corresponding to the calculated 14 MeV nickel ion range in the 400 and 500°C P7 samples. These effects are consistent with the current predic-

tions of the effects of the injected interstitials on void nucleation and growth at low temperatures.

3. Oxygen present in the P7 matrix probably promotes void formation at high temperatures by reducing the surface energy of the voids. In thoroughly outgassed P7, voids were not observed after irradiation to 40 dpa at 650°C.
4. No phase decomposition of the austenite matrix was observed in either the ion-damage region or in the thermal control region over the entire 400-650°C temperature range of irradiation of the P7 alloy.
5. The MFE heat of 316 SS irradiated over a temperature range of 450-650°C and at 10 to 120 dpa produced a low density (2-5 x 10^{14} cm^{-3}) of voids at 450-550°C. No voids were detected up to 40 dpa at 600 and 650°C.
6. The void formation in 316 SS was heterogeneous in nature whereby voids were observed only in conjunction with or at precipitate interfaces. These precipitates were highly enriched in nickel compared to the surrounding 316 SS matrix.
7. The precipitation response of 316 SS at 450-550°C was characteristic of the G-phase. Only a small depth dependency of precipitate size and number density was observed for a particular irradiation temperature. The average precipitate size increased and the number density decreased with an increase in temperature for dose levels from 10-40 dpa.

8. The precipitation response of 316 SS at 600-650°C was predominantly the Fe_2P phase. The Fe_2P lathes were larger (95 nm) and less numerous (2×10^{14} cm^{-3}) at 650°C compared to 600°C (55 nm, 1×10^{15} cm^{-3}) for doses from 10 to 40 dpa.
9. A raw swelling rate of 0.4%/dpa was observed in P7 at 650°C. This rate, although consistent with swelling rates noted in other heavy-ion irradiations, is a factor of two lower than the intrinsic rates of fast-neutron irradiated austenitic alloys. Consideration of void-straggling effects yielded a swelling rate of 0.7%/dpa for the P7 alloy.
10. The range of the radiation-induced dislocation structure ended at depths of 2.9-3.2 μm in the P7 samples with low swelling and in 316 SS. This range is in agreement with the predicted range using the Brice code with LSS electronic stopping.

CHAPTER 8. SUGGESTIONS FOR FUTURE WORK

The wide difference in response to ion-irradiation between the P7 alloy and 316 SS shown by this study suggests that further experimental examination is necessary to identify and quantify the impurity components causing the differences. These experiments might include:

1. The manufacture of a high-purity, oxygen-free austenitic stainless steel alloy with major alloying components similar to those of the P7 alloy should be initiated. This alloy should be irradiated over a wider temperature and dose regime used in this study to determine the temperature range of void formation in the absence of a reactive gas species.
2. Implantation of oxygen in varying amounts into the MFE heat of 316 SS or into other austenitic alloys with differing impurity contents. Subsequent ion irradiations would show whether oxygen -- well in excess of that normally present -- could promote void formation.

The results of the swelling rate study on P7 using the cross-section technique, provided valuable information on the ion-irradiation swelling rate. Further swelling rate studies might include:

1. Higher fluence irradiations of P7 should be conducted at 650°C to investigate whether ion-irradiated P7 will show a saturation in swelling.

2. Swelling rate studies of P7 should be conducted at a temperature of 550°C. This temperature was shown to exhibit no depth-dependent suppression effects from the injected interstitial species. Comparison of the 650°C study to 550°C would show any temperature dependence on the linear swelling rate of austenitic steels under ion irradiation.